UNIVERSITY OF CALIFORNIA SAN DIEGO

# Design and Fabrication of Acoustic Metamaterials in Near-megahertz Range

A dissertation submitted in partial satisfaction of the
requirements for the degree
Doctor of Philosophy

in

Nanoengineering

by

Jiaying Wang

Committee in charge:

Professor Oscar Vazquez-Mena, Chair
Professor James Friend, Co-Chair
Professor Nicholas Boechler
Professor Shaochen Chen
Professor Donald Sirbuly

2020

The dissertation of Jiaying Wang is approved, and it is acceptable in quality and form for publication on microfilm and electronically:

_____

_____

_____

_____
Co-Chair

_____
Chair

University of California San Diego

2020

DEDICATION

*To my grandmother, in loving memory.*

# EPIGRAPH

*Knowing yourself is the beginning of all wisdom.*

—Aristotle

TABLE OF CONTENTS

LIST OF FIGURES

LIST OF TABLES

# ACKNOWLEDGEMENTS

First and foremost, I would like to thank my supervisor, Professor Oscar Vazquez-Mena. Without his constant guidance and supporting over the years, this work would not be achieved successfully. I was inspired and enlightened by his profound knowledge, sense of humor and most importantly, passion for science. I also would like to express my utmost gratitude to my co-supervisor, Professor James Friend. He placed me in the care of talented Ph.D. student as his own student and supported me without reservation. I also appreciate Professor Sheng Xu to provide me the opportunity to fulfill my dream of being a student here.

I would like to thank my dissertation committee, Professor Nicholas Boechler for challenging my knowledge and guiding experiments for my dissertation. I also would like to appreciate Professor Sreekanth Chalasani, Professor Shaochen Chen and Professor Donald Sirbuly for their insightful comments and constructive suggestion which significantly gains my research experience and improve this dissertation.

I would like to thank all the postdoc I met and worked with in the past five years, Dr. Lin Zhang, Dr. Morteza Miansari, Dr. Abdoulaye Ndao, Dr. Jeremy Orosco, Dr. Amihai Horesh and Dr. Cécile Floer. Thanks for their guidance in the research path. I also would like to thank Dr. Florian Allein, in a special way, for all of his invaluable supporting and assistance in the past two years. I would like to express my appreciation to my previous and current labmates in 2DLab, Dr. Wenjun Chen, Malcolm Lockett, Seungbae Ahn and Leon Li. I also would like to thank all the PhD students in MADLab, Naiqing Zhang, Gopesh Tivawala, Jiyang Mei, An Huang, Shuai Zhang, Aditya Vasan, and William Connacher. I will miss all the time we worked together in the SME 320 and everyone's birthday we celebrated together.

I would like to appreciate Professor Max C. Lemme and Dr. Stefan Wagner from RWTH Aachen University, Germany for 3D Raman tomography. I also would like to appreciate Professor Luis Guillermo Villanueva from EPFL for the high-stress silicon nitride coated wafer and preliminary resonance frequency characterization.

Finally, I would like to acknowledge with gratitude and support and love of my parents. They all kept me going, and this dissertation can not have been possible without them. I also would like to thank my wife, Mingyang Gao for her encouragement and supporting in the past ten years. As my girlfriend, her name appeared in the last paragraph of my Bachelor and Master degree thesis. I would like to write her name here again as the romantic letter to her.

Chapter 2, in part, have been submitted for publication of the material as it may appear in Physical Review Applied, 2020. Jiaying Wang, Florian Allein, Nicholas Boecholer, James Friend, Oscar Vazquez-Mena. "Design of Negative Refractive Index Metamaterials for Near-Megahertz Enhanced Acoustic Transmission in Future Biomedical Ultrasound Applications", Physical Review Applied. 2020. The dissertation author was the primary investigator and author of this paper.

Chapter 3, in full, is a reprint of the materials as it appears in Journal of Micromechanics and Microengineering 2020. Jiaying Wang, Jiyang Mei, James Friend, Oscar Vazquez-Mena."Frequency and damping effect of suspended silicon nitride membranes in water near the megahertz range", Journal of Micromechanics and Microengineering, 2020. The dissertation author was the primary investigator and author of this paper.

Chapter 4, in full, is a reprint of the materials as it appears in ACS applied materials interfaces 2018. Jiaying Wang, Stefan Wagner, Wenjun Chen, Yuesong Shi, Abdoulaye Ndao, Leon Li, Boubacar Kante, Donald Sirbuly, Max C Lemme, Oscar Vazquez-Mena. "Integration of Nanomaterials into Three-Dimensional Vertical Architectures", ACS applied materials interfaces, 10(34) 28262-28268, 2018. The dissertation author was the primary investigator and author of this paper.

## VITA

| | |
|---|---|
| 2013 | B. S. in Materials Science and Engineering, Harbin Institute of Technology, China |
| 2015 | M. S. in Materials Science, Harbin Institute of Technology, China |
| 2020 | Ph. D. in Nanoengineering, University of California San Diego |

## PUBLICATIONS

**Jiaying Wang**, Florian Allein, Nicholas Boecholer, James Friend, Oscar Vazquez-Mena. "Experimental realization of acoustic metamaterials in mega-hertz range", *Advanced Materials*, in preparation.

**Jiaying Wang**, Jiyang Mei, James Friend, Oscar Vazquez-Mena."Frequency and damping effect of suspended silicon nitride membranes in water near the megahertz range", *Journal of Micromechanics and Microengineering*, Accepted, 2020.

**Jiaying Wang**, Florian Allein, Nicholas Boecholer, James Friend, Oscar Vazquez-Mena. "Design of Negative Refractive Index Metamaterials for Near-Megahertz Enhanced Acoustic Transmission in Future Biomedical Ultrasound Applications", *Physical Review Applied*, Revision and resubmit, 2020.

Shuai Zhang, An Huang, Avinoam Bar-Zion, **Jiaying Wang**, Oscar Vazquez Mena, Mikhail G Shapiro, James Friend. "The Vibration Behavior of Sub-Micrometer Gas Vesicles in Response to Acoustic Excitation Determined via Laser Doppler Vibrometry", *Advanced Functional Materials*, 30(13), 2020.

Wenjun Chen, Seungbae Ahn, Marquez Balingit, Jiaying Wang, Malcolm Lockett, Oscar Vazquez Mena. "Near full light absorption and full charge collection in 1-micron thick quantum dot photodetector using intercalated graphene monolayer electrodes", *Royal Society of Chemistry*, 409-4915, 2020.

Viviana Sarmiento, Mercedes Teresita Oropeza-Guzmán, Malcolm Lockett, Wenjun Chen, Seungbae Ahn, Jiaying Wang, Oscar Vazquez-Mena. "Electrochemical functionalization strategy for chemical vapor deposited graphene on silicon substrates: grafting, electronic properties and biosensing", *Nanotechnology*, 30(47) 475703, 2019.

Jiaying Wang, Stefan Wagner, Wenjun Chen, Yuesong Shi, Abdoulaye Ndao, Leon Li, Boubacar Kante, Donald Sirbuly, Max C Lemme, Oscar Vazquez-Mena. "Integration of Nanomaterials into Three-Dimensional Vertical Architectures", *ACS applied materials & interfaces*, 10(34) 28262-28268, 2018.

**Jiaying Wang**, Yang Li, Zhao-Yao Zhan, Tie Li, Liang Zhen, Cheng-Yan Xu. "Elastic properties of suspended black phosphorus nanosheets", *Applied Physics Letters*, 108(1), 013104, 2015.

Yang Li, Cheng-Yan Xu, Jing-Kai Qin, Wei Feng, **Jiaying Wang**, Siqi Zhang, Lai-Peng Ma, Jian Cao, Ping An Hu, Wencai Ren, Liang Zhen. "Tuning the Excitonic States in MoS2/Graphene van der Waals Heterostructures via Electrochemical Gating", *Advanced Functional Materials*, 26(2), 293-302, 2014.

**Jiaying Wang**, Zhihua Yang, Xiaoming Duan, Dechang Jia, Yu Zhou. "Microstructure and mechanical properties of SiCf/SiBCN ceramic matrix composites", *Journal of Advanced Ceramics*, 4(1), 31-38, 2015.

Yang Li, Cheng-Yan Xu, **Jiaying Wang**, Liang Zhen. "Photodiode-Like Behavior and Excellent Photoresponse of Vertical Si/Monolayer MoS2 Heterostructures", *Scientific reports*, 4, 7186, 2014.

**Jiaying Wang**, Xiaoming Duan, Zhihua Yang, Dechang Jia, Yu Zhou. "Ablation mechanism and properties of $SiC_f$/SiBCN ceramic composites under an oxyacetylene torch environment", *Corrosion Science*, 101-107, 2014.

ABSTRACT OF THE DISSERTATION

**Design and Fabrication of Acoustic Metamaterials in Near-megahertz Range**

by

Jiaying Wang

Doctor of Philosophy in Nanoengineering

University of California San Diego, 2020

Professor Oscar Vazquez-Mena, Chair
Professor James Friend, Co-Chair

Ultrasound is strongly attenuated, reflected and aberrated in the skull and on the interface, due to the complex structure and acoustic impedance mismatch of biological layer. Acoustic metamaterials with effective negative density and modulus have been proved to enhance the ultrasound transmission in theoretical and experimental physics, which also can enable for bidirectional ultrasound delivery for ultrasonic imaging and neurostimulation. However, it is quite challenging to prepare and fabricate the double-negative metamaterials in biomedical application frequency range due to the limitation of fabrication and characterization methods.

Therefore, we present the design of negative refractive index acoustic metamaterials

that operate at near-megahertz frequencies and is intended for the eventual aim of enabling enhanced acoustic transmission through high impedance-contrast biological layers. The negative properties are composed by a linear array of unit cells Helmholtz resonators and membranes. The dispersion relation, the effective modulus and density of the proposed negative metamaterials are calculated by COMSOL Multiphysics. The enhancement of ultrasound transmission through high-impedance-contrast layer is proven by a full three-dimensional model of the metamaterials. The transmission improves from 80% transmission through a high impedance layer alone to near 100% transmission through the metamaterial-plus-high-impedance layer combination. As the preliminary experimental realization, the unit cell structure created using a novel nanofabrication approach, is presented and characterized between 230 kHz and 410 kHz.

We study the vibration behavior of silicon nitride membrane in water to further improve the resonant frequency of silicon nitride membrane above 1 MHz. We demonstrate that the water mass loading effect dominates the reduction of resonant frequency. Meanwhile, the non-dimensionalized added virtual mass incremental (NAVMI) factors are experimentally calculated to estimate the resonance reduction. Based on the scaling law, we developed a new microfabrication method to integrate horizontal suspended thin films with functional nanomaterials into three-dimensional architectures for highly-compact micro/nanoscale devices. This method also reduces the spacing between the horizontal membrane structure from 200 μm to 2 μm, which provides the possibility for high-frequency range metamaterial component.

This work demonstrates the first membrane-Helmholtz resonator based metamaterials component works in near-megahertz range, which provides a new potential method to achieve ultrasonic transmission enhancement for biomedical application. Our approach also paves the way for the development of active acoustic metamaterials, acoustic metasurface and superlensing.

# Chapter 1

# Introduction

## 1.1 Background

### 1.1.1 Acoustic Double Negative Metamaterials

Metamaterials are defined artificial engineering materials exhibiting unusual optical or mechanical properties which have not been observed in the nature[1, 2, 3, 4, 5, 6]. It is composed by subwavelength components to manipulate the acoustic/electromagnetic wave in unusual properties at the beginning. This idea has been approved by Pendry's experimentally by achieving the magnetic negative permeability and negative dielectric constant[7, 8, 9]. These theoretical and experimental results inspire the acoustic metamaterials to manipulate the mechanical wave in the elastic medium[10].

Although the acoustic wave in the fluid, such as air and water is longitude wave and the electromagnetic wave is transverse wave, the negative refractive constant in EM waves can be assumed by negative density behavior because of the similar mathematics equation[11]. Similarly, the negative magnetic dielectric properties can be assumed by negative modulus behavior in the acoustic metamaterials. The unusual excellent parameters values of metamaterials extend the application by manipulating the acoustic wave, which are expected to be utilized in acoustic

cloaking[12, 13, 14], subwavelength imaging[15, 16, 17] and acoustic diode[18, 19, 20].

Generally speaking, the negative density and negative modulus behaviors are illustrated in Fig.1.1(a) and (b). The negative density behavior means when a mass excited under a external force, the acceleration of the mass is in an opposite direction of the force direction[21]. The negative bulk modulus behavior implies the volume of the mass expands under an compression force (Fig.1.1(c) and (d))). The negative behavior of metamaterial can be derived from Newton's 2nd law. Considering a one-dimensional mass-spring-mass oscillator excited by an external harmonic excitation, the effective mass of system can by expressed by following equations[11]:

$$\bar{M}(\omega) \;=\; M_1 + \frac{K}{\omega_0^2 - \omega^2} \tag{1.1}$$

where $M_1$ and $M_2$ are the mass of oscillator, $K$ is the spring constant and $\omega_0$ is the local resonance frequency of mass $M_2$. which shows the dispersive behavior at the resonant frequency of the system. Considering the volume of the system does not change, the dynamic effective density of the system ($\bar{\rho} = \bar{M}(\omega)/V$) shows the same behavior of effective mass of system, which shows the negative density in the frequency region close to the resonant frequency $\omega_0$. This disperive relation can be worked as the basic phenomena to express most of the negative density/modulus behavior of passive acoustic metamaterials. If the acoustic system includes both of negative-density component and negative-modulus component, the system will shows double-negative (negative-density, negative modulus) behavior in the overlap working frequency range. In the following sections, two types of popular double-negative metamaterials will be discussed, namely the localized resonant double-negative metamaterials (Sec.1.1.2) and membrane-based double-negative metamaterials (Sec.1.1.3).

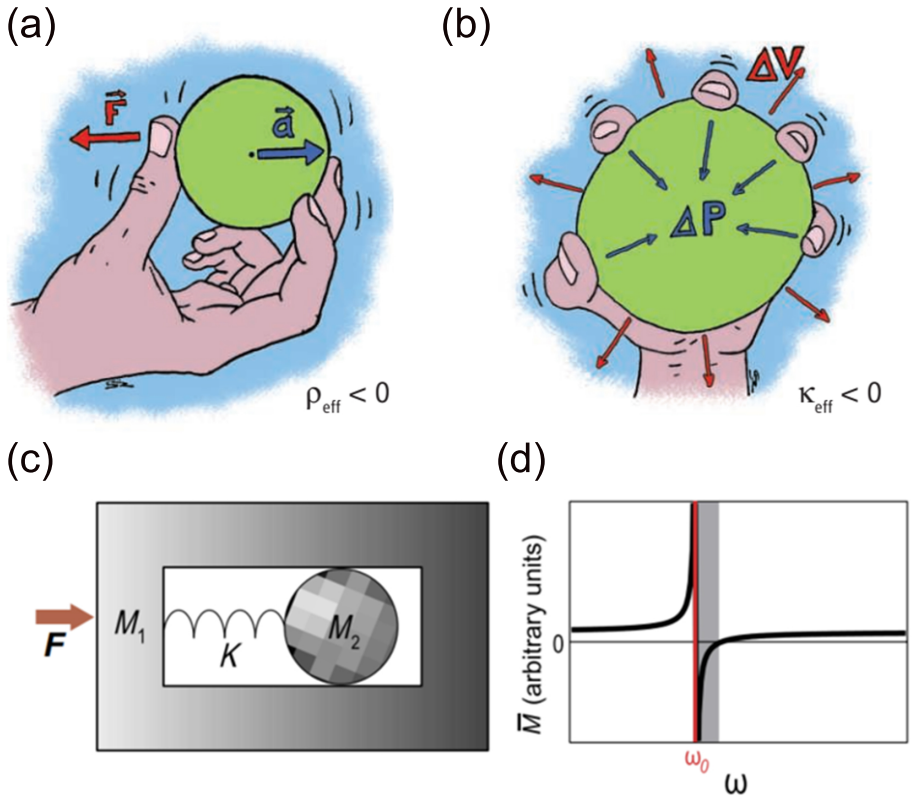


**Figure 1.1**: The origin of negative behavior of metamaterials: (a)The acceleration of negative density metamaterials is in the opposite direction of external harmonic excitation; (b) The volume of negative modulus metamaterial expands under an isotropic compression; (c) The schematic of a spring-coupled oscillator; (d) The average of the total mass is dispersive at the resonance $\omega_0$ and shows the negative value in the gray area[4, 21].

### 1.1.2 Localized resonant double-negative metamaterials

The first experimental realization of double negative acoustic metamaterials is composed by the polymer-coated lead ball and structural matrix, which achieves negative density up to 200 kHz by inducing the local-resonance of this structures[5, 22, 10]. The microstructures of these local-resonance double-negative metmaterials are illuminated in Fig.1.2 (a)[10]. There are three different components, namely the solid particles, soft elastic matrix and structural matrix[10]. 'A' demonstrates the rigid and high-density solid particles, embedding into a structural matrix, named 'C'. These solid 'A' particles are surrounded by the soft elastic matrix 'B'. These

scattering components are coupled strongly at the resonance frequency, which demonstrates a large frequency dispersion of the wave propagation characteristics. This resonance response could be expressed by $1/(\omega_0^2 - \omega^2)$. When the working frequency is smaller than the $\omega_0$, a negative response appears due to the center-of-mass motion between the matrix and B. As shown in Fig.1.2(c), there is two valleys at 400 and 1000 Hz, which is caused by the negative effective parameters. And similar phenomena is observed for hexagonal coated sphere in polymer matrix with similar design, which is proved by theoretical calculations.

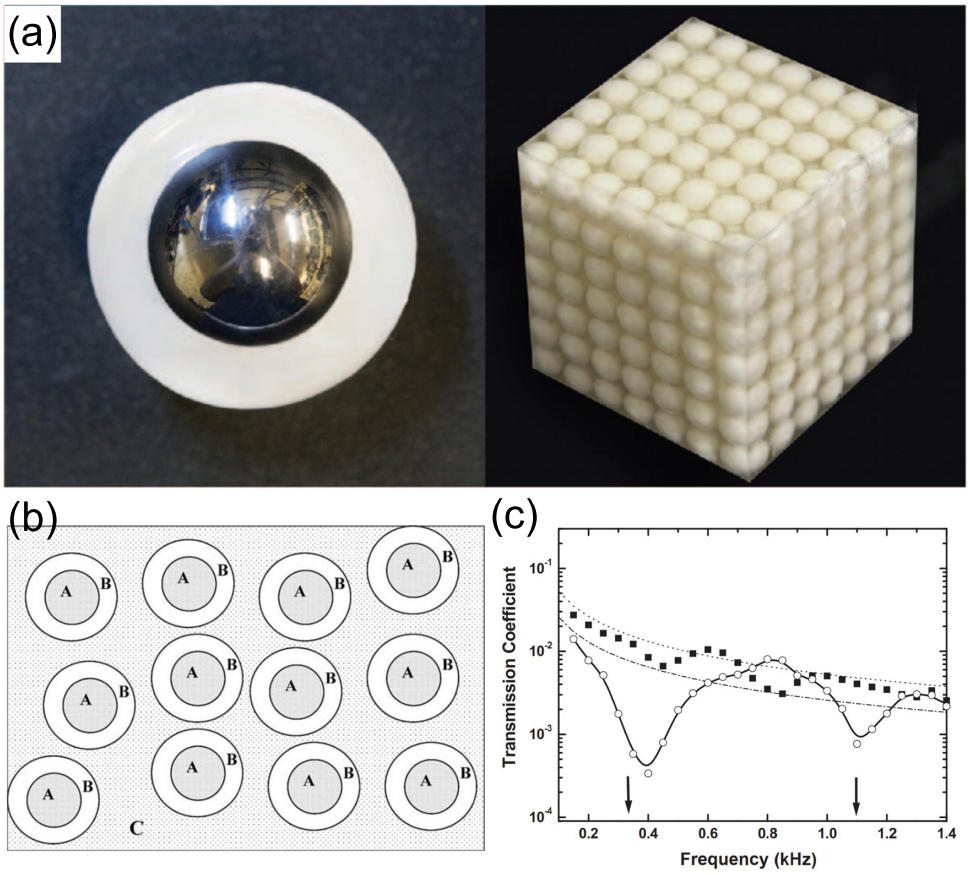


**Figure 1.2**: (a) Left: The cross-section view of unit cell, including a metallic sphere structure coating with silicone polymer; Right: Localized resonance metamaterials (b)Schematic of matrix/polymer/sphere microstructures of localized metamaterials; (c)Transmission coefficient of localized resonance metamterials[5, 10]

To extend the application into the high frequency range, micrometer-scale resonator is

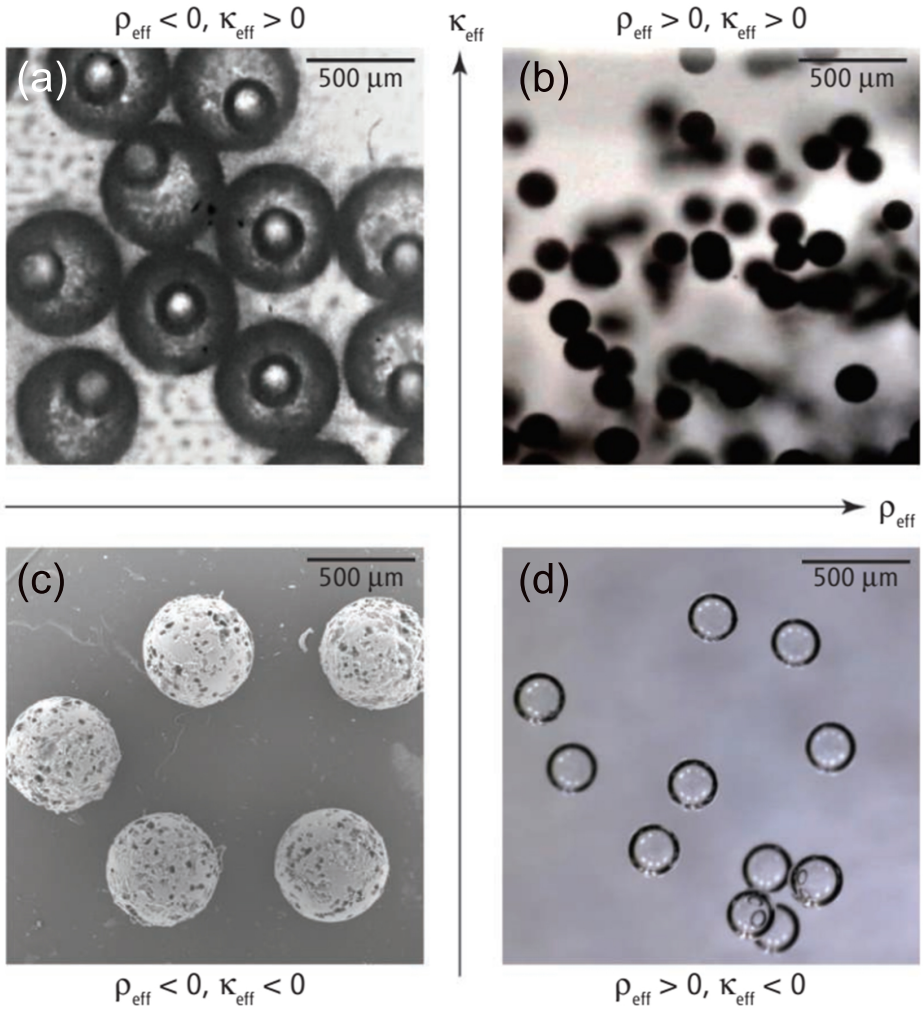


**Figure 1.3**: Microstructure of Mie-resonance metamaterials with different fillers: (a) core-shell filler; ($\rho_{\text{eff}} < 0, \kappa_{\text{eff}} > 0$) (b) Slow oil filler; ($\rho_{\text{eff}} > 0, \kappa_{\text{eff}} > 0$)(c) Polymer porous beads; filler($\rho_{\text{eff}} < 0, \kappa_{\text{eff}} < 0$) (d) Air bubble as fillers. ($\rho_{\text{eff}} > 0, \kappa_{\text{eff}} < 0$).

required to manipulate megahertz range elastic wave. Therefore, similar by introducing the sub-millmeter size micro particle into fluidic gel or soft solids to process negative-density, negative modulus or double negative microfluidic system are discovered, which allows a wide controllable multipolar Mie resonances by producing different types of high-density, high-dispersion particles[21, 23]. Figure 1.3 shows the interior microstructures of these metamaterials. There are four types of microparticles, namely, core-shell particles (negative density and positive modulus); slow-oil particles (positive density and positive modulus); polymer porous beads (negative density

and negative modulus) and air bubbles (positive density and negative modulus). To achieve double-negative behavior, Brunet etal[23] represented a soft three-dimensional acoustic metamaterials, which is composed by macroporous microbeads-filled polymer matrix. The microbeads work as ultra-slow Mie resonator embedding into the polymer matrix, which controls the sign of effective density and modulus. To avoid the possible phase shift by the interface, the soft acoustic metamaterials is excited by Gaussian-moduluated sine wave and the phase shift is calculated by the center of the pulse signal. As shown in Fig.1.4, there is a negative to positive sign change of phase shift from 110 kHz to 170 kHz, which indicates the phase velocity transfers from negative to positive. The phase velocity as the function of filler ratio is experimentally measured and calculated by Waterman-Truell formula. Thanks for this methods, a flat soft gradient-index metasurfaces are engineered to control the three-dimensional wavefront in water[24]. By applying the flat acoustic lens on a plane wave transducer, the ultrasonic wave can steer and focus as designed and vortex beam also can be generated from the transducer. However, this water-based gel matrix dissolves in the water and there is also a strong attenuation effect caused by the porous microbead filler, which needs to be taken into account in the biomedical application.

### 1.1.3 Membrane-based acoustic metamaterials

Compared with the other components to achieve the negative density behavior, the fixed-edge membrane and plates are more light-weight and efficient way to manipulate the elastic wave with a sub-wavelength acoustic components[25, 26, 27, 28, 11, 29, 30]. The resonant frequency of membrane can be easily controlled by the dimensions of membrane including the membrane width, thickness and interior stress, which dominates the working frequency of negative density[31]. Meanwhile, by introducing the other acoustic components into membrane array, namely the side hole[32, 33], Helmholtz resonator[34, 35] and open channel which are placed in parcell with channel, the double-negative behavior is achieved in the overlap between the negative modulus and negative density working frequency range.

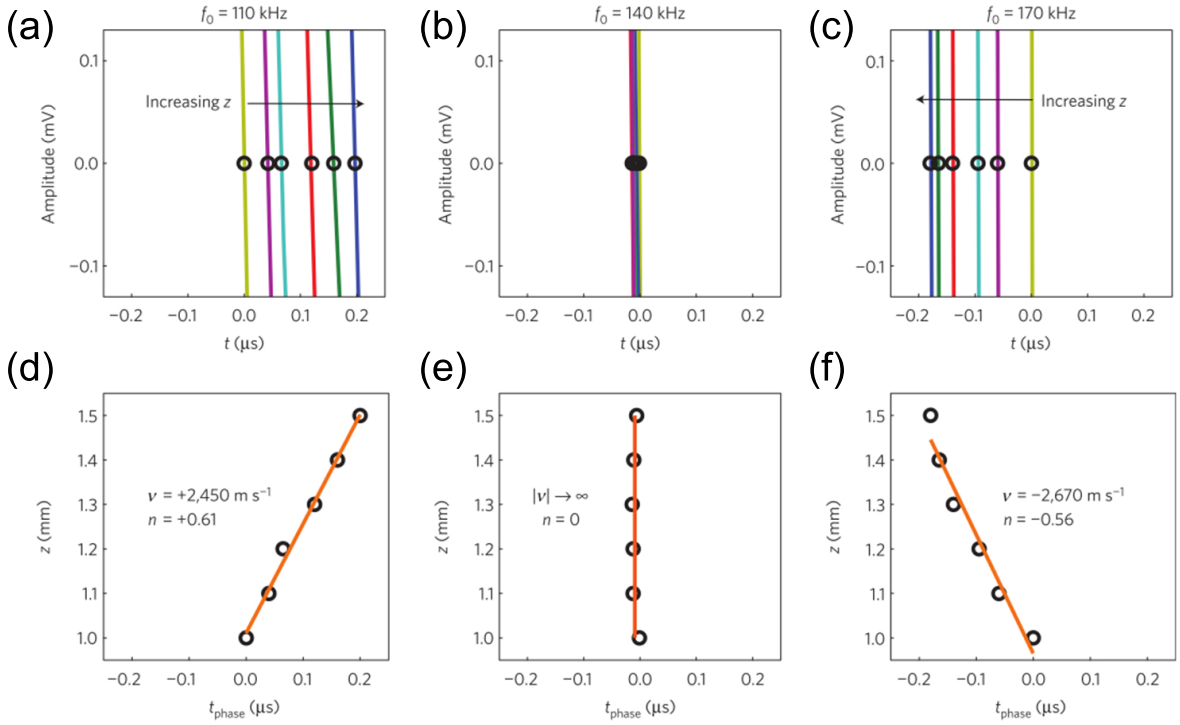


**Figure 1.4**: Phase shift and group velocity of micro-beads-filler-based metamaterials[23]: (a)-(c) Phase shift at 110, 140 and 170 kHz; (d)-(f) Group velocity at 110, 140 and 170 kHz[23].

The first negative-density metamaterials by placing a couple of membrane is proposed by Lee etal[28] with a certain period distance to form the one-dimensional waveguide. Negative density behavior is observed under the (1,1) mode resonant frequency of membrane. At the same time, negative modulus metamaterial composed by the side hole array was published by the same group[32]. The negative modulus behavior is observed below the cut-off frequency of side hole. Short after, the same group combines these two technologies (membrane array and side hole) to achieve double negative behavior from 0 to 500 Hz[33] and the nonlinear effect of this double-negative metamaterials system is discussed by Fan et al[36]. By replacing the air medium by water, the negative modulus behavior based on Helmholtz resonator structure is improved from hertz range to kilohertz range[34].

The double-negative metamaterials based on Helmholtz resonator and membrane array structure are demostrated by Lee etal[35] in Fig. 1.7(a). There are three transition frequencies

observed in the system, which shows the four types of metamaterials, namely single negative density, double negative, negative modulus and double negative regions in a sequence of low frequency to high frequency (Fig. 1.7(b)). The measurement setup is similar as the previous publication [33] and phase velocity is calculated by the phase shift between two detectors placed at a given distance. The experimental results shows a good agreement with transmission line model, which demonstrates a double negative range between 210 kHz to 310 kHz in Fig.1.5 (c) and (d).

Other method is called decorated membrane resonator[30, 29, 11], which have been explored for superresolution, acoustic metasurface and phase manipulation. Compared with most of membrane-based acoustic metamaterials which only produces the negative density behavior[28], the decorated membrane system can produce more different vibration modes or called the monopolar and dipolar in the system, which will generate the resonator coupling between different resonator. These resonator-coupling will break the symmetric of the system and cause the dispersive acoustic behavior of the whole structures. Yang et al[30] reported a double-negative metamaterials by two coupled decorated membranes resonating structure and the schematic is as shown in Fig.1.6 (a). The resonator includes two pre-stress circular membranes, which is decorated a rigid mass plate in the center position of membranes. These two decorated membranes were connected by an acrylic plastic ring and fixed on a right side wall to apply an 1.3 $\times 10^6$ Pa pre-stress on membrane. The normal displacement of the membrane were characterized by laser vibrometer on the top membrane to analyze the vibration mode of the membrane.

As shown in the Fig.1.6(b)-(d), there are three types of vibration modes observed by this structures, including two monopolar resonances and one dipolar resonance. Under the monopolar resonances, the mass in the center of membrane vibrate out-of-phase (negative modulus) and under the dipolar resonance (negative density), the two disks vibrate in phase. The double-negative behavior demonstrates the overlap range of monopolar and dipolar resonance. Compared with traditional two coupled membrane resonators, the in-phase dipolar eigenmodes are preserved,

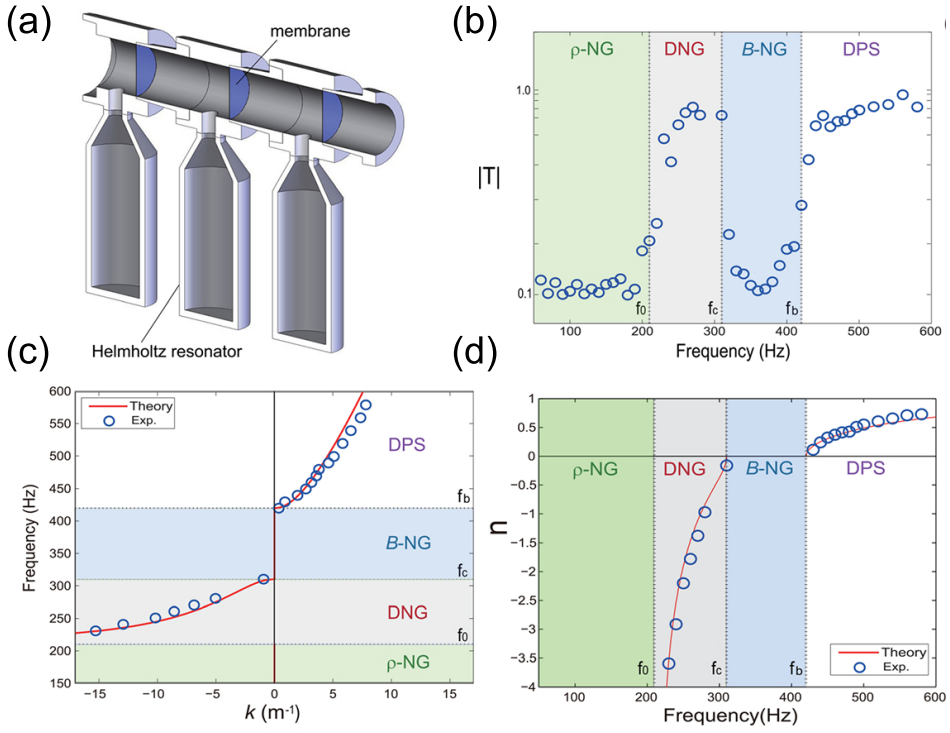


**Figure 1.5**: Double negative metamaterials based on Helmholtz resonator and membrane array[33]: (a) Helmholtz resonator and elastic membrane composite structure, (b) Transmission spectrum; (b) Wave vector; (c) Refractive index;

which maintains the negative density behavior. Meanwhile, a monopolar eigenmode is produced by the out of phase oscillation of central mass, which leads a frequency-dispersive effective bulk modulus. The effective density $\bar{\rho}$ of the system can be expressed by the following equations:

$$\bar{\rho} = \frac{1}{\omega^2 d} \frac{\langle P \rangle}{\langle W \rangle} \tag{1.2}$$

where $\langle P \rangle$ is the average pressure difference between the two sides of membrane, $\langle W \rangle$ is the averaged acceleration of the membrane and $d$ is the average thickness of the decorated membrane. The effective density as the function of frequency is shown in the Fig.1.6(e). At the two eigenfrequency resonance, the effective density is equal to zero, which shows a 100% transmission as well. There is also a particular point observed between two resonant peaks, which is the antiresonant frequency of the system as discussed previously. At this antiresonant frequency, the sign of of $\bar{\rho}$

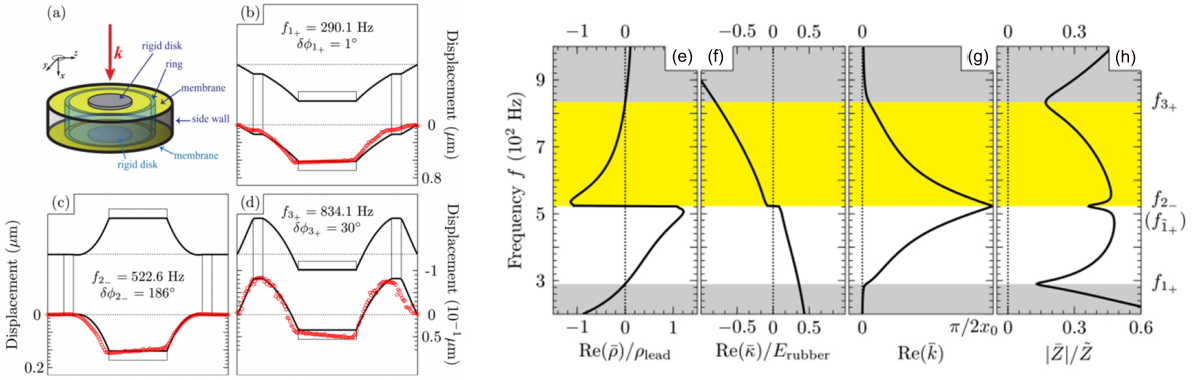


**Figure 1.6**: (a) Schematic of coupled decorated membrane resonator (b), (c) and (d) three eigenmodes of resonator including two monopolar resonance and one dipolar resonance. (e) Effective density; (f) Effective bulk modulus; (g )Real part of the effective wave vector; (h) Acoustic effective impedance.

is changed from positive to negative, which causes all the propagating wave is reflected. This specified properties have been utilized to realize the lightweight reflective system to block the low-frequency noise.

The displacement decomposition is discussed in the paper to study the coupling between the membrane and medium. When the acoustic wave propagates through the membrane-fluidic medium, the dispersion relation is given by

$$k_{\parallel}^2 + k_{\perp}^2 = (\pi/\lambda)^2 \tag{1.3}$$

where $k_{\perp}^2$ is the normal wave vector decomposed component and $k_{\parallel}^2$ is the wave vector along the membrane displacement direction. Considering the radius of membrane and acoustic wavelength ($2\pi/2R > 2\pi/\lambda$), the perpendicular decomposition of wavenumber follows $k_{\perp}^2 < 0$. Therefore, the fine details of membrane displacement is only related to evanescent modes and surface averaged normal displacement of membrane can be assumed as a piston motion, which is coupled to the acoustic radiation mode[11, 30].

Based on this principle, Ma[11] demonstrated an acoustic metasurface with hybrid resonance, which can match the airbone acoustic impedance with tunable frequencies. The pre-stress

membrane with the central mass is fixed on a cavity structure, which sealed a $SF_6$ gas inside. Because of the membrane displacement variance component is much larger than the wave number value, there is a very weak dissipation effect appearing at the resonant frequency. This metasurface shows a remarkable acoustic property, which is above 99% absorption coefficient at the resonance with subwavelength unit cell length and low-dissipation factor. To evaluate the dissipation effect, the vibration profile at the resonance and anti-resonance frequency is measured by LDV and the dissipation was considered by adding the isotropic structural loss factor of membrane in the COMSOL Multiphysics FEM methods. The dissipated factor is fitted by experimental results according to the following equation:

$$\langle G_M \rangle = \sum_{i=1}^{2} \frac{\|\langle W_i \rangle\|^2}{\rho_i(\omega_i^2 - \omega^2)} + \sum_{i=1}^{2} \frac{\|\langle W_i \rangle\|^2 \omega}{\rho_i(\omega_i^2 - \omega^2)} \tag{1.4}$$

where $\langle G_M \rangle$ is the surface-averaged Green function, $\langle W_i \rangle$ is the average membrane displacement and $\rho_i$ is the displacement-weighted mass density parameter at $i$th eigenmode. The surface-average displacement $\langle W_h \rangle$ is close to the amplitude of incident sound and there is a significant amplification of displacement at the anti-resonant frequency, which means the absorption behavior caused by the membrane lossy but not the dissipation. This decorated-membrane metasurface provides a promising application potentials in acoustic filter and sensor and the strong absorption at antiresonance is expected for piezoelectric application with the high conversion efficiency.

### 1.1.4 Acoustic Transformation Theory

Transformation theory, which is developed by Cummer and Pendry theory[37, 38], has been widely utilized for experimental demonstration 3D acoustic cloaks in microwave, optical and acoustic frequency range[39, 40, 13, 12]. Based on this theory, Jing etal[41], proposed an acoustic complementary metamaterials (CMM), which is able to restore the acoustic field

behind the skull barrier at 50 kHz. The acoustic coordinate transformation methods is utilized to match the effective parameters of biological layer. The effective density tensor of CMM and aberrating layer are namely $\rho^{(c)}(x^{(c)},y^{(c)},z^{(c)})$ and $\rho^{(a)}(x^{(a)},y^{(a)},z^{(a)})$. The compressibility tensors are $\beta^{(c)}(x^{(c)},y^{(c)},z^{(c)})$ and $\beta^{(a)}(x^{(a)},y^{(a)},z^{(a)})$. $x^{(c)},y^{(c)},z^{(c)}$ and $x^{(a)},y^{(a)},z^{(a)}$ are coordinates of CMM and aberrating layer. Therefore, the effective density of CMM can be expressed by following equation[41, 38]:

$$[\rho^{(c)}]^{-1} = \mathbf{A}[\rho^{(a)}]^{-1}\mathbf{A}^T/\det\mathbf{A} \tag{1.5}$$

$$\beta^{(c)} = \beta^{(a)}/\det\mathbf{A} \tag{1.6}$$

where A is the Jacobian transformation tensor of compressing transformation given by

$$\mathbf{A} = \begin{bmatrix} \frac{\partial x^{(c)}}{\partial x^{(a)}} & \frac{\partial x^{(c)}}{\partial y^{(a)}} & \frac{\partial x^{(c)}}{\partial z^{(a)}} \\ \frac{\partial y^{(c)}}{\partial x^{(a)}} & \frac{\partial y^{(c)}}{\partial y^{(a)}} & \frac{\partial y^{(c)}}{\partial z^{(a)}} \\ \frac{\partial z^{(c)}}{\partial x^{(a)}} & \frac{\partial z^{(c)}}{\partial y^{(a)}} & \frac{\partial z^{(c)}}{\partial z^{(a)}} \end{bmatrix} \tag{1.7}$$

The density and modulus of aberrating layer to mimic the biological layer is 2000 kg/$m^3$ and 12.5 GPa. Assuming the thickness of acoustic metamaterials is half of the biological layer, the effective density in x direction, in y direction and modulus of metamterials is -1000 kg/$m^3$, -4000 kg/$m^3$ and 6.25 GPa. A membrane-based metamaterials is designed to achieve the designed effective parameters and the equivalent circuit is to approximate the effective parameter theoretically. Fig. 1.7 shows the acoustic intensity field with and without the acoustic metamaterials applying on the biological layer. The intensity with acoustic metamaterials is about 88% at the focused point, whereas the transmission drops to 31% without acoustic metamaterials. Although the acoustic metamaterials needs to be optimized for different biological layer and the losses needs to be considered as well in the metamaterials, this proposed metamaterials have been proved to

improve the ultrasonic transmission through biological layer with appropriate effective parameters.

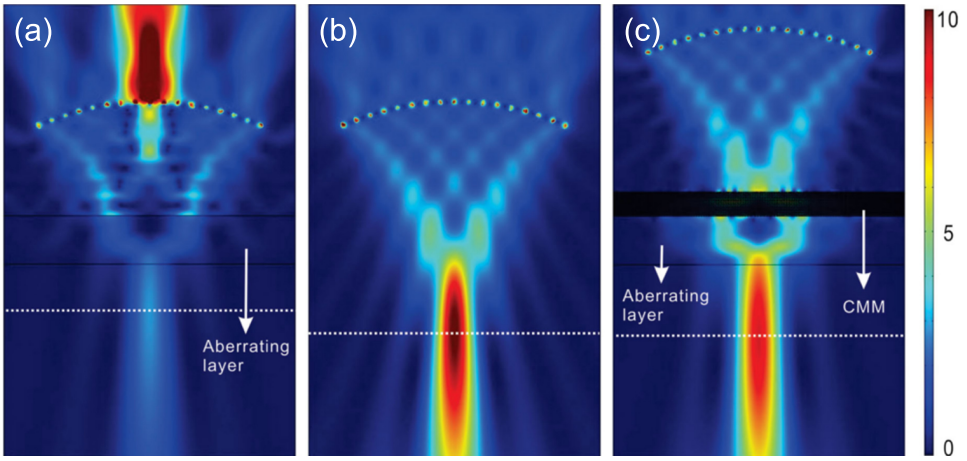


**Figure 1.7**: Acoustic intensity field mapping for focused acoustic beam[41]: (a) Biological layer only; (b) Medium only; (c) CMM+biological layer.

### 1.1.5 Retrieve the effective density and modulus of metamaterials

In order to match the density and modulus of biological layer, the effective density and modulus of double negative metamaterials needs to be demonstrated beforehand to match the biological layer at the working frequency according to the acoustic transform theory. Fokin etal[42] extends the method from electromagnetic materials to extract the acoustic parameters of acoustic metamaterials. When a plane wave propagates through the metamaterials, which is placed between two liquid media, the reflection ($R$) and transmission ($T$) coefficient can be expressed as:

$$R = \frac{Z_2^2 - Z_1^2}{Z_1^2 + Z_2^2 + 2iZ_1Z_2\cot\phi} \tag{1.8}$$

$$T = \frac{1+R}{\cos\phi - Z_2 i\sin\phi/Z_1} \tag{1.9}$$

where $rho_1$ and $rho_2$ are the density of liquid medium and metamaterials, $c_1$ and $c_2$ are the

sound speed of liquid medium and metamterials, $Z_o = \rho_i c_i \theta_i$ is acoustic impedance, $\phi = \pi f d / c_2$ is the phase change across metamaterials, $f$ is the working frequency and d is the metamaterials thickness. Introducing acoustic impedance $\xi = \rho_2 c_2 / \rho_1 c_1$, wave number $k = \omega / c_1$ and refractive index $n = c_1 / c_2$, we obtain

$$R = \frac{\tan(nkd)(1/\xi - \xi)i}{2 - \tan(nkd)(1/\xi + \xi)i} \tag{1.10}$$

$$T = \frac{2}{\cos(nkd)[2 - \tan(nkd)(1/\xi + \xi)i]} \tag{1.11}$$

By inverting Eqs. 1.10 and 1.11, The acoustic impedance $\xi$ and refractive index $n$ is obtained.

Meanwhile, additional constraints need to be imposed which to prevent the ambiguity of equations. For passive metmaterials, the real part of $\xi$ should be positive and imaginary part of $n$ should be negative. To overcome the problems, the Eqs. 1.10 and 1.11 can be rewritten in the form:

$$\xi = \frac{r}{1 - 2R + R^2 - T^2},\ n = \frac{-i\log x + 2\pi m}{kd} \tag{1.12}$$

where

$$r = \mp\sqrt{(R^2 - T^2 - 1)^2 - 4T^2}, x = \frac{1 - R^2 + T^2 + r}{2T} \tag{1.13}$$

And the effective density ($\rho_{\text{eff}}$) and modulus ($B_{\text{eff}}$) of metamaterials can be expressed by the following equations:

$$\rho_{\text{eff}} = n\xi,\ B_{\text{eff}} = \frac{\xi}{n} \tag{1.14}$$

According to Eqn. 1.14, the effective parameters of metamaterials can be retrieved when the transmission and reflection coefficient of metamaterials is known. And the experimental

and theoretical methods to characterize the transmission and reflection coefficient of unknown acoustic metamaterials will be discussed in the Sec. 1.1.6

### 1.1.6 Transmission and reflection coefficient

As discussed in Sec.1.1.5, the reflection and transmission coefficient of the medium are the crucial components to retrieve the effective density and modulus. There are several methods to extract the reflection and transmission coefficient, namely the transfer matrix[43] and scattering matrix[44, 45]. The origin of these paper can trace back to this standard[43]. The value of $R$ and $T$ can be extracted from the COMSOL Multiphysics by acoustic transmission line theory which is well built and discussed in Ref. [44, 45].

In principle, the plane-wave transducer is placed at the end of acoustic standing wave tube and four receivers are used to measure the sound pressure including the amplitude and phase information in four different positions($x_1$ to $x_4$), which shows:

$$p_1 = (ae^{-jkx_1} + be^{-jkx_1})e^{j\omega t} \tag{1.15}$$

$$p_2 = (ae^{-jkx_2} + be^{-jkx_2})e^{j\omega t} \tag{1.16}$$

$$p_3 = (ce^{-jkx_3} + de^{-jkx_3})e^{j\omega t} \tag{1.17}$$

$$p_4 = (ce^{-jkx_4} + de^{-jkx_4})e^{j\omega t} \tag{1.18}$$

where ks is the wave number of measured sample. $p_1$ to $p_4$, represent the plane waves in these four measured position. The amplitude of pressure of four receivers ($a$, $b$, $c$, $d$) can be expressed

by the following equations:

$$a = \frac{j(p_1 e^{jkx_2} - p_2 e^{jkx_1})}{2\sin k(x_1 - x_2)} \tag{1.19}$$

$$b = \frac{j(p_2 e^{jkx_1} - p_1 e^{jkx_2})}{2\sin k(x_1 - x_2)} \tag{1.20}$$

$$c = \frac{j(p_3 e^{jkx_4} - p_4 e^{jkx_3})}{2\sin k(x_3 - x_4)} \tag{1.21}$$

$$d = \frac{j(p_4 e^{jkx_2} - p_3 e^{jkx_4})}{2\sin k(x_3 - x_4)} \tag{1.22}$$

So the S matrix [S] can be obtained based on the incoming and outgoing wave before and after the targeted measured materials.

$$\begin{pmatrix} b \\ ce^{jks} \end{pmatrix}_{\text{Reflected}} = \begin{pmatrix} S_{11} & S_{12} \\ S_{21} & S_{22} \end{pmatrix} \begin{pmatrix} a \\ ce^{jks} \end{pmatrix}_{\text{Incident}} \tag{1.23}$$

In order to solve four unknown variables in Eq. 1.23, the additional equation is necessary by changing the load (or called changing the boundary condition) at the end of acoustic impedance tube eg. sound hard boundary condition or plane wave boundary condition. We use ($a_1$, $b_1$, $c_1$, $d_1$) and ($a_2$, $b_2$, $c_2$, $d_2$) to express the different amplitudes under different loading, the components of S matrix can be obtained as:

$$S_{11} = \frac{b_1 d_2 e^{jks} - b_2 d_1 e^{jks}}{a_1 d_2 e^{jks} - a_2 d_1 e^{jks}} \tag{1.24}$$

$$S_{12} = \frac{a_1 b_2 - a_2 b_1}{a_1 d_2 e^{jks} - a_2 d_1 e^{jks}} \tag{1.25}$$

$$S_{21} = \frac{c_1 e^{-jks} d_2 e^{jks} - c_2 e^{-jks} d_1 e^{jks}}{a_1 d_2 e^{jks} - a_2 d_1 e^{jks}} \tag{1.26}$$

$$S_{22} = \frac{a_1 c_2 e^{-jks} - a_2 c_1 e^{-jks}}{a_1 d_2 e^{jks} - a_2 d_1 e^{jks}} \tag{1.27}$$

s is the thickness of measured materials.

Eqn. 1.27 can be simplified when the acoustic system is a symmetrical network system, which the $S_{11} = S_{22}$ and $S_{12} = S_{21}$ Meanwhile, when the anechoic materials are applied at the end of tubing, all the reflection sound is absorbed and then $d$=0. Reflection and Transmission coefficient are shown as following equations:

$$R = S_{11} = S_{22} = \frac{b}{a} \tag{1.28}$$

$$T = S_{12} = S_{21} = \frac{c}{a} e^{-jks} \tag{1.29}$$

### 1.1.7 Biological skull barrier to ultrasound

Ultrasonic waves, which are known as a efficient and non-invasive imaging method, can excite the neurons to evoke the electrical potential for neuromodulation as well[46, 47, 48]. The first for tissue ultrasonic stimulation can dates back to 1929 on fog's static nerves[49].Current technology is using 43 MHz high intensity focused ultrasound (HIFU) to reach 90 μm resolution stimulation in salamander retina by 'open water' methods[50]. Meanwhile, HIFU was found to heat the brain tissues for tumor therapy by reaching necrotic treatment temperature, which is performed as a non-surgical and radiation free procedure for cancer treatment.

However, the attenuation and scattering effect of the cranial bone will cause the strong transmission loss through the skull structures[51]. The high-surface-area-to-volume ratio cancellous bone layer, which is localized between the two cortical bones, contributes most of the absorption to acoustic wave[51, 52]. There is a very high insertion ultrasonic loss ($\sim$ 60 dB) at 2 MHz. The main loss comes from the impedance mismatch between the skull and tissue ($Z_{bone}/Ztissue = 5$). And the dipole structure in the cancellous bone, which absorbs acoustic energy and transform as heat energy, also causes the scattering loss. Pinton et al[52] studied the attenuation, scattering and aborption effect of ultrasound in skull bone. Figure shows the experimental setup and temperature rising which is characterized by IR camera. Nine skull samples

with average thickness of 7.62 $\pm$ 0.46 and 4.63 $\pm$ 0.48 diople thickness were characterized and attenuation is about $-13.3 \pm 0.97$ dB. And the maximum temperature rising difference caused by the absorption is 9.88 $\pm$ 2.82. White etal measured the transcranial ultrasonic transmission between 0.6 and1.4 MHz by using broadband pulse[51]. There is a rapid drop in the transmission spectrum with the increase of excitation frequency and most of the acoustic wave will reflect at the interface between the water and skull. Therefore, how to solve the reflection on the interface between the water and skull is the main topic to improve the high-frequency acoustic transmission through the skull.

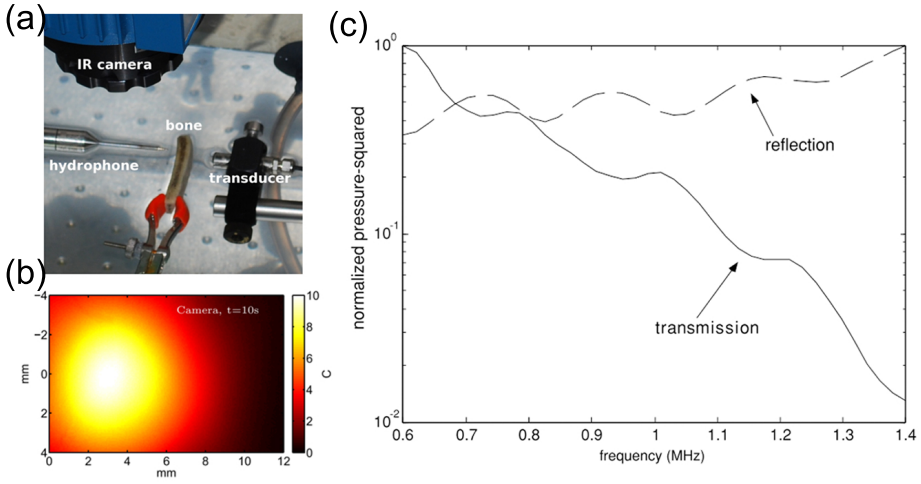


**Figure 1.8**: Attenuation effect and scattering effect of human skull[51, 52]: (a) Experimental setup; (b) Temperature rising after 10 second 1 MHz ultrasound exposure; (c) Normalized transmission and reflection pressure.

## 1.2 Current Limitation and Our Solution

### 1.2.1 Current Limitations

As discussed in the previous sections, there is very high inserted ultrasonic loss mainly caused by the interface reflection between the medium and skull, which can be efficient improved if the appropriate metamaterials are applied to match the parameters of biological layer. Several

publications reported the double negative metamaterials based on the Helmholtz resonator and membrane array or other decorated structure. However, the working frequency of the system is below 30 kHz, which is far lower than the ultrasonic frequency. In order to utilize for biomedical ultrasonic application, the working frequency of double negative band is required to reach kilo-hertz or mega-hertz range. With respect to achieve this frequency, new fabrication method is required for high-frequency application.

### 1.2.2 Current Approaches

In order to deliver the ultrasonic acoustic wave through biological layer, saying skull bone, low ultrasonic frequency transducer ($\sim$200 kHz) is expected for treatment to increase the wavelength of ultrasonic wave. When the wavelength of the ultrasound is larger than the thickness of biological layer, the attenuation and aberration effect can be ignored. However, low-working frequency and long wavelength also means High-frequency ultrasound (above 1 MHz) was also utilized for brain lesions and disorder treatment, but the aberration effect must be corrected beforehand by characterize and analyze the skull CT-morphology. To correct the wavefront phase position and focus point, the wave propagating and interaction with skull was studied by finite difference time domain (FDTD) solution and the ultrasonic time reversal correction methods were well-established to emit the ultrasonic wave at the focus location[53, 54, 55, 56]. In vivo experiment, the phase-array transducer and one hydrophone was placed behind the skull to map the ultrasonic acoustic intensity. But in the patient's therapy, it is very hard to correct the acoustic intensity and estimate the focus point by skull CT-morphology to reconstruct the skull because of complex skull's microstrucutre.

Another way is to discover a new double negative metamaterial component to reach high-working frequency above mega-hertz range. As proven in Sec., there is a huge transmission enhancement if the effective density and modulus of double-negative metamaterials match the properties of biological layer. However, there are no specific studies on metamaterials which

work in near or beyond mega-hertz frequency.

## 1.3 Our Solution and Objectives

We start to design a double-negative metamaterials based on micro-meter scale silicon nitride membrane and Helmholtz resonator to target above 1 MHz working frequency double negative metamaterials. We calculate the dispersion curves of helmholtz resonator and membrane-based metamaterials. We also suppose a new approach to enhance the acoustic transmission through the biological layer by applying the double-negative metamaterials. According to the simulation results, we use a microfabrication method to build the acoustic metamaterial, which can achieve up to 1 MHz working frequency. In summary, our objectives are as followed:

• Design the double negative metamaterials composed by helmholtz resontor and membrane component by COMSOL Multiphysics FEM methods;

• Experimental realization of 200 kHz metamaterials unit cell design and characterize the acoustic properties of the unit cell structure by Laser Doppler Vibrometer;

• Study the vibration behavior of high-stress silicon nitride membrane in water and estimate water mass effect on the resoance frequency reduction of silicon nitride membrane.

• Discover a novel fabrication method to integrate functional nanomaterials into three dimensional structure for high-surface, high-compacted functional device.

## 1.4 Outline of Chapters to Follow

Chapter 2 will present our first metamaterials design between 250 kHz to 400 kHz. The dispersion relations, transmission spectrum of negative-density, negative modulus and double-negative metamaterials, which is composed by micro-meter scale silicon nitride membrane and Helmholtz resonator. The experimental realization of unit cell structure and acoustic characteriza-

tion will be presented as well. In Chapter 3, we study and discuss the vibration behavior of silicon nitride membrane in water, which indicates the possibility to improve the working frequency of double negative metamaterials to megahertz range. To further improve the double-negative band frequency, a novel fabrication strategy to integrate the suspended thin film method is presented in Chapter 4, which provides the possible to control the period length between the membrane components from 2 μm to 15 μm. Functional nanomaterials, namely the metallic nanostructures and semiconducting quantum dots also could be integrated on the suspended film by the same method. Chapter 5 will conclude the important points of this dissertation and propose the promising research topics for biomedical ultrasonic application.

# Chapter 2

# Design and Fabrication of Acoustic Unit Cells for Negative Refractive Index Metamaterials for Near-Megahertz Enhanced Acoustic Transmission

## 2.1 Introduction

The field of acoustic metamaterial engineering has grown significantly over the past two decades [57, 4, 58, 59], as it has demonstrated the ability to create unprecedented and beneficial material behaviors. Arguably the most counter-intuitive and desired behavior has been the realization of a negative acoustic refractive index, which has been predicted, among other features, to enable imaging beyond the diffraction limit [7]. Such negative index materials simultaneously exhibit a negative effective density and a negative elastic modulus, and are achievable through the proper design of arrays of locally resonant elements [4, 6, 60, 61, 62, 63, 33, 23, 64, 65]. The finite element method (FEM) has furthermore been used to show that negative index materials,

when matched appropriately to a high-impedance layer, could act to effectively "cancel" acoustic wave reflections from, and enhance transmission through the layer. The metamaterial thus acts as a "complementary acoustic material" (CAM) [7, 66, 41, 67].

In Ref. [41], it was suggested that a CAM could be used to improve biomedical ultrasound imaging through dense layers positioned between the transducer and the medium of interest, for example, imaging the brain through the skull. This capability could also be used in concert with other demonstrated techniques aimed at enhancing ultrasonic signal quality, including time reversal, phase conjugation, and phased array methods [68, 54, 69]. However, existing negative refractive index metamaterials operate at much lower frequencies—around tens of kHz frequencies or below—than biomedical ultrasound, which is conducted at $\sim$2 to 15 MHz for most diagnostic imaging techniques,[70] and $\sim$0.25 to 2 MHz for high intensity focused ultrasound [71, 72]. The few examples of negative index acoustic metamaterials operating in this frequency regime have furthermore only been demonstrated in systems that would have poor energy transmission into, and compatibility with, biological materials [73]. For instance, the initial proposal for using a complementary material to cancel aberrating layers operated at $\sim$50 kHz[41]. To deliver a suitable metamaterial for biomedical applications, the locally resonant elements must be made at far smaller scales, posing significant design and fabrication challenges.

In this work, we present the design and analysis of a near-MHz negative effective refractive index acoustic metamaterial that is indented for use in biomedical ultrasound applications. We analytically and numerically calculate the dispersion band diagrams for the resonant elements of our metamaterials, and retrieve the effective densities, elastic moduli, and refractive indices of the acoustic metamaterial from these results. Via these simulations, we furthermore demonstrate the ability of our metamaterial design to serve as a CAM, and complement a high impedance layer to enhance the passage of ultrasound through it. Finally, we present experiments that serve to validate the design of the metamaterial's unit cell structure through acoustic wave transmission measurements which we compare with our analytical and numerical results.

## 2.2 Design and properties of the structure

The concept of extraordinary ultrasound transmission through a high impedance layer using a CAM [41] is shown in Figure 2.1(a). The proposed CAM structure[60, 33] is composed of a two-dimensional array of $SiN_x$ membranes that produce a negative effective density[28, 74, 75] and Helmholtz resonators that produce a negative effective modulus[34, 76, 32, 77]. In this study, we only investigate the effective properties of one-dimensional (1D) chains of the constitutive blocks, as are shown in Fig. 2.1(b). It is known that by tuning the resonant frequencies of each element, a *double negative frequency range* can be achieved where both the density and modulus are negative, and the phase velocity opposes the group velocity. Since the periodicity (unit cell length $D$) of our proposed metamaterial is smaller than the corresponding wavelength in water ($D \sim \lambda/7$ at 1 MHz), the metamaterial can be considered to be a strongly dispersive, homogenized medium. In the following section, we use an analytical lumped element model[78] to describe the dispersion of metamaterials composed of: *i*) only membranes, *ii*) only Helmholtz resonators, and *iii*) membranes and Helmholtz resonators together.

### 2.2.1 Dispersion band diagram

A membrane-based acoustic metamaterial exhibits a dispersion relation of $k = \omega\sqrt{\rho_{\text{eff}}/B_0}$, where $k$ is the wave number, $\omega$ is the angular frequency, $B_0 = \rho_0 c_0^2$ is the bulk modulus of water, and $c_0$ is the sound speed in water. The water density is denoted as $\rho_0$ and the effective metamaterial density as $\rho_{\text{eff}}$. The latter can be expressed as

$$\rho_{\text{eff}} = \rho' \left(1 - \frac{\omega_{0m}^2}{\omega^2}\right), \tag{2.1}$$

where $\rho' = M/V$ is the average density, $M$ is the total mass, $V$ is volume of fluid in the unit cell, and $\omega_{0m}$ is the membrane's fundamental resonant frequency. In the analytical lumped model, the membranes do not influence the effective modulus of the metamaterial.

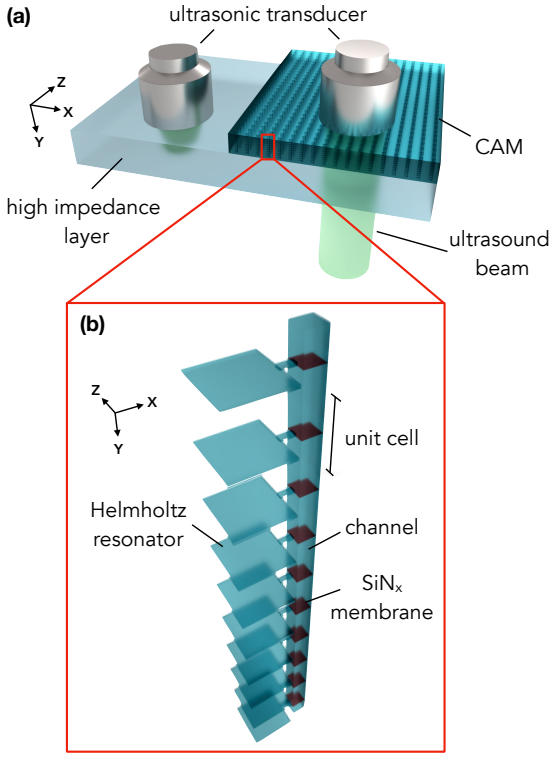


**Figure 2.1**: (a) Principle of extraordinary acoustic transmission via complementary acoustic metamaterials (CAMs). (b) One-dimensional chain CAM composed of a channel with periodically assembled $SiN_x$ membranes and Helmholtz resonators.

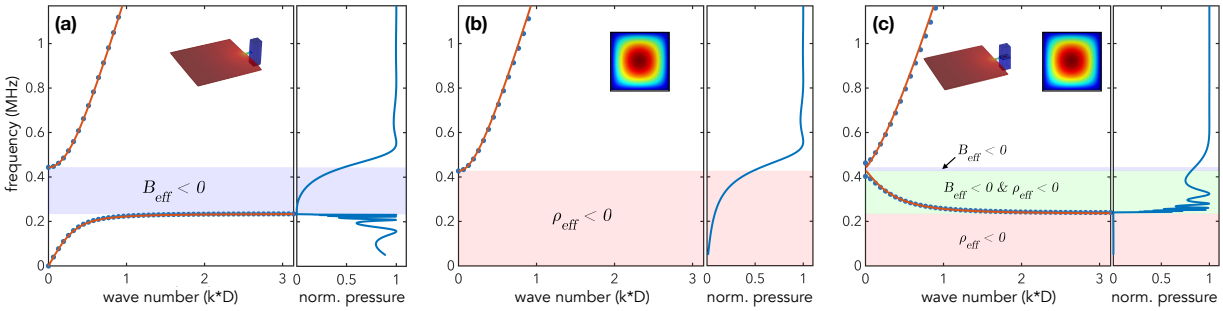


**Figure 2.2**: Dispersion curves for infinitely long metamaterials for the (a) Helmholtz resonator, (b) membrane, and (c) membrane and Helmholtz resonator together, where $\omega_{0H}/(2\pi) = 0.23$ MHz, $\omega_{1H}/(2\pi) = 0.44$ MHz, and $\omega_{0m}/(2\pi) = 0.43$ MHz. The red solid line corresponds to analytical predictions from Ref. [lee2016origin], while the blue markers and blue solid line correspond to our FEM results. The negative density/modulus regions are depicted by a colored background (blue $\equiv B_{\text{eff}} < 0$, red $\equiv \rho_{\text{eff}} < 0$, green $\equiv B_{\text{eff}} < 0$ and $\rho_{\text{eff}} < 0$). The right panels of each subfigure show the normalized transmitted acoustic pressure through a ten unit cell long structure as a function of the frequency.

The dispersion relation of a Helmholtz-resonator-based acoustic metamaterial is defined as: $k = \omega\sqrt{\rho_0/B_{\text{eff}}}$, where $B_{\text{eff}}$ is the effective modulus, and its related compressibility $B_{\text{eff}}^{-1}$ is expressed as

$$B_{\text{eff}}^{-1} = B_0^{-1}\left(1 + \frac{\omega_{1H}^2 - \omega_{0H}^2}{\omega_{0H}^2 - \omega^2}\right), \tag{2.2}$$

where $\omega_{0H}$ is the Helmholtz resonator frequency and $\omega_{1H}$ is the resonance corresponding to the Helmholtz resonator connected to the channel[78, 79]. Following the lumped element model, the metamaterial's effective density is not influenced by the Helmholtz resonator and is assumed to be the density of water. Other studies[80] have shown that while the effective density can indeed vary around $\omega_{0H}$, the constant density assumption remains sufficiently accurate for predicting the effective modulus. In our study, the resonant frequencies of membranes and Helmholtz resonators are estimated via FEM simulations (COMSOL Multiphysics version 5.3, COMSOL Inc, www.comsol.com) and then implemented in the analytical model. The resulting dispersion relations for Helmholtz resonators and membranes, each alone, are shown in Fig. 2.2(a) and (b), respectively, as red solid lines. Finally, the dispersion relation of the combined Helmholtz resonator and membrane can be expressed as $k = \omega\sqrt{\rho_{\text{eff}}/B_{\text{eff}}}$, as is plotted in Fig. 2.2(c), also as a red solid line.

These analytical estimates are compared to FEM simulation eigenfrequency analysis that is conducted on the specific, three-dimensional one-unit cell geometry shown in Fig. 2.1(b). A cavity 500×500×10 μm in size is connected to the main channel via a neck of 50×20×10 μm to form a Helmholtz cavity. The main channel and the membranes across it both have a square cross section of 70×70 μm. The membranes have a thickness of 660 nm formed from silicon nitride ($SiN_x$). The membrane pre-stress is set at 400 MPa, as calculated from the wafer curvature film stress measurements of the experimentally fabricated membranes, which is described later. All the boundaries of the structure are modeled as acoustically rigid walls, except the channel

extremities, where Floquet boundary conditions are applied to simulate a periodically infinite system. The entire structure is assumed to be filled by water with a density $\rho = 1000$ kg/m$^3$ and bulk modulus $B_0 = 2.19$ GPa.

We simulate three different unit cells: *i*) the channel and one Helmholtz resonator, *ii*) the channel and one membrane, and *iii*) the channel, one Helmholtz resonator, and one membrane. For all cases, the length of the unit cell is $D = 200$ μm. For this configuration, the resonance frequencies are estimated via FEM simulations to be $\omega_{0H}/(2\pi) = 0.23$ MHz, $\omega_{1H}/(2\pi) = 0.44$ MHz, and $\omega_{0m}/(2\pi) = 0.43$ MHz. The simulated dispersion curves are shown in Fig. 2.2 as blue markers, and the regions of negative density, negative modulus, and doubly negative material properties are highlighted with colored backgrounds (blue $\equiv B_{\text{eff}} < 0$, red $\equiv \rho_{\text{eff}} < 0$, green $\equiv B_{\text{eff}} < 0$ & $\rho_{\text{eff}} < 0$). For each case, we also present the normalized acoustic pressure transmitted through a ten unit-cell-long structure as a function of the frequency as a solid blue line. Plane wave radiation boundary conditions are used for the channel extremities, so that a plane wave is emitted from one end of the channel towards the other end. Recognizing that the shortest investigated wavelength (corresponding to the highest frequency of operation) is $\lambda_{\text{min}}$, the size of the mesh elements were restricted to $\lambda_{\text{min}}/15$ or smaller, and the frequency increment was set at 1 kHz to retain sufficient accuracy in the analysis. The reported pressure is normalized by the incident pressure.

The analytical model and the FEM simulations of the dispersion relations in Fig. 2.2 show good agreement in all three cases. In Fig. 2.2(a), the Helmholtz resonators' band structure shows a band gap between the natural frequencies of the resonators, where the effective modulus is negative. The transmission clearly drops in the band gap region. The phase velocity ($v_p = \omega/k$) and effective modulus becomes infinite at $\omega = \omega_{1H}$. In Fig. 2.2(b), the membranes alone produce a band gap at low frequencies, $\omega < \omega_{0m}$, which can also be seen via the transmission drop. At $\omega = \omega_{0m}$, the effective density is equal to zero. For metamaterials composed of both membranes and Helmholtz resonators, the dispersion relation plotted in Fig. 2.2(c) shows two band gaps, one at

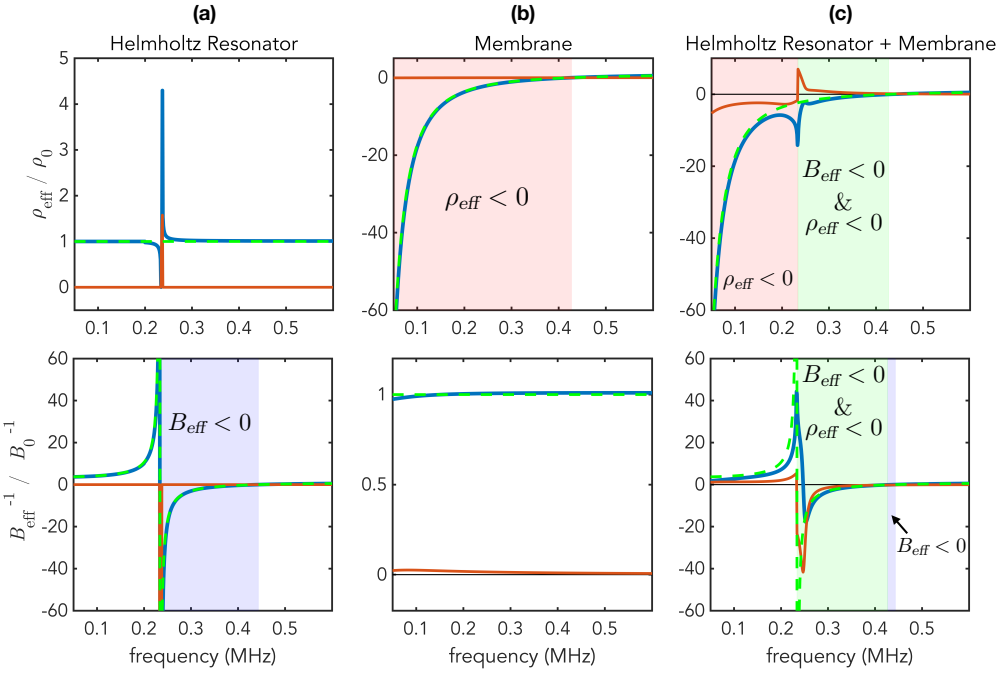


**Figure 2.3**: Effective densities and moduli for the (a) Helmholtz resonator, (b) membrane, and (c) combined membrane and Helmholtz resonator. The real and imaginary portions of the FEM analysis are plotted as solid blue and red lines, respectively, while the dashed green lines correspond to the analytical model. The negative density, negative modulus, and doubly negative regions are highlighted by colored backgrounds (blue $\equiv B_{\text{eff}} < 0$, red $\equiv \rho_{\text{eff}} < 0$, green $\equiv B_{\text{eff}} < 0$ and $\rho_{\text{eff}} < 0$).

$\omega < \omega_{0H}$ corresponding to negative density, and a narrow one at $\omega_{0m} < \omega < \omega_{1H}$ that corresponds to a negative modulus. The propagating negative index region appears over $\omega_{0H} < \omega < \omega_{0m}$, between 0.23 MHz and 0.43 MHz. Some oscillations are visible in the transmission spectrum shown in Fig. 2.2(a,c) for the ten unit-cell structure over the frequency range corresponding to the lower propagating branch of the systems. These oscillations are due to acoustic interactions between the unit cells, and the total number of peaks (or resonances) should be, and is, equal to the number of unit cells in the structure.

### 2.2.2 Estimation of effective properties

The effective properties of the metamaterials were calculated via FEM analysis using the method developed by Fokin *et al.*[42], wherein the effective refractive index $n$ and acoustic

impedance $Z$ is extracted from reflection and transmission coefficients. The effective mass density and sound speed are then calculated from $n$ and $Z$. For plane waves normally incident on a sample of density $\rho_{\text{eff}}$ and sound speed $c_{\text{eff}} = \sqrt{B_{\text{eff}}/\rho_{\text{eff}}}$ placed between two identical media—in our case, water—on both sides, the refractive index is

$$n = \frac{c_0}{c_{\text{eff}}} = \pm \frac{\cos^{-1}\left(\frac{1}{2T}[1-(R^2-T^2)]\right)}{kd} + \frac{2\pi m}{kd}, \tag{2.3}$$

and the acoustic impedance is

$$Z = \frac{\rho_{\text{eff}} c_{\text{eff}}}{\rho_0 c_0} = \pm \sqrt{\frac{(1+R)^2 - T^2}{(1-R)^2 - T^2}}, \tag{2.4}$$

where $R$ and $T$ are the reflection and transmission coefficients, $d$ is the thickness of the sample, and $m$ is the branch number of the arccosine function (which is equal to zero for a single unit cell). We note that both the refractive index and impedance are complex functions. From Eqs. (2.3) and (2.4), the effective density and modulus may be written as $\rho_{\text{eff}} = nZ\rho_0$ and $B_{\text{eff}}^{-1} = (n/Z)B_0^{-1}$, respectively.

To estimate the reflection and transmission coefficients for a wave propagating through our metamaterial, we placed a single constitutive block of the metamaterial at the center of a channel of dimension $70\times70\times200$ μm in our simulation, and implemented a scattering matrix formalism via a four-probe method: two pressure probes each before, and after, the sample. Plane wave radiation boundary conditions were used for the channel inlet and outlet, with a plane wave generated at, and propagating from, the channel inlet, while the other boundaries were defined as acoustically rigid walls. The mesh and frequency resolutions were kept identical to the earlier simulations. Once the reflection and transmission coefficients were obtained, we estimated the effective density and modulus from the refractive index and the acoustic impedance using Eqns. (2.3) and Eq. (2.4), respectively. The signs of these equations were chosen assuming a passive metamaterial, implying the real part of the impedance $Z$ remains positive. The imaginary

part of $n$ was chosen to be negative,[42] to ensure that the sound speed retains a positive imaginary component.

Figure 2.3 shows the effective density and modulus extracted from three different unit cell arrangements: (a) only Helmholtz resonators, (b) only membranes, and (c) a combination of membranes and Helmholtz resonators. Dashed green lines represent the analytical values while, as before, the negative density and modulus regions are highlighted by colored backgrounds. The single negative modulus or negative density regions are well described. Likewise, the doubly negative region appears, as expected, between $\omega_{0H} < \omega < \omega_{0m}$. However, for the Helmholtz resonator alone, the effective density around $\omega_{0H}$ varies in the FEM results while the simplified analytical model predicts a constant value. This effective density variation has been already observed in Ref. [jena2019demonstration] and is also present in the combined Helmholtz resonator and membrane system (Fig. 2.3(c)). We note that the resonance peaks in Fig. 2.3 have finite widths, which is caused by the retrieval of the effective density and modulus from one unit cell structure. There is also a sharp drop at the edge of the doubly negative regime in Fig. 2.3(c) that corresponds to the transition from negative density alone to doubly negative behavior.

### 2.2.3 Enhanced acoustic transmission

Enhanced acoustic transmission via CAMs was evaluated by simulating the acoustic propagation of ultrasound through a target high impedance layer with, and without, the doubly negative acoustic metamaterial. The magnitude of the high impedance layer's properties were chosen to match those of the metamaterial. For a chosen design frequency of 0.303 MHz, the properties of the target high impedance material are $\rho = 0.16\rho_0$ and $B = 0.225B_0$. The metamaterial unit cell dimensions remain unchanged, and a 10-cell structure is considered. In Fig. 2.4, we show the normalized transmission intensity through the channel: *i*) without the high impedance layer, *ii*) with the high impedance layer, and *iii*) with both the the 10-cell metamaterial and the high impedance layer. For reference, in Fig. 2.4 we also show the transmission for the

combinations of the high impedance layer plus the metamaterial with only membranes, and with only Helmholtz resonators.

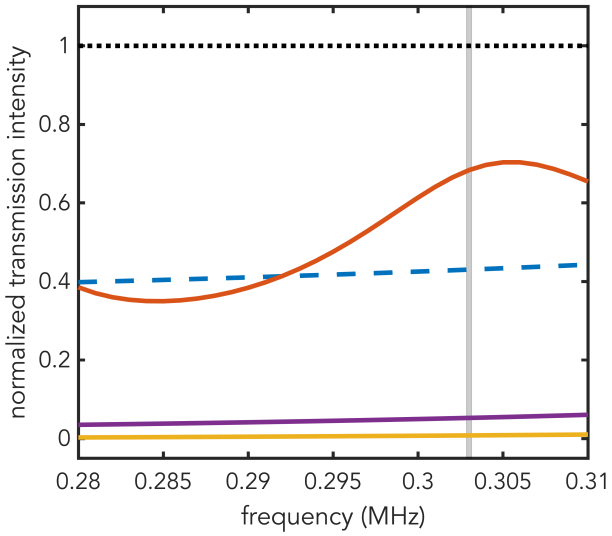


**Figure 2.4**: Normalized transmission intensity through the channel alone (dotted black line), the high impedance layer (dashed blue line), the CAM with the high impedance layer (solid red line), Helmholtz resonator-based metamaterials plus the high impedance layer (solid yellow line), and membrane-based metamaterials plus the high impedance layer (solid purple line). The vertical gray line highlights the chosen frequency of operation: 0.303 MHz.

At the desired frequency of 0.303 MHz, the normalized transmission intensity through the high impedance layer is 43% (blue dashed line). When the CAM is added, the transmission increases to 70% (red solid line), showing the enhanced transmission enabled by the CAM. When the metamaterial is composed of only membranes or only Helmholtz resonators (as a single negative metamaterial), the transmission drops to less than 5%. This low transmission is expected because the investigated frequency range corresponds to forbidden bands of propagation for the single negative metamaterials (*see* Fig. 2.2). We note that our measured transmission enhancement for the negative index plus high impedance layer is less than that of Ref. [41], wherein transmission was increased to 97% of the control case. We speculate that this may be due to acoustic wave scattering induced by the high aspect ratio of our metamaterial resonant elements, particularly the Helmholtz resonator cavity and it's narrow neck.

## 2.3 Proof of concept and feasibility

To evaluate the feasibility of the proposed metamaterials, we present the fabrication and experimental characterization of two types of unit cells: membrane-only, and membrane-plus-Helmholtz resonator. A flow chart showing the individual nanofabrication steps is provided in the supplementary information. In summary, the structures are fabricated on 200 μm thick ⟨100⟩ Si chips. The membrane-only unit cells are fabricated by depositing 660 nm thick silicon nitride ($SiN_x$) films on both sides of the chip by plasma-enhanced chemical vapor deposition (PECVD). The $SiN_x$ on the "back" side is patterned to form windows by UV lithography and dry etching. A deep reactive ion anisotropic dry etch is then performed to remove 180 μm of the Si bulk and form vertical walls. This is followed by anisotropic KOH wet etching, which is used to remove the remaining Si bulk and form the $SiN_x$ membrane. For the membrane-plus-Helmholtz resonator unit cell, 660 nm thick $SiN_x$ is deposited by PECVD on the "front" side only of a blank Si chip (in contrast to both sides in the prior case). The back side is then structured by UV lithography and a Si dry etching process to produce the Helmholtz cavity and neck with respective dimensions of 500×500 μm and 50×20 μm, where both have a depth of 10 μm. A 1 μm thick $SiN_x$ layer is then deposited on the back side to protect the topography of the Helmholtz cavity and neck during the membrane fabrication steps. To fabricate the membrane in the combined membrane-plus-Helmholtz resonator unit cell, windows in the back side $SiN_x$ are defined by UV lithography and dry etching, as in the membrane-only unit cell fabrication procedure. As before, deep reactive ion anisotropic etching and KOH wet etching are then used to remove the Si bulk and form the front $SiN_x$ membrane. Representative scanning electron microscopy images of the fabricated structures are presented in Fig. 2.5(a-b). We note that the Helmholtz resonator is not fully enclosed as a result of the described single-unit-cell fabrication process, and that the final wall of the cavity is formed as a result of clamping together two unit cells.

We prepared membrane-only unit cells with three different types of silicon nitride mem-

**Table 2.1**: The resonance frequencies of three different membranes immersed in water along with their standard deviations ($\sigma$) for the three first modes of vibration from experiment and computation are in good agreement. The resonant frequencies are the average values obtained by measuring four samples for each membrane size.

| Membrane | | Frequency (MHz) | | | |
|---|---|---|---|---|---|
| Size ($\mu$m) | Pre-stress(MPa) | mode (1,1) | | mode (1,2) | |
| | | $f_{exp} \pm \sigma$ | $f_{sim}$ | $f_{exp} \pm \sigma$ | $f_{sim}$ |
| 70×70×0.66 | 400 | $0.68 \pm 0.18$ | 0.43 | $1.32 \pm 0.06$ | 1.32 |
| 82×82×0.20 | 1200 | $0.43 \pm 0.01$ | 0.43 | $1.17 \pm 0.01$ | 1.21 |
| 39×39×0.20 | 1200 | $1.24 \pm 0.05$ | 1.43 | $3.32 \pm 0.04$ | 3.72 |

branes. In addition to the membrane geometry characterized in Figs. 2.2 to 2.5, the remaining two membrane types were designed to have smaller widths and higher pre-stresses in order to test our design's potential for reaching the MHz frequencies characteristic of biomedical ultrasound technologies. For each type of membrane we constructed and measured four nominally identical samples. All of the samples were immersed in water and their resonant frequencies and corresponding vibration modes measured using a scanning Laser Doppler Vibrometer (LDV, UHF-120-SV, Polytec, Waldbrönn, Germany). The membrane is excitchapteed by a single period 2.09 MHz sinusoid wave with a 625 Hz repetition rate generated by a piezoelectric disk that is placed 2 cm from the sample. Each signal was averaged over 10 repetitions, and then a moving average algorithm was applied to smooth the measured signal. Fig. 2.5(c-e) shows the three first membrane mode shapes obtained from both the LDV experimental measurements (left) and from the FEM simulations (right) for the 70×70×0.66 $\mu$m (400 MPa) membranes (which corresponds to the membrane geometry and resonant frequency shown in Figs. 2.2-2.4). The mode shapes show good agreement between the LDV measurements and FEM simulation results. Table 2.1 shows the resonant frequencies, obtained from both experiments and FEM simulations, for the first three modes of all three membrane types, where average values and standard deviations are provided that based upon the differences between the four nominally identical samples of each membrane type. By decreasing the membrane width to 39 $\mu$m and increasing its pre-stress

to 1.2 GPa, we were able to measure a fundamental membrane resonance at 1.24 MHz, which approaches the working frequency range for biomedical ultrasound technologies [76, 81, 82]

We also characterized the acoustic response of the membrane-plus-Helmholtz resonator unit cell. The membrane for the combined unit cell has the same dimensions and stress as the membrane-only unit cell shown in Figs. 2.2-2.5 (specifically, $70\times70\times0.66$ μm and 400 MPa). The Helmholtz resonator was made with cavity dimensions of $500\times500\times10$ μm and neck dimensions of $50\times20\times10$ μm. As previously described, the membrane-plus-Helmholtz resonator unit cell was completed by clamping a membrane-only unit cell to the open side of the Helmholtz resonator cavity to form the fully enclosed unit cell. As shown in the top illustration of Fig. 2.5(f), clamping these two samples together creates a second membrane in this test configuration, which was used to measure the acoustic response of the unit cell via LDV (with $\sim 1$ $\mu$m laser spot diameter). These results were also compared with measurements on a membrane-only unit cell that was clamped together with a wafer of the same thickness and without either a membrane or a Helmholtz resonator, containing only a channel as can be seen in the bottom illustration of Fig. 2.5(f). A Gaussian-modulated sine wave packet was then generated as an acoustic input via a piezoelectric disk (C–213 40 mm diameter, Fuji Ceramics, Ltd., Tokyo, Japan). The central frequency was swept from 0.2 to 0.3 MHz in increments of 0.01 MHz. The results of these measurements are shown in Fig. 2.5(j-l). Corresponding FEM simulations are shown in Fig. 2.5(g-i). The normalized fast Fourier Transform (FFT) intensities are plotted in panels (g, j) for the membrane-only unit cells, and in panels (h, k) for the membrane-plus-Helmholtz resonator unit cells. The key feature to observe is the dip in transmission appearing at 0.267 MHz for the membrane-plus-Helmholtz resonator unit cell spectra, which is not present in the membrane-only unit cell spectra. We therefore attribute this dip to the resonant frequency of the Helmholtz resonator. This feature is also observed in the FEM simulations, but is shifted down to 0.237 MHz, resulting in an error of $\sim$12% between the experimental and numerically predicted resonant frequencies. For further clarity, we also separately plot the spectrum for a 0.24 MHz

center excitation frequency in Figs. 2.5(i) and 2.5(l), wherein the same dip in the (measured and simulated, respectively) spectra can be seen. We suggest that the differences between the experimental and FEM numerical results for the Helmholtz resonator frequency could be due to small deviations of the neck or cavity during fabrication. For instance, if the Helmholtz cavity was just 1 μm deeper than expected, it would result in a change in the resonance frequency of 0.03 MHz, close to the deviation observed between the experimental and numerical results.

In order to utilize negative index metamaterials for biomedical therapy applications, 1–10 MHz resonant frequencies are needed for the membrane and Helmholtz resonators, and a sufficiently large doubly negative bandwidth must be maintained. These operating frequencies can be achieved for the membrane, as seen by our 39 μm wide and 1.2 GPa pre-stress membrane, by reducing the membrane's size and increasing its pre-stress. Furthermore, the Helmholtz resonator is patterned by standard nano-fabrication methods, and its depth, one of the drivers for the resonator's frequency, is determined by the dry etching process. Dry etching is routinely used to etch sub-micron depths, suggesting that 1–10 MHz resonant frequency resonators can be fabricated. Concerning the bandwidth, we note that for our metamaterial design, $\omega_{0m}$ is in between $\omega_{0H}$ and $\omega_{1H}$, such that the difference between $\omega_{0m}$ and $\omega_{0H}$ bounds the bandwidth for our double negative regime. In the case where $\omega_{0m}$ is above $\omega_{1H}$ and $\omega_{0H}$, the difference between $\omega_{1H}$ and $\omega_{0H}$ will govern the bandwidth for the doubly negative regime. A key parameter affecting the frequency of $\omega_{0m}$ and $\omega_{1H}$ is the unit cell period length $D$, wherein the period affects the second Helmholtz resonator resonance ($\omega_{1H}$) via the channel volume and the membrane resonance ($\omega_{0m}$) via the mass of the unit cell. For our design and manufacturing process, the unit cell period is determined by the silicon wafer thickness and we note that thinner wafers (thicknesses less than 10$\mu$m) are readily available from vendors.

To explore the effect of the system dimensions on the behavior of the membrane and Helmholtz resonator, we study via FEM simulation the membrane resonance frequency as a function of the square-shaped membrane lateral dimensions for a membrane thickness of 200 nm,

an initial membrane stress of 1.2 GPa, and two unit cell lengths, 20 and 100 μm, as shown in Fig. 2.6. We observe that the resonant frequency of the membrane increases as its size decreases. The resonance exceeds 10 MHz when the membrane size is less than 10×10 μm for a unit cell period length of 20 μm. For a specific membrane width, the resonance frequency of the membrane is increased when the period length of the unit cell is reduced. In Fig. 2.6(b), we show the $\omega_{0H}/(2\pi)$ and $\omega_{1H}/(2\pi)$ of the Helmholtz resonator as a function of cavity volume for several different neck sizes and unit cell period lengths. Both $\omega_{0H}$ and $\omega_{1H}$ are dependent on the dimensions of the neck and cavity, while the period length only affects $\omega_{1H}$. As expected, $\omega_{0H}/(2\pi)$ grows rapidly with the decrease of the cavity volume, reaching above 1 MHz for a 100×100×10 μm ($1\times10^5$ $\mu m^3$) Helmholtz resonator cavity size for neck dimensions of 50×10×10 μm (see Fig. 2.6(b)). There is also a slight increase of $\omega_{0H}$ with the shrinking neck dimensions. In Fig. 2.6(c), we see the expected increase in $\omega_{0H}$ as the cavity volume decreases. We note that for given neck and cavity dimensions, $\omega_{0H}$ is fixed while $\omega_{1H}$ is tuned by the period of unit cell length, which means as the channel volume decreases, the bandwidth between $\omega_{0H}$ and $\omega_{1H}$ increases.

Leveraging this scaling analysis, we suggest that an experimentally achievable CAM with negative index behavior above 1 MHz could be designed, for example, for a unit cell with a unit cell length of $D$ = 100 μm, a membrane of dimensions 20×20×0.20 μm and pre-stress of 1.2 GPa, and a Helmholtz resonator of cavity and neck sizes of 150×150×10 μm and 20×10×10 μm, respectively. While the nano-fabrication issues appear achievable, we note that the fluid dynamics in such tiny waveguides could also involve different relevant physical phenomena when the dimensions reach sub-micron or nanometer scales. Viscous, Brownian motion, and thermal dissipative effects may become increasingly important and affect the resulting metamaterial properties. These open questions concerning the physics of downscaling will be explored in future work.

## 2.4 Conclusions

In this work, we have designed and explored the acoustic properties of a negative index acoustic metamaterial towards, with eventual aim of achieving enhanced acoustic transmission through a high impedance biological layer at frequencies relevant to biomedical ultrasound technologies. The acoustic metamaterial has been based on a realistic, manufacturable, experimental design. The analytical and numerically calculated dispersion band diagrams for the constitutive building blocks of our metamaterial has been presented along with their effective properties. We also computationally demonstrate, using a 3D geometric model of our metamaterial, the possibility of achieving an enhanced acoustic transmission through a high impedance layer when the metamaterial effective properties are negative and matched to the magnitude of the layer's properties. Finally, preliminary experimental realization of the unit cell structure is presented using conventional silicon based microfabrication, which has the potential for future down scaling. The realized unit cells were tested in the near-MHz regime, and showed promising behavior and good agreement with our predictions. This work provides additional forward progress toward metamaterial-based devices for enhanced acoustic transmission with applications in non-invasive imaging and focused high-power ultrasound.

This Chapter, in part, have been submitted for publication of the material as it may appear in Physical Review Applied, 2020. Jiaying Wang, Florian Allein, Nicholas Boecholer, James Friend, Oscar Vazquez-Mena. "Design of Negative Refractive Index Metamaterials for Near-Megahertz Enhanced Acoustic Transmission in Future Biomedical Ultrasound Applications", Physical Review Applied, Revision and resubmit, 2020. The dissertation author was the primary investigator and author of this paper.

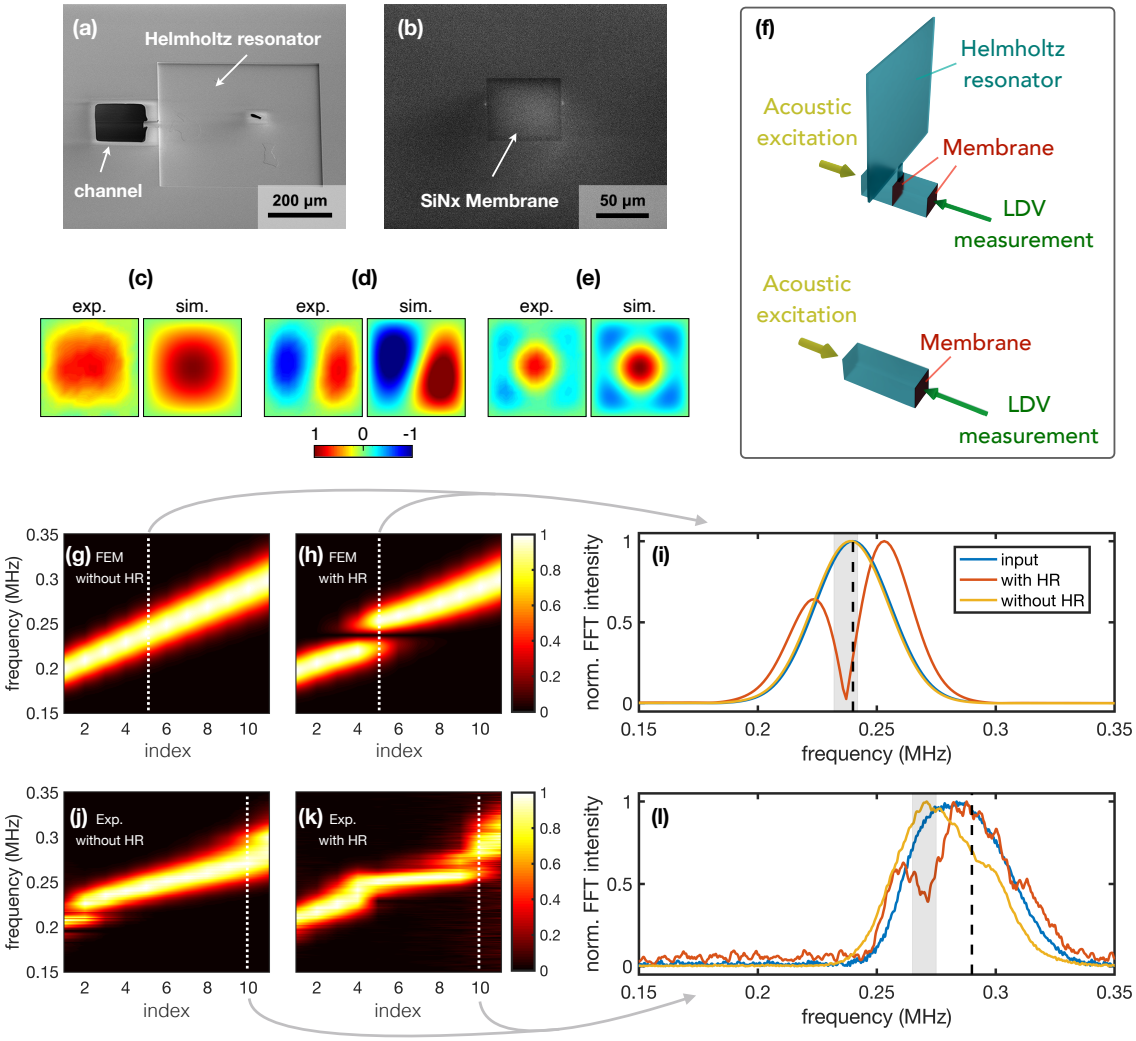


**Figure 2.5**: (a) Front and (b) back side scanning electron microscope images of a sample unit cell (with dimensions of 500×500×10 μm for the cavity, 50×20×10 μm for the neck, 70×70×0.66 μm for the membrane, and 70×70×200 μm for the channel), which shows the Helmholtz resonator on the front and the membrane on the back of the layer. (c-e) Experimental and numerical normalized displacement of the first three membrane resonances where (c) corresponds to the (1,1) mode , (d) to the (1,2) mode, and (e) to the (1,3)+(3,1) mode. (f) Illustration showing the configuration used to obtain the results for panels (g-l) with (Top) and without (Bottom) the Helmholtz resonator. (g-i) FEM and (j-l) experimental characterization of the unit cell. The effect of introducing the Helmholtz resonator (HR) is shown in the FEM-derived normalized FFT plots of frequency with respect to the Gaussian modulated sine wave index in (g, j) without the HR and (h, k) with the HR. (i) Normalized FFT intensity for a central frequency of 0.24 MHz (vertical dashed black line), which corresponds to index 5 (vertical dotted white line from panels (g, h)). (l) Normalized FFT intensity for a central frequency of 0.29 MHz (vertical dashed black line), which corresponds to index 10 (vertical dotted white line from panels [j, k]). The Helmholtz resonance frequencies are highlighted by a gray background at (i) 0.23 MHz and (l) 0.27 MHz.

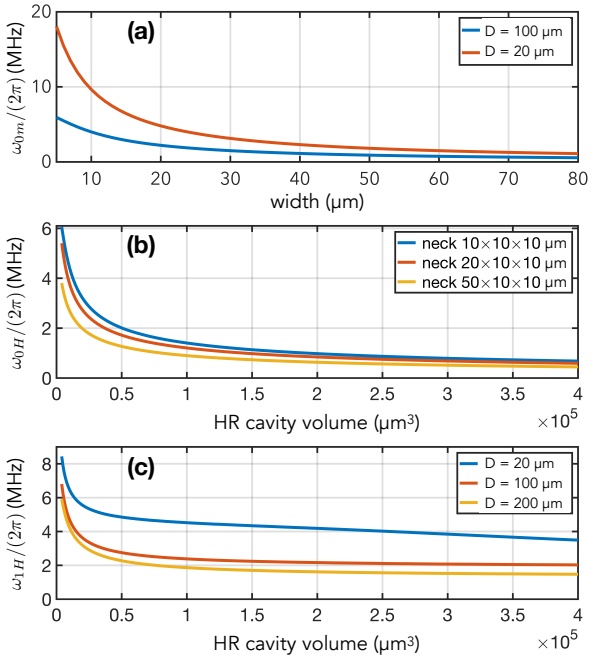


**Figure 2.6**: (a) The membrane resonance frequency, $\omega_{0m}/(2\pi)$, as a function of the square membrane's side length with a constant 200 nm thickness and pre-stress of 1.2 GPa, for two period lengths, $D = 20$ and 100 μm. (b) The resonance frequency, $\omega_{0H}/(2\pi)$, as a function of the Helmholtz resonator cavity volume for different neck dimensions. (c) The resonance frequency, $\omega_{1H}/(2\pi)$, as a function of the Helmholtz resonator cavity volume for different period length $D$ (channel $25\times25\times D$ μm) and neck dimension of $20\times10\times10$ μm.

# Chapter 3

# Frequency and damping effect of suspended silicon nitride membranes in water near the megahertz range

## 3.1 Introduction

Membranes have emerged as crucial components to obtain effective negative density in acoustic metamaterials by inducing opposite phase between pressure and acceleration.[83, 84, 78, 28] Hyperbolic metamaterials with negative effective density built by two-dimensional membrane arrays have enabled super lenses with resolution beyond the diffraction limit at 1 kHz.[85] When membranes enabling negative density are combined with Helmholtz resonators producing negative effective modulus[86], double negative metamaterials (i.e. negative density and negative modulus) can be obtained. [60, 33] These extraordinary materials are predicted to enhance acoustic transmission through high-contrast biological barriers such as the skull,[41] which could enable novel capabilities in biomedical ultrasound such as non-invasive neurostimulation and transcranial brain imaging and therapies. However, the experimental realization of negative

acoustic metamaterials has not reached the operating frequency of medical ultrasound. The implementation of membranes with resonance frequency in the MHz range in water is one of the major challenges which needs to be solved.

Silicon nitride ($SiN_x$) membranes are widely used as mechanical resonators in micro-electromechanical systems (MEMS) and have broad applications such as pressure sensors and transducers, membrane sieves, microresonators, and microfabrication shadow masks[87, 88, 89, 90, 91, 92, 93, 94]. They are remarkably strong against static loads and chemically stable in a wide range of environments. [95] These properties make $SiN_x$ a natural candidate to produce membrane components in acoustic metamaterials operating in high-frequency range. There are several studies on $SiN_x$ membranes used as capacitive ultrasound transducer[96, 97], filters[93], and pressure sensors[98], but there are no specific studies on their resonance behavior in the MHz range fully immersed in water. Solid plates dominated by flexural rigidity immersed in liquid have also been studied[99], but the resonance frequency of membranes with residual tensile stress operating fully immersed in water still near the MHz range remains largely unexplored. The main limitation to achieve MHz resonance frequency is the strong reduction in resonance frequency of mechanical resonators upon immersion.[100, 101, 102] The main factors causing this reduction are the kinetic energy transfer from the membrane to the liquid and the viscous losses. [103, 104] Understanding the resonance frequency reduction of $SiN_x$ membranes and damping phenomena are important for their implementation in acoustic metamaterials for ultrasound imaging applications.

Herein, we study the reduction in resonance frequency and quality factor of $SiN_x$ membranes from air to water. Previous reports have suggested that unit cells in the 100 μm range could operate around 1 MHz in water[85], therefore, we decided to study membranes with widths around 100 μm, fabricating membranes with widths between 40 and 160 μm wide. The membrane vibrations are studied using Laser Doppler Vibrometry (LDV), allowing measuring the resonance frequency and imaging their respective vibration modes. We also use finite element

methods (FEM) to simulate the behavior of the membranes. From the experimental values of resonance frequency and quality factor ($Q$ factor) we extract the water loading added mass, the non-dimensionalzed added virtual mass incremental (NAVMI) factor, the damping ratio and the damping coefficient for different vibrating modes of membranes with different sizes. The estimated NAVMI factor and damping coefficients are crucial parameters that will facilitate the design of $SiN_x$ membranes for negative acoustic metamaterials close to relevant medical ultrasound frequencies.

Understanding the behavior of water-immersed membranes in the megahertz range is critical to develop novel acoustic metamaterials compatible with biomedical ultrasound applications. Herein, we study the influence of water on the resonance frequency and quality factor near the megahertz range of silicon nitride membranes fully immersed in water using Laser Doppler Vibrometry. The resonance frequency of silicon nitride membranes significantly decreases in water compared to air. For a 40 μm wide membrane, the resonance frequency is reduced from 11.2 MHz in air to 1.24 MHz after immersion in water, which is confirmed by finite element method simulations. Our results indicate that the water mass loading plays a major role in the resonance frequency reduction, with a ratio of water mass to membrane mass of $m_{\text{water}}/m_{\text{membrane}} \sim 10^2$ and NAVMI factors of $\Gamma \sim 1.3$. We attribute the main losses to acoustic radiation with small contributions from viscous damping. We estimate that silicon nitride membranes with widths below 50 μm are required to build negative metamaterials operating above 1 MHz. The large NAVMI factors suggest strong coupling between membrane motion and acoustic waves in water, which is important to develop metamaterials able to manipulate acoustic fields.

## 3.2 Experimental Methods

The membranes were designed with square shape and widths of 40, 80, 120 and 160 μm aiming to reach resonance frequencies around 1 MHz in water. Fig. 3.1(a) illustrates the

microfabrication of the suspended $SiN_x$ membranes for this study which is based on conventional KOH etching. Our process starts with a 400 μm-thick, double-sided polished silicon wafer (4-inch (100) silicon wafer, University Wafer Inc., MA, US) with 200 nm-thick $SiN_x$ layers deposited on both sides by low-pressure chemical vapor deposition. Then, a chrome metallic layer is deposited on the top (membrane) side to protect the top $SiN_x$ during wafer processing. Ultraviolet photolithography was then carried out on the back side of the wafer with a positive photoresist (AZ12XT-10PL, Microchemicals, Ulm, Germany), followed by $SiN_x$ dry etching on the backside to define opening windows for KOH etching. Then the photoresist and Cr protective layer are removed. Finally, the topside $SiN_x$ thin film was released by KOH wet anisotropic Si etching (40 wt%, 80, 5 hrs). The wafer is cleaned in a HCl bath for 30 min for potassium decontamination followed by RCA cleaning. Fig. 3.1(b) shows an optical microscope image of four membranes with different membrane widths on the front side of the chip. Due to fabrication process limitations, the final membranes had slight variations from the designed values. For example, the membranes in Fig. 3.1(b) have actual sizes of 39 μm, 82 μm, 118 μm and 157 μm in width. An important aspect from the fabrication are variations in thickness. Figure 3.2 shows the experimental mapping and thickness fitting data from ellipsometry (J.A. Woollam M-2000D Ellipsometer) confirming the thickness of 204 nm with a variation of $\pm$ 2 nm. An SEM cross section in Figure 3.3(a) also shows that the thickness of the SiNx layer is 200 nm.

LDV measurements[105, 106, 107] were performed with a UHF-120SV equipment (Polytec, Waldbronn, Germany) with the measurement setup shown in Fig. 3.1(c). The membranes were excited by a 4 by 4 cm square shape lithium niobate thickness-mode device with an adhesive putty absorber between the lithium niobate and the silicon chip hosting the membrane. The distance between the lithium niobate and the membrane was set at 1 cm to prevent dynamic or near-field coupling between the membrane and transducer, ensuring that any vibration in the membrane is induced via the fluid.[108] The excitation from the water on the Si frame is expected to be negligible in comparison to the water-membrane coupling given the large acoustic

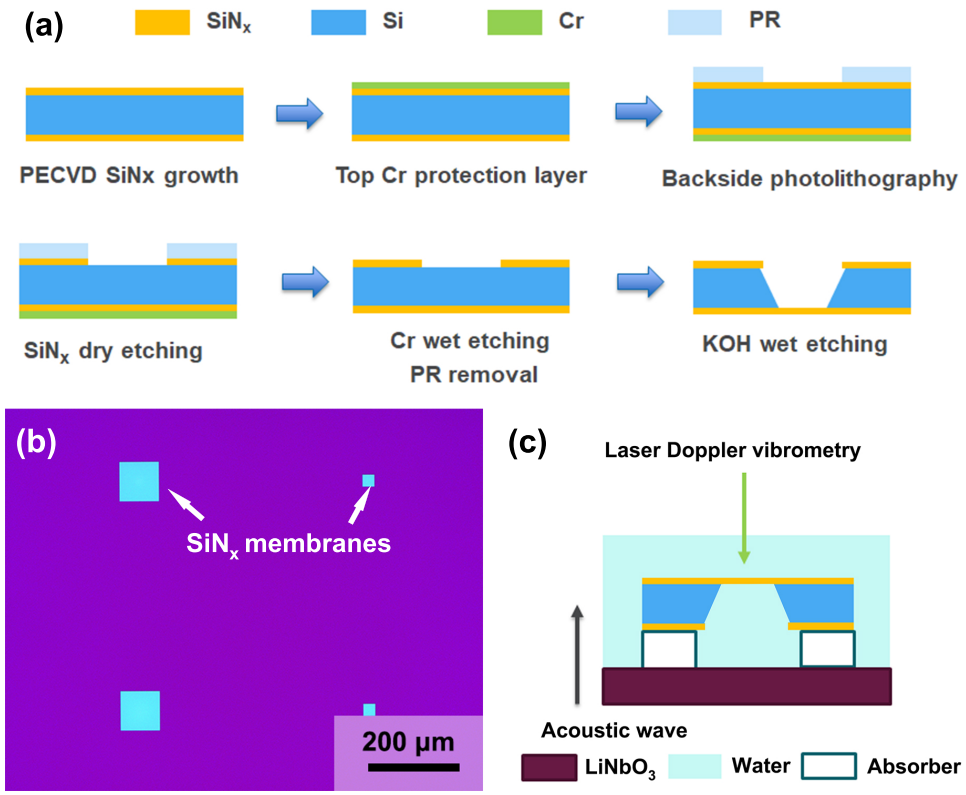


**Figure 3.1**: (a) Process flow for the microfabrication of suspended silicon nitride membranes using photolithography to define etching windows, followed by KOH wet etching of Si for membrane release. (b) Optical image of $SiN_x$ membranes with different membrane widths of 39 µm, 82 µm, 118 µm and 157 µm. (c) LDV experiment setup for resonance frequency measurements.

impedance difference between water and silicon. The membranes were excited with a chirp wave by a vector signal generator (SMBV100A, Rohde Schwarz, Germany) and an amplifier (ZHL–32A+, Mini-Circuits, Brooklyn, NY) before being applied to the face electrodes of the lithium niobate. Frequency sweeps were performed from 9 kHz to 20 MHz in air and from 9 kHz to 4 MHz in water with 625 Hz steps in both cases. The chirp wave period was set to 1.6 ms to match the average time elapsed between each LDV measurement from point to point as it scanned across the membrane. Each displacement measurement was averaged ten times to reduce the potential signal noise. Four samples for each membrane dimension were measured from which the average and standard deviation of the resonance frequency and $Q$ factor were extracted. Size variations were mainly due to the fabrication process. Lorentzian distributions

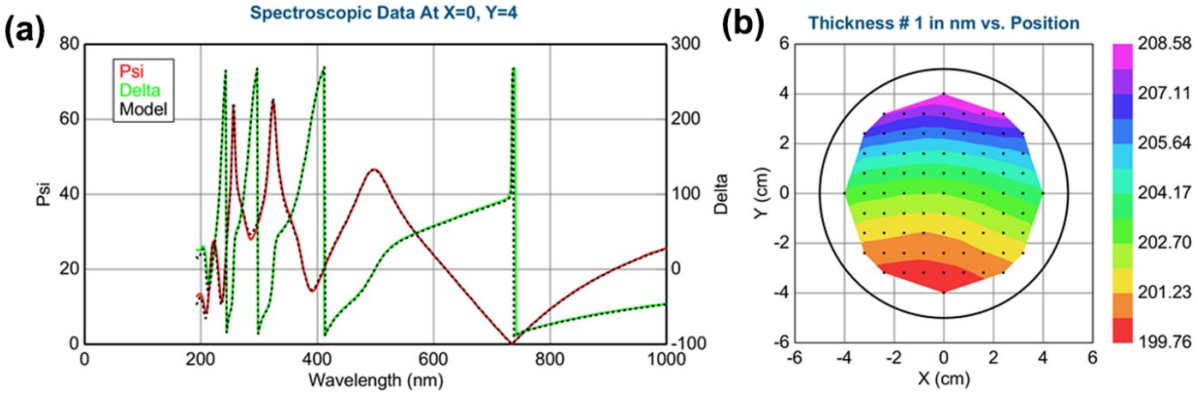


**Figure 3.2**: (a) Delta angle and reflective intensity change of $SiN_x$ membrane characterized by ellopsometry, fitting by $SiN_x$ model; (b) $SiN_x$ membrane thickness distribution on silicon substrate.

curve fitting characteristic of resonance responses of dynamic systems were utilized to extract the peak position and $Q$ factor for each resonance. The experimental $Q$ factor is calculated by $Q_{\text{exp}} = f_{\text{R}}/(f_2 - f_1)$ where $f_1$ and $f_2$ are frequencies at which the amplitude of is $1/\sqrt{2}$ times of the resonance frequency $f_{\text{R}}$. Since our LDV setup produces a laser spot of 3 μm in diameter, we were able to study the (1,1), (1,2), (1,3)+(3,1), (1,4) of the membranes. However, in the particular case of the 39 μm wide membranes, the laser spot was too wide to resolve the (1,3)+(3,1) and (1,4) modes.

Simulations in air were performed using the built-in thermo-acoustics model in COMSOL Multphysics, considering the thermal and viscous damping effect in water. The linearized Navier-Stokes equation was solved with the thermoviscous boundary layer condition. The thickness of the thermo-viscous boundary layer is set as $\delta_v = 0.57(\mu\text{m})\frac{1(\text{MHz})}{f}$ where $f$ is working frequency[109]. The velocity of sound in water is 1480 m/s and bulk viscosity is $2.47\times10^{-3}$ Pa·s.[110] The resonance frequency and quality factor can be obtained by eigenfrequency simulation. For each multimode vibration shape, the resonance frequency is calculated by FEM resulting in a complex number frequency ($f_{\text{R}} = f_{\text{real}} + if_{\text{imag}}$). The real part ($f_{\text{real}}$) represents the resonance frequency and the imaginary part ($f_{\text{imag}}$) shows the dissipation. Thus, the $Q$ factor at resonance can be obtained from $Q = f_{\text{real}}/(2f_{\text{imag}})$.

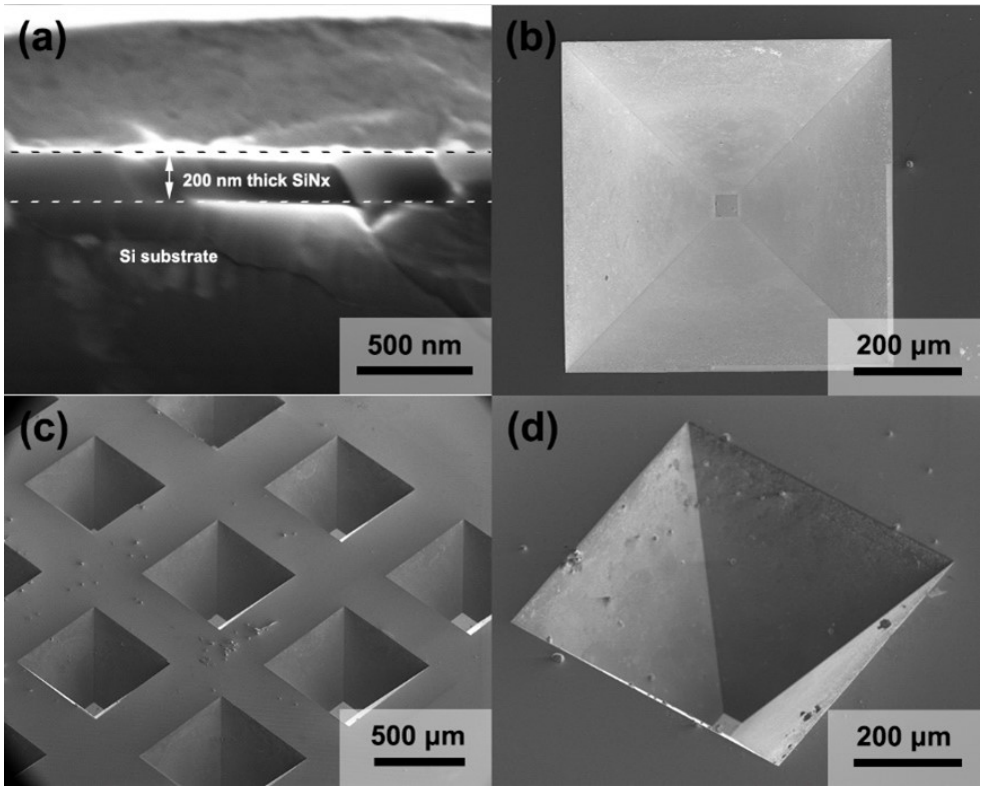


**Figure 3.3**: SEM image of $SiN_x$ thin film morphology: (a) Cross-section of $SiN_x$ thin film. (b) Topview from backside of silicon substrate; (c) 40 tilted angle from backside of substrate; (d) High magnification of 39 um suspended membrane from backside of substrate.

## 3.3 Results and Discussion

### 3.3.1 $SiN_x$ membrane vibration behavior in air

The LDV characterization of an 82 µm wide $SiN_x$ membrane is shown in Fig. 3.4, showing the resonance frequency and $Q$ factor in air and water. Fig. 3.4(a-c) show the normalized displacements and mode shapes of the membrane in air with Lorentzian fittings for the resonance peaks. The resonance frequencies in air for (1,1), (1,2) and (1,3)+(3,1) modes are $f_{1,1}^{\text{air}} = 5.38$ MHz, $f_{1,2}^{\text{air}} = 8.49$ MHz and $f_{1,3}^{\text{air}} = 12.3$ MHz. The mode (1,3)+(3,1) is actually a superposition of the natural (1,3) and (3,1) modes. Fig. 3.4(d-f) show the results for the same membrane, 82 µm wide, immersed in water. The drastic decrease in resonance frequency from air to water is evident. The (1,1) mode frequency is reduced by $\sim$10x from $f_{1,1}^{\text{air}} = 5.38$ in air to $f_{1,1}^{\text{water}} = 0.44$ MHz in

water(Table 3.1 and 3.2). Similarly, the resonance frequency for the higher modes are reduced from 8.49 to 1.17 MHz for the (1,2) mode, and from 12.3 to 1.87 MHz for the (1,3)+(3,1) mode. The $Q$ factor is also reduced after water immersion. For the (1,1) mode, $Q$ reduces from 138.1 to 5.31, illustrating the strong damping forces affecting the motion of the membrane in water.

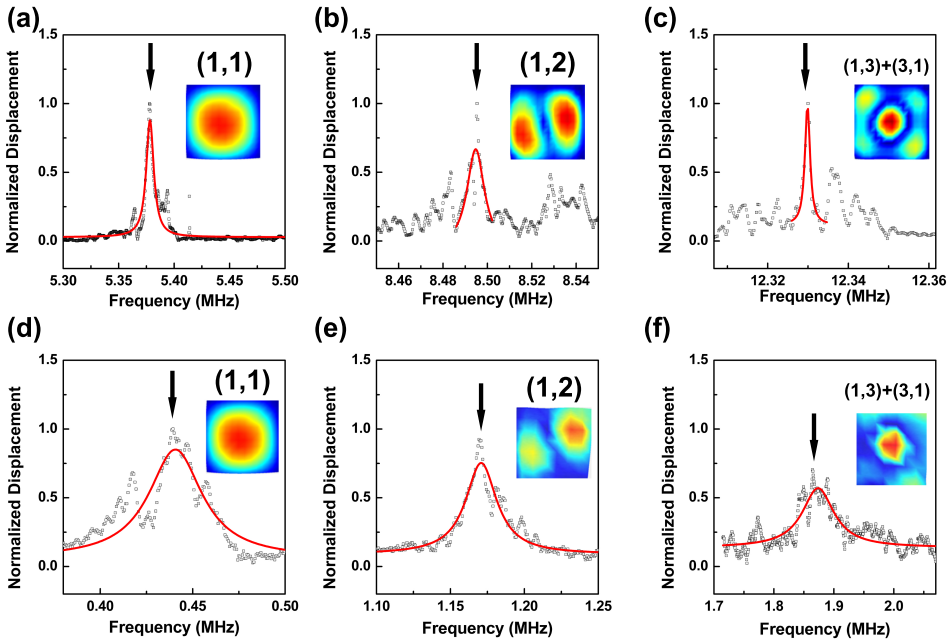


**Figure 3.4**: $SiN_x$ membrane characterization: (a)-(c) Measured resonance frequency and mode shapes by LDV of an 82 μm-square $SiN_x$ membrane in air. (d)-(f) Measured resonance frequency and mode shapes by LDV of the same membrane in water. Red solid lines correspond to Lorentzian fittings.

We compared experimental LDV measurements with analytical calculations and FEM simulations. Fig. 3.5(a) shows the resonance frequency as function of membrane width for the (1,1) mode, exhibiting good agreement between experimental measurements in air by LDV (red squares), FEM simulation in air (red line), and analytic theoretical values (black dotted line). The theoretic resonance frequency values of membranes are extracted by the following equation: [111]

$$f_{i,j}^{\text{air}} = \{\frac{\lambda_{i,j}^4}{4\pi^2 a^4}\left[\frac{Eh^2}{12\rho(1-\nu^2)}\right] + \frac{N(J_i+J_j)}{4\rho h a^2}\}^{1/2} \tag{3.1}$$

where $a$ is the membrane width, and $h = 200$ nm is the thickness; $\rho = 3170$ kg/m$^3$ and $\nu = 0.23$ are the density and Poisson's ratio of silicon nitride; $f_{i,j}^{\text{air}}$ is the natural frequency for $i,j$ mode where $i$ and $j$ refer to the numbers of half-wavelengths present in the mode shape along the $x$ and $y$ axes; $N$ is the linear tensile load; $J_i$ is a constant that depends on the mode number and boundary condition ($J_1$ =1.248 for clamped membranes); $\lambda_{i,j}$ are geometrical parameters for the $i$ and $j$ modes.[111] The experimental and theoretical values for higher resonance modes are shown in the Figure 3.6 and listed in Table 3.1. The resonance values at different mode shapes show also a good agreement between experiments, simulations, and analytical result. The overall frequency mismatch between experimental and simulation results is less than 5%. A critical parameter that determines the membrane vibration behavior is its tensile stress. This value is calibrated by matching the calculations for resonance frequency from Eq. 3.1 with LDV measurements for various resonance modes. The calibrated value obtained from the (1,1) mode is 1.2 GPa. The results from higher modes (1,2) and (1,3)+(3,1) also confirm the stress of membrane of 1.2 GPa.

**Table 3.1**: Resonant frequency of different dimension of high-stress $SiN_x$ membrane in air calculated by Eqn. 3.1. Unit: MHz

| Width(μm) | (1,1) | (1,2) | (1,3) | (2,3) | (1,4) |
|---|---|---|---|---|---|
| 39 | 11.2 ± 0.25 (11.1) | 18.0 ± 0.10 (17.6) | | | |
| 82 | 5.50 ± 0.18 (5.37) | 8.84 ± 0.16 (8.48) | 12.3 ± 0.0 (12.0) | 16.4 ± 0.22 (15.6) | |
| 118 | 3.65 ± 0.02 (3.71) | 5.83 ± 0.07 (5.86) | 8.03 ± 0.43 (8.29) | 9.48 ± 0.01 (9.5) | 10.64 ± 0.24 (10.8) |
| 157 | 2.59 ±0.26 (2.79) | 4.37 ±0.21 (4.41) | 6.09 ±0.11 (6.25) | 7.09 ±0.10 (7.12) | 8.06 ±0.06 (8.15) |

### 3.3.2 $SiN_x$ membrane vibration behavior in water

Fig. 3.5 (a) clearly shows the drastic reduction of resonance frequency in water. For the (1,1) mode and for widths from 160 to 40 μm, the membranes in air (red line/squares) reach

a frequency range of $\sim 2.59 - 11.2$ MHz, but after immersion in water, the range decreases to $\sim 0.18 - 1.24$ MHz (blue line/squares). Fig. 3.5(b) shows the ratio of frequencies in air to water ($f_{1,1}^{\text{air}}/f_{1,1}^{\text{water}}$) as function of width for the (1,1) mode. For 40 μm, the ratio $f_{1,1}^{\text{air}}/f_{1,1}^{\text{water}}$ is ∼9, while for 160 μm it reaches ∼14. This reduction in resonance frequency after water immersion is observed for higher resonance modes. Fig. 3.5(c) shows $f_{i,j}^{\text{air}}$ and $f_{i,j}^{\text{water}}$ for the higher resonance modes for a 118 μm wide membrane and Fig. 3.5(d) shows the corresponding $f_{i,j}^{\text{air}}/f_{i,j}^{\text{water}}$ ratios. The natural mode (1,1) shows the largest reduction with $f_{1,1}^{\text{air}}/f_{1,1}^{\text{water}}$ ∼15, while the higher (1,4) mode shows a smaller reduction with $f_{1,4}^{\text{air}}/f_{1,4}^{\text{water}}$ ∼6. The $Q$ factor also shows a strong reduction for different widths and modes. For the (1,1) mode, the $Q$ factor drops to $Q_{\text{water}} < 10$ for the all the membranes from 40 to 160 μm as shown in Fig. 3.5(e). In particular, the largest drop occurs for the smallest 40 μm membrane , dropping from $Q_{\text{air}} = 694$ to $Q_{\text{water}} = 5.6$. The $Q$ factor for different modes of the 120 μm membranes is shown in Fig. 3.5(f) as well.

**Table 3.2**: Resonant frequency of different dimension of high-stress $SiN_x$ membrane in water. Unit: MHz

| Width(μm) | (1,1) | (1,2) | (1,3)+(3,1) | (1,4) | (3,3) |
|---|---|---|---|---|---|
| 39 | 1.24 ± 0.05 (1.43) | 3.32 ± 0.04 (3.72) | | | |
| 82 | 0.43 ± 0.01 (0.43) | 1.17 ± 0.01 (1.21) | 1.89 ± 0.06 (2.06) | | |
| 118 | 0.25 ± 0.12 (0.24) | 0.64 ± 0.01 (0.69) | 1.07 ± 0.01 (1.19) | 1.69 ± 0.01 (1.81) | 1.82 ± 0.03 (1.95) |
| 157 | 0.18 ±0.05 (0.15) | 0.42 ±0.01 (0.45) | 0.69 ±0.02 (0.77) | 1.10 ±0.01 (1.21) | 1.19 ±0.01 (1.27) |

**Table 3.3**: Quality factor of different dimension of high-stress $SiN_x$ membrane in water

| Width(μm) | (1,1) | (1,2) | (1,3)+(3,1) | (1,4) | (3,3) |
|---|---|---|---|---|---|
| 39 | 5.65 ± 0.56 (4.815) | 22.4 ± 4.9 (29.3) | | | |
| 82 | 5.31 ± 1.03 (3.04) | 21.1 ± 4.18 (24.7) | 17.6 ± 8.9 (20.5) | | |
| 118 | 4.48 ± 0.46 (2.17) | 21.22 ± 3.25 (20.0) | 19.3 ± 6.2 (19.4) | 44.2 ± 5.29 (38.3) | 44.8 ± 3.04 (39.4) |
| 157 | 7.10 ±1.80 (2.55) | 22.0 ±3.21 (22.2) | 20.4 ±2.48 (19.9) | 37.8 ±4.43 (34.1) | 28.1 ±3.7 (37.5) |

### 3.3.3 Water loading effect and NAVMI factor of micrometer-scale $SiN_x$ membrane

To analyze the reduction in frequency, we first look at the contribution from water loading that causes a transfer of kinetic energy from the membrane to the liquid. From the resonance frequency in water and mass, the added mass for mechanical resonators in liquid can be estimated from the expressions:[112]

$$\frac{f_{\text{water}}}{f_{\text{air}}} = \sqrt{\frac{m_{\text{membrane}}}{m_{\text{membrane}} + m_{\text{water}}}} \tag{3.2}$$

$$\frac{m_{\text{water}}}{m_{\text{membrane}}} = (\frac{f_{\text{air}}}{f_{\text{water}}})^2 - 1 \tag{3.3}$$

The ratio of the water added mass ($m_{\text{water}}$) over the membrane mass ($m_{\text{membrane}}$) as function of membrane width for different modes is plotted in Fig. 3.7(a). It increases as the width (a) increases, starting at $m_{\text{water}}/m_{\text{membrane}}$ = 80 for a = 40 μm up to $m_{\text{water}}/m_{\text{membrane}}$ = 212 for a = 120 μm, followed by slight decrease to 206 for a = 160 μm. The large ratios of $m_{\text{water}}/m_{\text{membrane}}$ indicate that the restoring elastic force of the membrane is also transferred to a water body much larger in mass than the membrane itself. For the higher (1,2) and (1,3)+(3,1) modes, the $m_{\text{water}}/m_{\text{membrane}}$ ratio decreases to a range from 25 to 100, with a closely linear increment as function of membrane width. The added mass can be quantified by the nondimensionalized added

virtual mass incremental, or NAVMI, factor reflecting the ratio of kinetic energy of the water to the kinetic energy of the solid membrane [100]. The shift in resonance frequency and the NAVMI factor ($\Gamma$) are related by:[100]

$$\frac{f_{i,j}^{\text{water}}}{f_{i,j}^{\text{air}}} = 1/\sqrt{1+\Gamma_{i,j}\beta} \tag{3.4}$$

$$\Gamma_{i,j} = \left[\left(\frac{f_{i,j}^{\text{air}}}{f_{i,j}^{\text{water}}}\right)^2 - 1\right]\frac{1}{\beta}, \tag{3.5}$$

where $\beta = d\rho_w a/\rho h$ is a thickness correction factor and $\rho_w$ is the water density. The NAVMI factor can be understood as a ratio between the membrane width $a$ and the thickness of the water layer following the membrane motion $l_w$. The NAVMI factor is plotted in Fig. 3.7(b) as function of membrane width for different modes. As expected from the added mass values in Figure 3.7(a), the NAVMI values for the (1,1) mode are higher than for (1,2) and (1,3)+(3,1) modes. For the (1,1) mode, based on the NAVMI factor range of $\Gamma \sim 1.3-0.8$, it can be estimated that the water layer following the membrane motion is close to the actual width of the membrane. However, it should be stressed that the membrane is not in a symmetric environment. One side of the membrane faces the Si chip cavity with size ~a, while the other side has an infinite opened geometry, therefore, the layers of water following the membrane can be different on the two sides. As the membrane is reduced, the Si cavity is also reduced and this may affect the NAVMI factor of smaller membranes. In the case of the higher (1,2) and (1,3)+(3,1) modes, the NAVMI factor is smaller and shows a behavior independent of size. For a given membrane width, the NAVMI factor clearly decreases for higher resonance modes as shown in Fig. 3.7(b). This is expected as the propagation in water of acoustic waves following higher membrane modes is more difficult compared with (1,1) mode that can easily couple to pressure acoustic waves. Previous reports on clamped circular plates (motion driven by flexural rigidity) in infinite open geometries have reported NAVMI values of $\Gamma = 0.35$ for natural (1,1) mode and lower values of $\Gamma < 0.3$ for higher

order modes. [99] In our case, our natural (1,1) mode for squared clamped membranes gives a higher NAVMI factor, indicating a stronger coupling with water motion. The higher values in our case can be due to the cavity geometry on one side of the membranes, which may extend the water motion coupled to the membrane as compared with an infinite open geometry. Another reason for the larger NAVMI factor maybe that for our thin membranes, the restoring force is driven by residual stress that is thickness independent, whereas plates are driven by flexural rigidity that require thicker dimensions to achieve same restoring forces. Therefore, the ratio of water mass to membrane mass is expected to be higher than for plates.

The main damping mechanisms in water are acoustic radiation and viscous losses. The Reynolds number for our membranes can be expressed as: [113]

$$R_e = \frac{\rho_f \omega_{\text{water}} a^2}{4\mu}. \tag{3.6}$$

where $\rho_f$ is the fluid density, $\omega_{\text{water}}$ is the angular frequency in water, and $\mu$ is the bulk viscosity. For the (1,1) mode ($\omega_{\text{water}} \sim 2\pi \times 10^6$ rad/s), we obtain $R_e = 3327$ for the 39 μm membrane and $R_e = 7826$ for the 157 μm membrane. These large Reynolds numbers suggest an low viscous fluid regime in which the main damping factor is the energy lost through acoustic radiation, which as mentioned earlier, seems probable due to the large NAVMI factor and added mass values. The damping ratio $\zeta = 1/(2Q)$ is shown in Fig. 3.7(c) as function of membrane width for different resonance modes. The damping ratio $\zeta$ is the highest for the (1,1) mode, reaching $\zeta \sim 0.1$. The (1,2) and (1,3)+(3,1) modes have smaller damping ratios of $\zeta = 0.01 - 0.03$. The damping behavior of these modes requires further studies since their motion is influenced by the super-position of the (1,2) and (2,1), and (1,3) and (3,1) modes, respectively. Understanding the contribution of each natural mode to the superposition is required to understand the damping of the membranes at their particular modes.The damping coefficients, which is crucial for the operation of the membranes as acoustic metamaterial components can be expressed by the

following equation:

$$\gamma = \frac{m_{\text{membrane}} + m_{\text{water}}}{Q} \omega_{\text{water}} \tag{3.7}$$

are shown in Fig. 3.7(d), showing a decrease as membrane width decreases. This is encouraging for acoustic metamaterials targeting operation above 1 MHz. Based on Fig. 3.7(d), it is possible that membranes below 40 μm can reach higher frequencies without suffering strong overdamping, allowing effective interactions between membranes and acoustic waves.

## 3.4 Conclusions

This work reports the significant reduction in resonance frequency when membranes with widths a=40−160 μm are immersed in water, reaching a ∼10x reduction factor. Based on our measurements, to achieve resonance frequency in water >1 MHz, $SiN_x$ membranes with widths below 50 μm are likely required. The strong reduction in frequency is associated with a heavy water loading effect, reaching mass ratios of $m_{\text{wat}}/m_{\text{mem}} \sim 10^2$. The NAVMI factor reaches values close to $\Gamma \sim 1$ for the first (1,1) mode, indicating that the water layer $l_w$ following the membrane motion is close in magnitude to the membrane width, i.e. $l_w \sim$a. Lower NAVMI values in the 0.2-0.4 range are obtained for higher modes. Based on the estimated Reynolds number, $R_e >$3000, for the membranes studied, we infer that the main losses are due to acoustic radiation with limited effect from water viscosity. This is supported by the large NAVMI value for the (1,1) mode. This is a positive aspect for membranes as acoustic metamaterials components, suggesting a good coupling between membrane motion and acoustic waves. The damping coefficients for the (1,1) mode for 40 μm membranes is $\sim 10^{-4}$, with higher values as the membrane width increases. These may indicate that smaller membranes with higher resonance frequencies above 1 MHz will not be severely affected by damping effects. The presented NAVMI factor and damping coefficients can serve as guidelines to design membranes for negative acoustic metamaterials

operating in the MHz range for medical ultrasound applications. Further studies are required to analyse the coupling between the membrane vibration and acoustic radiation. An effective energy transfer from the membrane motion towards acoustic radiation would favor the manipulation of acoustic fields through negative metamaterials based on membranes.

This Chapter, in full, is a reprint of the materials as it appears in Journal of Micromechanics and Microengineering 2020. Jiaying Wang, Jiyang Mei, James Friend, Oscar Vazquez-Mena."Frequency and damping effect of suspended silicon nitride membranes in water near the megahertz range", Journal of Micromechanics and Microengineering, 2020. The dissertation author was the primary investigator and author of this paper.

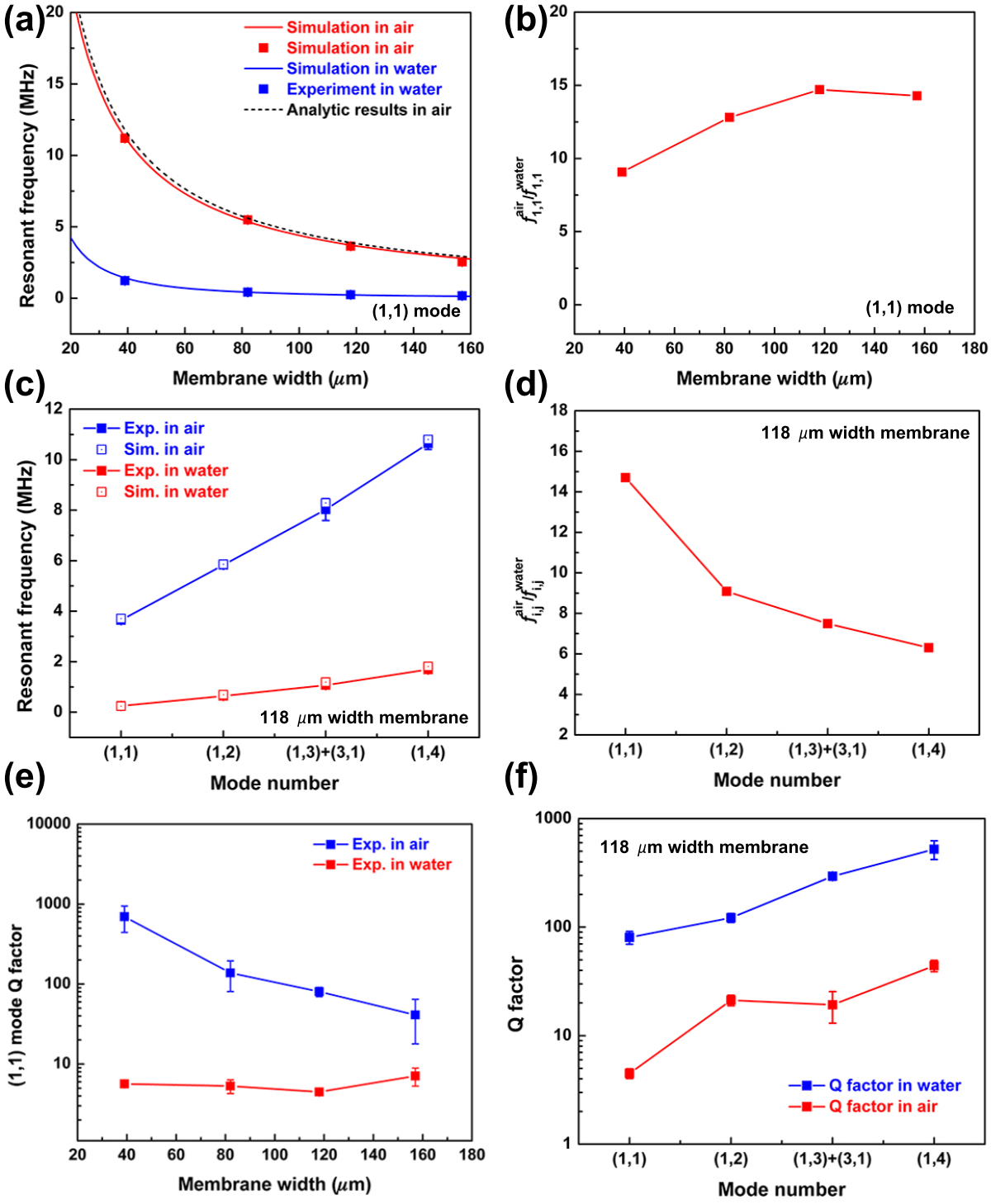


**Figure 3.5**: (a) Resonance frequency as function of membrane width in air and water from LDV measurement, FEM simulations and analytical calculations. (b) Ratio of resonance frequency in air to water $f_{1,1}^{\text{air}}/f_{1,1}^{\text{water}}$ as function of membrane width for (1,1) mode. (c) Resonance frequency for different vibration modes for a membrane 118 μm wide in air and in water. (d) Ratio of resonance frequency in air to water $f_{i,j}^{\text{air}}/f_{i,j}^{\text{water}}$ for different membrane modes of a 118 μm wide membrane. (e) $Q$ factor in air and in water as function of membrane width in air and water for (1,1) mode. (f) $Q$ factor for different vibration modes for a membrane 118 μm wide in air and water.

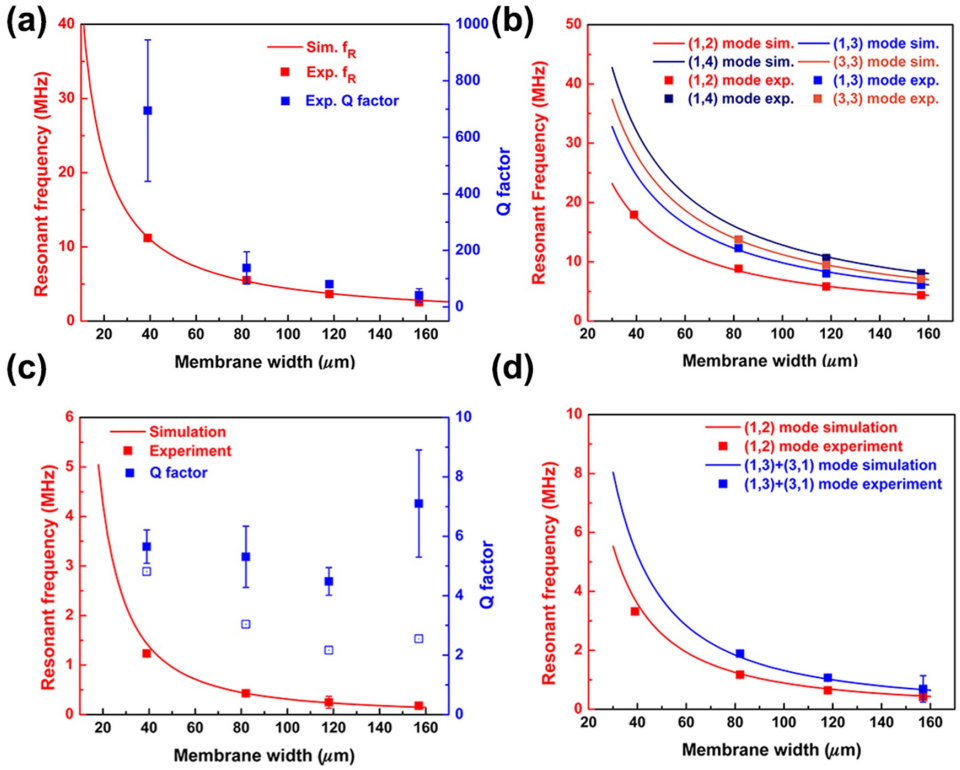


**Figure 3.6**: (a) Resonance frequency and Q factor in air as a function of membrane width. b) Resonance frequency in air for (1,2), (1,3), (1,4) and (3,3) modes. (c) Resonance frequency and Q factor in water as a function of membrane width for (1,1) mode. d) Resonance frequency in water for (1,2) and (1,3) modes.

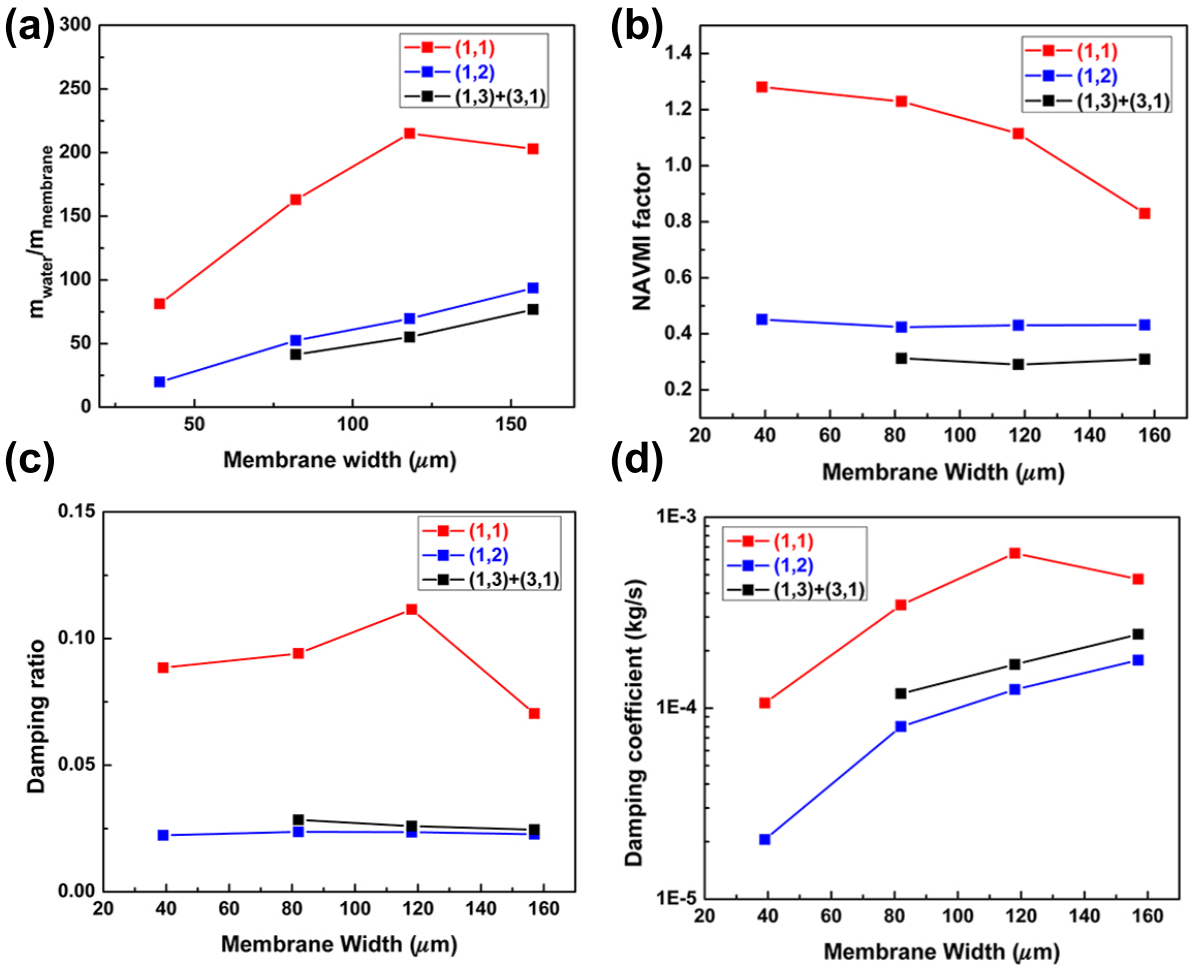


**Figure 3.7**: (a) Ratio of added water mass to membrane mass $m_{\text{wat}}/m_{\text{air}}$ as function of membrane width for various vibration modes; (b) NAVMI factor as function of width for different vibration modes; (c) Damping ratio as function of membrane width for different vibration modes; (d) Damping coefficient as function of membrane width for different vibration modes.

# Chapter 4

# Integration of nanomaterials into three-dimensional vertical architectures

## 4.1 Introduction

Micro/Nanotechnology devices are typically confined to a substrate surface because micro and nanofabrication technologies are mainly based on surface patterning techniques. However, paraphrasing Richard Feynman, there is also plenty of room on top of a substrate to add more structures that would enable more capabilities and functionalities. Three-dimensional (3D) designs would extend storage, computing and sensing capabilities, with novel designs and more interconnections between components. New 3D architectures would also enable far more complex metamaterials with smaller unit cells for higher frequency operation. The advantages of building 3D devices have been shown recently. Samsung has developed a vertical 3D flash memory (VNAND) consisting of 32 stacked layers of memory islands with improved speed and storage capability.[114, 115] Similarly, Shulaker et al, recently reported a 3D integrated circuit containing silicon and carbon nanotube components for computing and memory capabilities fabricated on interconnected vertical layers.[116] The incorporation of nanomaterials into 3D

architectures[117, 118, 119] is another important challenge. 3D patterning techniques like 3D printing[120, 121, 122] and two-photon lithography[123, 124] have achieved great advances in 3D nanofabrication, but they are mainly limited to polymers.[125, 126] Herein, we present a novel fabrication strategy to realize 3D architectures based on horizontal suspended thin films, like graphene and silicon nitride ($SiN_x$), that can integrate microstructures and nanomaterials. This strategy can be complemented with other surface and 3D patterning techniques to create more complex 3D structures with nanomaterial integration.

This method allowing to expand device fabrication in the vertical direction and integrating functional nanomaterials is presented by emulating civil engineering. The architecture uses SU-8 pillars as structural columns which supports multiple horizontal suspended thin films. The films then serves as platforms for the integration of nanomaterials and nano devices. Multiple graphene layers suspended across SU-8 pillars with precise control on their vertical spacing are demonstrated. In addition to graphene, silicon nitride films that offer high strength yield and thickness control are also presented. Metallic microstructures, plasmonic nanostructures, semiconducting quantum dots and monolayer graphene on the suspended films are achieved to prove the capability to integrate functional nanomaterials. This work provides the potential to integrate highly-compact micro/nanoscale devices at different vertical levels with high surface density which allows for more capabilities and functionalities in a single device.

## 4.2 Experimental methods

The 3D architecture proposed is shown schematically in Figure 4.1(a), consisting of thin layers suspended on SU-8 photoresist pillars[127]. To fabricate such structures, we have developed an innovative "3D Layered UV Lithography" fabrication process on a stack of thin films and photoresist layers. This process allows us fabricating multiple suspended layers of multilayer graphene (ML-Gr) and $SiN_x$ supported on SU-8 pillars. Compared with 3D

graphene matrix assembled by graphene nanosheets[128, 129, 130, 131], this architectures with suspended graphene allows for the integration of different functionalities distributed vertically at each thin film. We demonstrate that these layers can host microscale structures and functional nanostructures such as metallic nanodots, semiconducting quantum dots, and monolayer graphene (Figure 4.1.(b)). The spacing between the layers can be controlled and adapted to different applications. In this work, we present spacings from 5 $\mu$m to 50 $\mu$m suitable for microfluidic applications. This innovative process can be adapted to a broad range of materials. The realization of these structures is based on an innovative "3D Layered UV Lithography" process based on the transmission of UV through ML-Gr and $SiN_x$ layers. The process is illustrated in Figure 4.1(c), showing the general strategy for obtaining multiple suspended ML-Gr or $SiN_x$ layers. Both materials are grown on copper foils, ML-Gr is grown by Chemical Vapor Deposition and $SiN_x$ by Plasma-enhanced Chemical Vapor Deposition. Optical/AFM images and Raman spectrum of ML-Gr are provided in Figure 4.2. To fabricate ML-Gr suspended structures, the first step is to spin coat SU-8 on the ML-Gr/Cu foil. Then, the Cu foil is etched in ammonium persulfate solution, leaving a ML-Gr/SU-8 film floating on an aqueous solution. After rinsing in successive DI water baths, the ML-Gr/SU-8 film is transferred to a final substrate (similar to PMMA based graphene wet transfer). As a final substrate we used a Si wafer with 300 nm thick $SiO_2$ with an SU-8 layer deposited by spin coating. This transfer step is repeated several times, adding each time a new ML-Gr/SU-8 film on top of the previous one, forming a stack of alternating ML-Gr and SU-8 layers. Then, we do UV lithography to define SU-8 pillars by exposing the entire stack through the ML-Gr layers. The relevant lithography parameters such as the dose and baking time should be adjusted due to absorption and light scattering of the intercalated ML-Gr. After exposure and post-exposure bake, the critical development step through the thin films is carried on. As expected, this process is much slower, carried out overnight, and finished by using critical point drying to avoid collapsing of the structures. The detailed process flow and parameters are shown in the Table.

## 4.3 Results and discussion

### 4.3.1 3D integration of multilayer graphene

The schematics of suspended ML-Gr layers are shown in Figure 4.5(a1). Figures 4.5(a2-a4) show optical and electron microscope (SEM) images of a ML-Gr layer suspended 2 m above the substrate. The optical image shows the transition from ML-Gr collapsed areas without SU-8 pillars, to the areas with suspended graphene on SU-8 pillars. The color and the interference patterns due to the air wedge between the suspended graphene and the substrate show this transition. One of the most important aspects of these structures are the wrinkles of graphene observed in the SEM images. These wrinkles are a clear indication of its suspended condition and the stress induced during the process. The stress and wrinkles also show limits regarding the flatness and robustness of the ML-Gr layers. Compared with previous reports on free-standing graphene adhered on prefabricated pillars by bare van der Waals interactions[132, 133, 134], our suspended layers are clamped by top and bottom SU-8 layers, providing a stronger clamping and a non-sliding fixed boundary condition. Since the structures are released by supercritical drying that reduces the effects of surface tension, we suppose that the stress in the multilayer graphene is induced by SU-8 geometry. The stress in multilayer graphene remains clearly around the SU-8 pillars, causing the formation of wrinkles. Further process optimization is required to reduce the wrinkles and residual graphene stress.

Using this procedure, the maximum ML-Gr span (distance between SU-8 pillars) reached is 20 $\mu$m with 40 $\mu$m-diameter SU-8 pillars distributed in a hexagonal array. The smallest span is 5 $\mu$m with SU-8 pillars 2 $\mu$m in diameter in Figure 4.3 and 4.4. The maximum span also depends on the geometry and arrangement of the pillars, since this influences the stress distribution of the ML-Gr layers. Figures 4.5(b2-b3) show intensity maps of G and 2D Raman peaks of graphene in Figure 4.5(b1). The $20 \times 20 \mu m^2$ Raman mappings show a uniform and low-defect graphene area around SU-8 pillars. The Raman spectrum of the graphene signature peak in Figure 4.5(b4) also

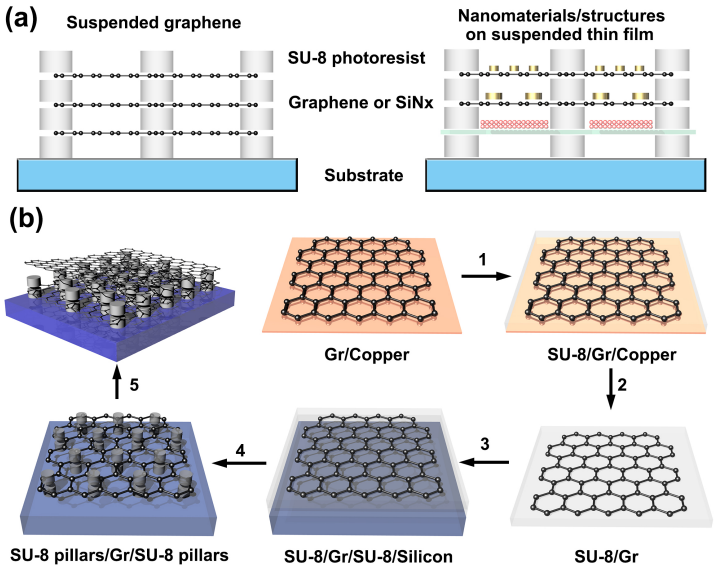


**Figure 4.1**: (a) Fundamental geometry consisting of thin films (ML-Gr or $SiN_x$) suspended and supported by SU-8 pillars. (b) Functional materials and structures can be incorporated on each of the suspended structures to create 3D devices. (c) Fabrication process: ML-Gr (or $SiN_x$) is grown on a copper foil by CVD (PECVD for $SiN_x$). Then, SU-8 is coated on the ML-Gr/Cu foil substrate by spin-coating (Step 1). The Cu foil is etched in a wet solution (Step 2), followed by wet transfer of the ML-Gr/SU-8 film to a final substrate (Step 3). This step is repeated several times, adding multiple ML-Gr/SU-8 layers on the final substrate, producing a stack of multiple ML-Gr and SU-8 layers. Finally, UV lithography (Step 4) is used to expose the entire stack due to the low ML-Gr absorption of UV light, allowing SU-8 exposure through the entire stack. Finally, the structure is developed through the ML-Gr layers. The same process can be applied to $SiN_x$ layers.

indicates multilayer graphene exists both in the suspended areas (red cross) and inside the SU-8 pillars (blue cross). The results for multiple ML-Gr suspended layers are presented in Figure 4.5(c1-c4). Figures 4.5(c1-c2) show SEM images of two suspended graphene layers from a top view and from a cross-section by cleavage. In order to study the graphene distribution in the vertical direction, non-invasive three-dimensional Raman tomography was used to map Raman signal at different depths (Figure 4.5(c3))22. Two separated 2D Raman signals from ML-Gr (2690 $cm^{-1}$) over Si signature signal (520 $cm^{-1}$) confirms the spacing between suspended graphene layers. Figure 4.5(c4) shows three suspended ML-Gr layers. Similar to single suspended layers, the multiple case also shows stress, defects and ripples. The wrinkles and defects of graphene

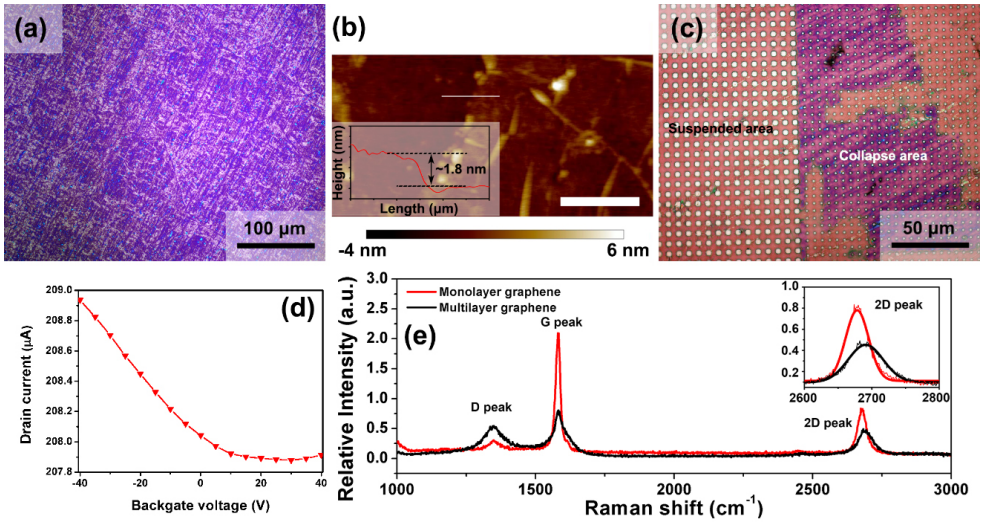


**Figure 4.2**: (a) Optical microscopy images of multilayer graphene; (b) AFM images at the edge of multilayer graphene; inset: height profile (c) optical images of multilayer graphene on 500 nm-thick pre-patterned SU-8 pillar; (d) Electrical properties of multilayer graphene; (e) Raman spectra of monolayer and multilayer graphene. Inset: Raman spectra from 2600 cm-1 to 2800 cm-1.

indicate that further work is required to improve the robustness and flatness of ML-Gr. Regarding the lithography process, it is easy remarkable that the SU-8 pillars do not have straight walls as expected for a regular process. This is probably due to less UV light reaching the bottom SU-8 layers due to the presence of the graphene layers. Since ML-Gr has a finite UV absorption, the exposure dose should be increased with respect to a conventional SU-8 process without ML-Gr. Compared with same-thickness SU-8 layer, we increase the exposure dose by 30 mJ/cm2 for each ML-Gr layer to ensure that the bottom SU-8 layers are sufficiently exposed. Optical inspection of structures during the developing process is also necessary to monitor and make sure all the SU-8 has been developed. Therefore, optimizing dose and development parameters is required. It is important mentioning that the spacing between each of the graphene layers can be controlled by the thickness of the SU-8 layer. Our future work includes avoiding or decreasing the defects on the supported graphene layer, and to explore limits in span and distance between ML-Gr layers.

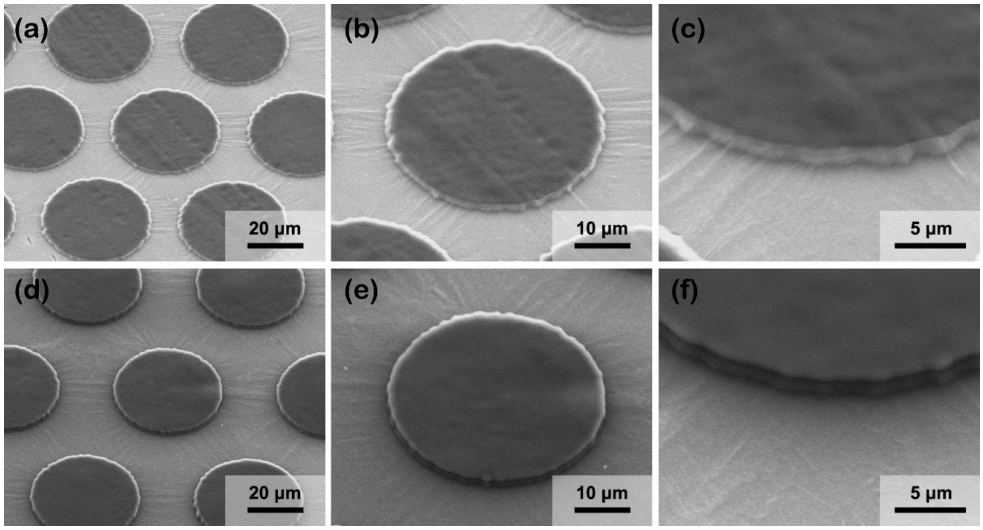


**Figure 4.3**: SEM images of SU-8/graphene/SU-8 three-dimensional architectures, top SU-8 2002 (Thickness: ∼2 µm); Bottom SU-8 2005 (Thickness: ∼2 µm): (a),(b) and (c) Diameter: 40 µm and spacing: 10 µm; (d),(e) and (f) Diameter: 40 µm and spacing: 20 µm;

### 4.3.2 3D integration of dielectric layers

This fabrication process can also be applied to other materials, as long as they transmit sufficient UV light. Using this method, we realized $SiN_x$ suspended layers shown schematically in Figure 4.6(a1). $SiN_x$ offers several advantages as supporting layer, namely chemical stability, tunable thickness and stress, and high yield strength. $SiN_x$ layers of 300 nm thickness grown by PECVD on Cu foils were used. A cross section showing one $SiN_x$ layer suspended ∼5 $\mu$m from the substrate is shown in Figure 4.6(a2), with a close look at the membrane and its clamping site into the SU-8 pillar in Figure 4.6(a3). The $SiN_x$ layer is clearly much more robust and flatter than graphene. Its roughness is attributed to the Cu growth substrate. Similar to ML Graphene, the top SU-8 layers are wider than the bottom layers, also due probably to UV light absorption from $SiN_x$. We demonstrate that this technology can be used to realize vertically stacked microcavities, as shown in Figure 4.6(a1). Figure 4.6(b1) shows a top view of 200 $\mu$m wide stacked cavities connected by 50 $\mu$m wide microchannels. The height of the cavities is defined by the thickness of the SU-8 layers. Figures 4.6(b2-b3) show a FIB cut into the membranes, showing the underneath membranes with a spacing of 5 $\mu$m and without SU-8 in between. This device has four cavities

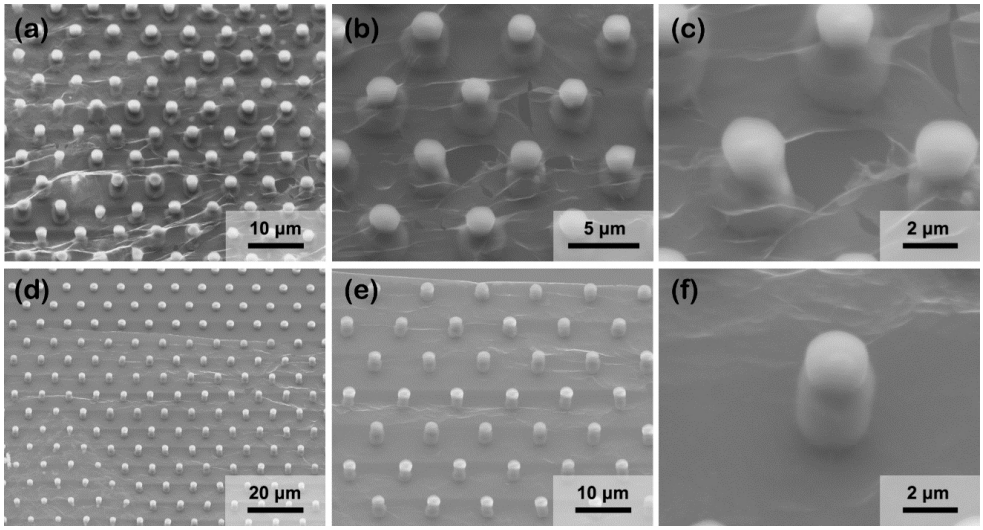


**Figure 4.4**: SEM images of SU-8/graphene/SU-8 three-dimensional architectures top SU-8 2002 (Thickness: ∼2 µm); Bottom SU-8 2002 (Thickness: ∼2 µm): (a),(b) and (c)!Diameter: 2 µm and spacing: 2 µm; (d),(e) and (f) Diameter: 2 µm and spacing: 5 µm;

formed by four $SiN_x$ membranes. Figure 4.6(c1-c2) shows similar cavities with 50 $\mu$m spacing, with a view of the top membrane and a cross-section side view of the cavities. Figure 4.6(c3) shows a 45 degree tilted close-up view of the $SiN_x$ membranes showing the clamping site. The damage of the membranes is due to the cleaving to obtain the cross-section. These structures are promising for 3D microfluidic devices and networks.

The realization of ML-GR and $SiN_x$ suspended structures demonstrates the effectiveness of our 3D Layered UV lithography method to fabricate stacks of suspended structures. However, this also requires a careful tuning of exposure parameters and development process. Concerning the exposure parameters, the presence of ML-Gr and $SiN_x$ layers affect the UV transmission through the stack and therefore the exposure time and the sidewall profile. Experimentally, we have demonstrated up to 4 layers of $SiN_x$ membrane. Based on 70 percentage transmission through 200 nm $SiN_x$, the maximum number of layers that can transmit sufficient UV light for SU-8 cross-linking would be about 5 layers (25 percentage transmission)[135]. In the case of ML-Gr, we have reached up to 3 layers and theoretical maximum number of ML-Gr is 8 layers considering 83% UV transmission of ML-Gr.[136] As an alternative path to overcome this issue,

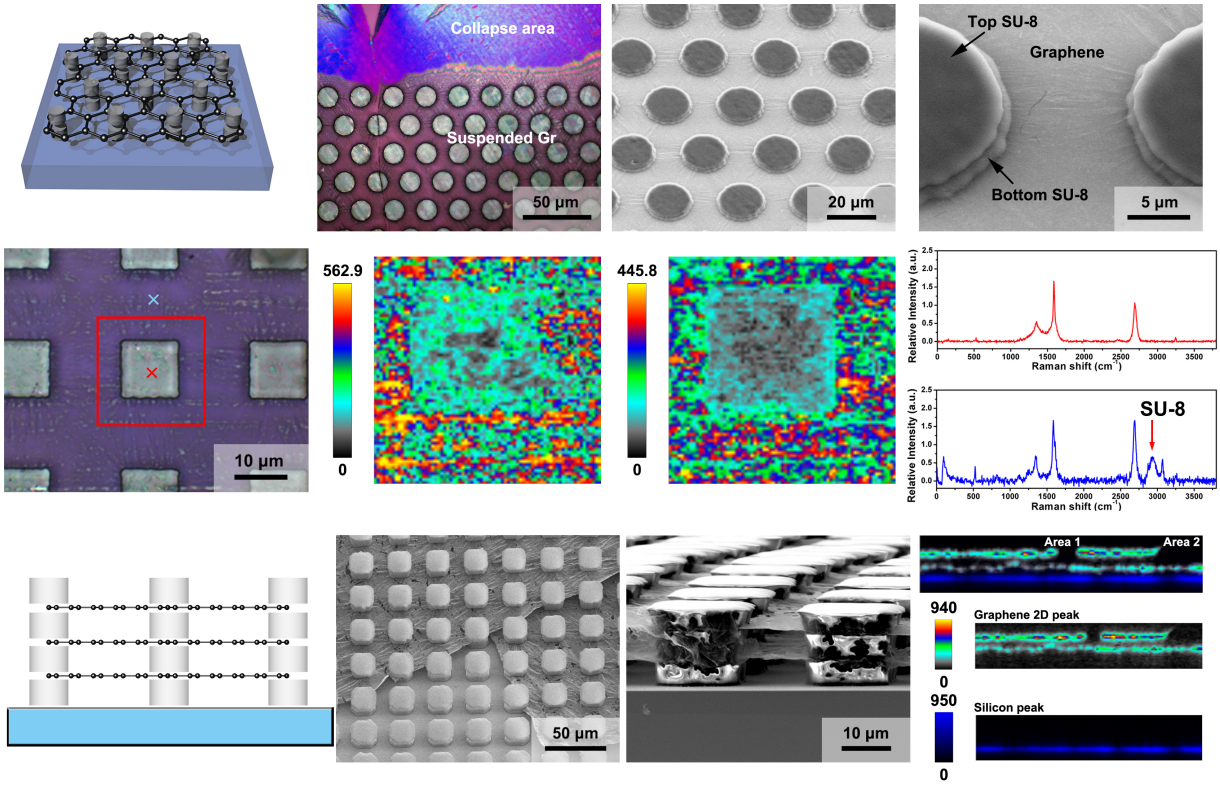


**Figure 4.5**: (a1) Schematics of ML-Gr suspended structures. (a2-a4) Optical picture and SEM images of a single suspended ML-Gr layer clamped by SU-8 pillars. The optical picture shows the transition from collapsed to suspended areas. The SEM images show wrinkles in ML-Gr due to stress induced during the process. (b1-b4) Raman analysis of the suspended ML-Gr, showing intensity maps of G and 2D graphene peaks. The Raman spectra in (b4) are taken at crosses in (b1). The spectrum in the pillar also shows a characteristic SU-8 peak. (c1-c3) SEM and crosssection Raman spectrum of two ML-Gr suspended on SU-8 pillars with 5 µm interspacing, showing also stress in the layers. (c4) Side view of three ML-Gr layers suspended across SU-8 pillars.

multiple exposures can be carried out as more SU-8 and thin films are added, with the requirement of a good alignment for each exposure. There are also design limitations, especially for the span of the membranes and the aspect ratio of the SU-8 pillars.

### 4.3.3 Integrate functional materials on suspended layers

Finally, we also show that functional materials can be integrated into these suspended layers, schematically shown in Figure 4.6(a1). These structures are deposited on the ML-Gr on

copper (before SU-8 spin coating) by UV lithography, evaporation, and lift-off. Figures 4.6(a2-a4) show metallic microstructures two ML-Gr suspended layers with different designs. Since the ML-Gr transfer is done in liquid without an alignment stage, the positioning and orientation of the metallic structures are not controlled. An alignment stage would enable specific alignment of the structures. We also demonstrate the integration of nanostructures on a $SiN_x$ suspended film. Figures 4.6(b1-b2) show Au nanostructures added by e-beam lithography, evaporation and lift-off, after the layers are released. This process enables the proper alignment and positioning of the nanostructures and shows that the suspended layers can sustain a lithographic processing. The plasmon resonance of these nanostructures in Figure 4.6(b4) is similar with respect to same reference structures deposited on $SiO_2$.[137] However, this strategy only allows patterning on the top of membrane. Larger arrays of nanostructures can be produced with more cost-effective techniques and added on the $SiN_x$ before transferring, as done for the microstructures in Figures 4.6(a2-a4). This would ensure a large area coverage of nanostructures. Besides deposition, nanostructures like nanoholes produced by FIB milling can be integrated as well (Figure 4.6(b3)), which can be utilized for biosensing.[138, 139, 140] The suspended $SiN_x$ membrane with nanostructures also can be used as the shadow mask for stencil lithography to fabricate the metallic nanostructures underneath[141]. We also show the addition of CdSe QD on suspended $SiN_x$ (Figure 4.6(c1-c3)). The QDs keep their photoluminescence properties as measured from the emission spectrum[142] (Figure 4.6(c4)). Finally, we added monolayer graphene on suspended $SiN_x$ membranes that can enable electrical devices (Figures 4.6(d1-d3)). The graphene layer shows a resistance of 1.3 k$\Omega$ extracted from the electrical measurements in Figure 4.6(d4). These results demonstrate different strategies to integrate functional nanomaterials into these 3D architectures, with the potential to enable nanomaterial-based 3D devices.

## 4.4 Conclusion

In conclusion, we have shown 3D architectures based on suspended films that can serve as platforms for devices and nanomaterials. This architecture can enable new devices with expanded space, storage, and function capability exploiting the vertical direction, rather than conventional lateral addition of components. This architecture can bring a new generation of microfluidic devices with larger surface density, a new fabrication strategy for metamaterials, and a new path to integrate different nanomaterials in a single device. Other functional materials such as biomolecules and other 2D materials can also be integrated, however, further work is required to exploit the full potential of this architecture. The integration of nanomaterials from the stacking step is required to integrate them at any membrane level with their own design and functionality. The alignment of the structures at different layers is also required for full 3D design enabling specific capabilities and performance. Another critical requirement is Vertical Interconnection Access (VIAs), allowing the electrical/physical connectivity between different levels. The 3D Layered UV lithography can also be implemented for different materials and reach nanoscale dimensions. SU-8 could be replaced by other materials and other exposure methods such as X-ray or e-beam, as long as the radiation can go through the stack. Other possibilities are combining this strategy with other techniques like tilted/rotated lithography[127] or two-photon lithography[123, 124] to obtain more complicated structures. The fabrication strategy and the architecture presented herein therefore, establishes, a first step towards a new platform for 3D multi-material architectures.

This Chapter, in full, is a reprint of the materials as it appears in ACS applied materials interfaces 2018. Jiaying Wang, Stefan Wagner, Wenjun Chen, Yuesong Shi, Abdoulaye Ndao, Leon Li, Boubacar Kante, Donald Sirbuly, Max C Lemme, Oscar Vazquez-Mena. “Integration of Nanomaterials into Three-Dimensional Vertical Architectures”, ACS applied materials interfaces, 10(34) 28262-28268, 2018. The dissertation author was the primary investigator and author of

this paper.

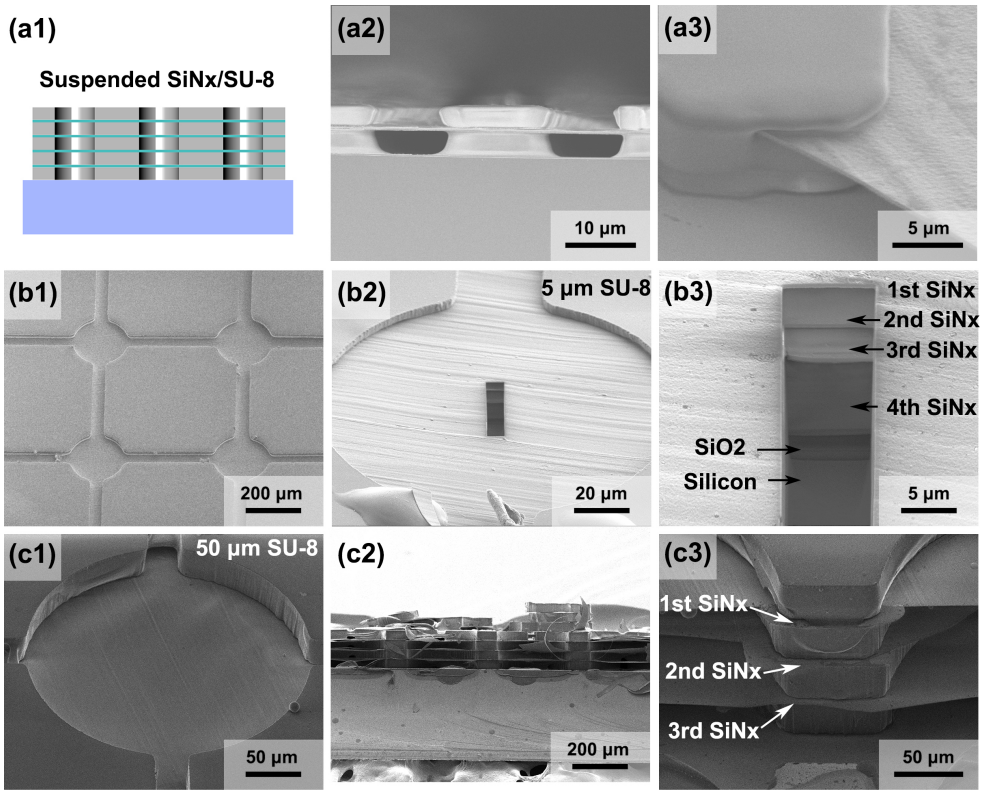


**Figure 4.6**: (a1) Schematic of cavities formed $SiN_x$ suspended layers supported on SU-8 microstructures; (a2) Side view of a single $SiN_x$ membrane suspended on SU-8 pillars; (a3) Close-up showing the $SiN_x$ membrane at its clamping site on a SU-8 pullar; (b1) Top view of $SiN_x$/SU-8 cavities 200 µm wide connected by 50 µm wide channels; The height of the cavities is determined by the thickness of the SU-8 layers (5 µm); (b2-b3) Focused Ion Beam (FIB) cut through showing four $SiN_x$ membranes enclosing 4 cavities, and the effective development of the SU-8 layers through the stack; (c1) Top view of cavities with 50 µm thick SU-8. (c2-c3) Chip cleavage allows side and tilted view of the caviteis and of the clamping of the $SiN_x$ films on the SU-8 layers. Comparing with ML-Gr devices in Fig. 4.5, $SiN_x$ layers are clearly more stable with fewer wrinkles and defects.

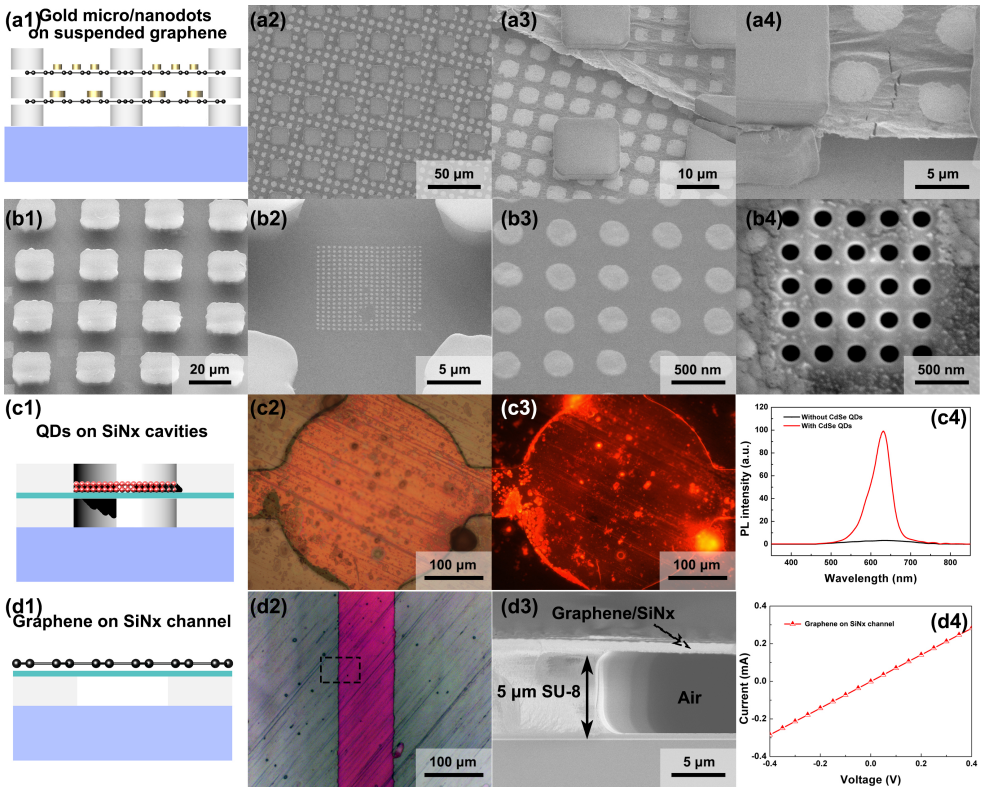


**Figure 4.7**: (a1) Schematic of suspended layers integrating functional structures. (a2-a4) Metallic microstructures with different patterns on two suspended ML-Gr layers; (b1-b2) Metallic nanodots on suspended $SiN_x$ layer defined by e-beam lithography and metal evaporation; (b3) Nanoholes in $SiN_x$ milled by FIB; (b4) Normalized reflection of Au nanodots array using Fourier-transform infrared spectroscopy in Fig.4.7(b2); (c1-c4) Schematics, optical image fluorescence image and photoluminescence of CdS quantum dots on a suspended $SiN_x$ membrane; (d1-d4) Schematic, optical image, SEM-cross-section and I/V curve of monolayer graphen on a $SiN_x$ suspended layer

# Chapter 5

# Future Work

## 5.1 Conclusions

The objective of this research is to design and fabricate the double-negative metamaterial component in near-megahertz range which is expected to enhance the ultrasonic transmission through the biological layer. We choose the Helmholtz resonator as the negative modulus component and pre-stress $SiN_x$ membrane as the negative density component.

We have successfully designed and fabricated the Helmholtz-resonator and membrane-based metamaterials which is expected to work between 200 to 410 kHz frequency range. The dispersion relation, transmission and effective parameters are extracted by COMSOL simulation, which shows a good agreement with analytic results. Meanwhile, the metamaterial unit cell is prepared by standard microfabrication process and characterized by LDV. The realized unit cells were tested in the near-MHz regime, and showed promising behavior and good agreement with our predictions. This work provides additional forward progress toward metamaterial-based devices for enhanced acoustic transmission with applications in non-invasive imaging and focused high-power ultrasound.

We demonstrated there is a significant reduction when the membranes immersed in water.

This reduction is related to the water loading effect. The resonant frequency and Q factor are characterized and the (1,1) NAVMI factor is calculated for the resonant frequency estimation when the membrane works in the water. The damping coefficient of 40 μm membrane at (1,1) mode is $\sim 10^{-4}$, which has higher value with the membrane width increases. The NAVMI factor and damping coefficients can serve as guideline for the negative density behavior design for metamaterials for biomedical application.

We also developed a novel three-dimensional fabrication method which allows to integrate layer materials such as graphene or dielectric thin film in vertical direction. By integrating different functional components in three-dimension, which open a new path for 3D multi-materials architectures. By reducing the $SiN_x$ membrane distance spacing from 200 μm to 2 μm, this technique can also be expanded to improve the performance of acoustic metamaterials up to 10 MHz range.

## 5.2 Future Work

As mentioned in chapter 2, there is a long way to go to apply this metamaterials on biomedical imaging application. Based on the scaling rule and the FEM results in Section 2.3, the periodic length of metamaterials needs to reach under 100 μm, which acquires more challenging in fabrication and measurement technique. Our three-dimensional fabrication methods may solve this problem by decreasing the distance between silicon nitride membranes to 2 μm, but the pre-stress of silicon nitride membrane is unknown.

Meanwhile, the scattering and dissipation effect in the passive metamaterials cannot be ignored in ultrasonic frequency range. When the total thickness of metamaterials is close to the acoustic wavelength, the application of passive metamaterials are hindered by the interior losses in high-frequency range. The acoustic energy may partially dissipated inside and limit the overall efficiency. Compared with the passive metamaterials, active acoustic metamaterials provide more

freedoms to manipulate the acoustic wave for dynamically reconfigurable and loss-compensating metamterials. The effective material properties, namely the effective density and modulus can be tuned in the real time. Meanwhile, the active components in the system can balance the loss-gain condition to provide a unusual acoustic response.

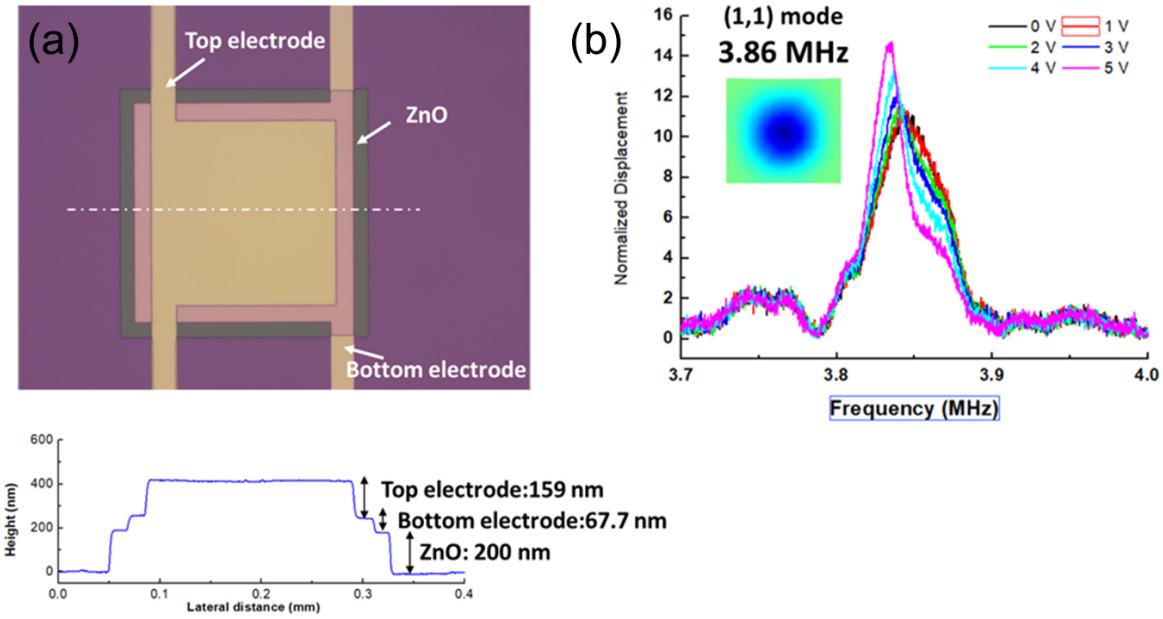


**Figure 5.1**: Prototype of active metamaterials: (a) Optical and height profile of active metamterials (b) Tunable resonance frequency by applying DC bias

Inspired by the previous research, zinc oxide (ZnO) piezoelectric layer are added on the passive silicon nitride membrane to design the active metamaterials. 0 to 5 V DC bias is applied on top and bottom gold electrodes in order to tune the resonant frequency of silicon nitride. The optical images of ZnO-based active metamaterials component and the height profile is demonstrated in Fig. 5.1(a). The thickness of $SiN_x$ is 600 nm and the thickness of ZnO is 200 nm. The vibration mode of active silicon nitride membrane is characterized by LDV and the (1,1) mode is 3.86 $\pm$ 0.02 MHz. By applying the DC bias on ZnO, there is a slightly resonant frequency shift from 3.85 MHz to 3.83 MHz, which is as expected in Fig. 5.1(b). The resonant frequency of this active membrane in water is 1.28 MHz, which is expected to compensate the lossy in the biological layer and tune the effective parameters of double-negative metamaterials in

megaherz range. We believe this technique will expand the horizons in invisible acoustic sensor and unidirectional metasurface.

# Bibliography


[1] Alexander Poddubny, Ivan Iorsh, Pavel Belov, and Yuri Kivshar. Hyperbolic metamaterials. *Nature photonics*, 7(12):948–957, 2013.

[2] Katia Bertoldi, Vincenzo Vitelli, Johan Christensen, and Martin Van Hecke. Flexible mechanical metamaterials. *Nature Reviews Materials*, 2(11):1–11, 2017.

[3] Saman Jahani and Zubin Jacob. All-dielectric metamaterials. *Nature nanotechnology*, 11(1):23–36, 2016.

[4] Guancong Ma and Ping Sheng. Acoustic metamaterials: From local resonances to broad horizons. *Science advances*, 2(2):e1501595, 2016.

[5] Zhengyou Liu, Xixiang Zhang, Yiwei Mao, YY Zhu, Zhiyu Yang, Che Ting Chan, and Ping Sheng. Locally resonant sonic materials. *science*, 289(5485):1734–1736, 2000.

[6] Jensen Li and Che Ting Chan. Double-negative acoustic metamaterial. *Physical Review E*, 70(5):055602, 2004.

[7] John Brian Pendry. Negative refraction makes a perfect lens. *Physical review letters*, 85(18):3966, 2000.

[8] J. B. Pendry. Controlling Electromagnetic Fields. *Science*, 312(5781):1780–1782, 2006.

[9] Ta-Jen Yen, WJ Padilla, Nicholas Fang, DC Vier, DR Smith, JB Pendry, DN Basov, and Xiang Zhang. Terahertz magnetic response from artificial materials. *Science*, 303(5663):1494–1496, 2004.

[10] Ping Sheng, XX Zhang, Zhengyou Liu, and Che Ting Chan. Locally resonant sonic materials. *Physica B: Condensed Matter*, 338(1-4):201–205, 2003.

[11] Guancong Ma, Min Yang, Songwen Xiao, Zhiyu Yang, and Ping Sheng. Acoustic metasurface with hybrid resonances. *Nature materials*, 13(9):873–878, 2014.

[12] Huanyang Chen and Che Ting Chan. Acoustic cloaking and transformation acoustics. *Journal of Physics D: Applied Physics*, 43(11):113001, 2010.

[13] Huanyang Chen and CT Chan. Acoustic cloaking in three dimensions using acoustic metamaterials. *Applied physics letters*, 91(18):183518, 2007.

[14] Shi-Wang Fan, Sheng-Dong Zhao, Liyun Cao, Yifan Zhu, A-Li Chen, Yan-Feng Wang, Krupali Donda, Yue-Sheng Wang, and Badreddine Assouar. Reconfigurable curved metasurface for acoustic cloaking and illusion. *Physical Review B*, 101(2):024104, 2020.

[15] Xianchen Xu, Pei Li, Xiaoming Zhou, and Gengkai Hu. Experimental study on acoustic subwavelength imaging based on zero-mass metamaterials. *EPL (Europhysics Letters)*, 109(2):28001, 2015.

[16] Jie Zhu, Johan Christensen, Jesper Jung, Luis Martin-Moreno, X Yin, Lee Fok, Xiang Zhang, and FJ Garcia-Vidal. A holey-structured metamaterial for acoustic deep-subwavelength imaging. *Nature physics*, 7(1):52–55, 2011.

[17] Ying Cheng, Chen Zhou, Qi Wei, DaJian Wu, and XiaoJun Liu. Acoustic subwavelength imaging of subsurface objects with acoustic resonant metalens. *Applied Physics Letters*, 103(22):224104, 2013.

[18] Bogdan-Ioan Popa and Steven A Cummer. Non-reciprocal and highly nonlinear active acoustic metamaterials. *Nature communications*, 5(1):1–5, 2014.

[19] AS Gliozzi, M Miniaci, AO Krushynska, B Morvan, M Scalerandi, NM Pugno, and F Bosia. Proof of concept of a frequency-preserving and time-invariant metamaterial-based nonlinear acoustic diode. *Scientific reports*, 9(1):1–9, 2019.

[20] Osama R Bilal, André Foehr, and Chiara Daraio. Bistable metamaterial for switching and cascading elastic vibrations. *Proceedings of the National Academy of Sciences*, 114(18):4603–4606, 2017.

[21] Thomas Brunet, Jacques Leng, and Olivier Mondain-Monval. Soft acoustic metamaterials. *Science*, 342(6156):323–324, 2013.

[22] Zhengyou Liu, Che Ting Chan, and Ping Sheng. Analytic model of phononic crystals with local resonances. *Physical Review B*, 71(1):014103, 2005.

[23] Thomas Brunet, Aurore Merlin, Benoit Mascaro, Kevin Zimny, Jacques Leng, Olivier Poncelet, Christophe Aristégui, and Olivier Mondain-Monval. Soft 3d acoustic metamaterial with negative index. *Nature materials*, 14(4):384–388, 2015.

[24] Yabin Jin, Raj Kumar, Olivier Poncelet, Olivier Mondain-Monval, and Thomas Brunet. Flat acoustics with soft gradient-index metasurfaces. *Nature communications*, 10(1):1–6, 2019.

[25] Min Yang, Guancong Ma, Zhiyu Yang, and Ping Sheng. Coupled membranes with doubly negative mass density and bulk modulus. *Physical review letters*, 110(13):134301, 2013.

[26] Yangyang Chen, Guoliang Huang, Xiaoming Zhou, Gengkai Hu, and Chin-Teh Sun. Analytical coupled vibroacoustic modeling of membrane-type acoustic metamaterials: Membrane model. *The Journal of the Acoustical Society of America*, 136(3):969–979, 2014.

[27] Yangyang Chen, Guoliang Huang, Xiaoming Zhou, Gengkai Hu, and Chin-Teh Sun. Analytical coupled vibroacoustic modeling of membrane-type acoustic metamaterials: Plate model. *The Journal of the Acoustical Society of America*, 136(6):2926–2934, 2014.

[28] Sam Hyeon Lee, Choon Mahn Park, Yong Mun Seo, Zhi Guo Wang, and Chul Koo Kim. Acoustic metamaterial with negative density. *Physics Letters, Section A: General, Atomic and Solid State Physics*, 2009.

[29] Jun Mei, Guancong Ma, Min Yang, Zhiyu Yang, Weijia Wen, and Ping Sheng. Dark acoustic metamaterials as super absorbers for low-frequency sound. *Nature communications*, 3(1):1–7, 2012.

[30] Zhiyu Yang, Jun Mei, Min Yang, NH Chan, and Ping Sheng. Membrane-type acoustic metamaterial with negative dynamic mass. *Physical review letters*, 101(20):204301, 2008.

[31] *Dynamics of Particles and Bodies*, chapter 2, pages 43–88. John Wiley  Sons, Ltd, 2016.

[32] Sam Hyeon Lee, Choon Mahn Park, Yong Mun Seo, Zhi Guo Wang, and Chul Koo Kim. Acoustic metamaterial with negative modulus. *Journal of Physics: Condensed Matter*, 21(17):175704, 2009.

[33] Sam Hyeon Lee, Choon Mahn Park, Yong Mun Seo, Zhi Guo Wang, and Chul Koo Kim. Composite acoustic medium with simultaneously negative density and modulus. *Physical review letters*, 104(5):054301, 2010.

[34] Nicholas Fang, Dongjuan Xi, Jianyi Xu, Muralidhar Ambati, Werayut Srituravanich, Cheng Sun, and Xiang Zhang. Ultrasonic metamaterials with negative modulus. *Nature materials*, 5(6):452–456, 2006.

[35] Yong Mun Seo, Jong Jin Park, Seung Hwan Lee, Choon Mahn Park, Chul Koo Kim, and Sam Hyeon Lee. Acoustic metamaterial exhibiting four different sign combinations of density and modulus. *Journal of Applied Physics*, 111(2):023504, 2012.

[36] Li Fan, Huan Ge, Shu-yi Zhang, Hai-fei Gao, Yong-hui Liu, and Hui Zhang. Nonlinear acoustic fields in acoustic metamaterial based on a cylindrical pipe with periodically arranged side holes. *The Journal of the Acoustical Society of America*, 133(6):3846–3852, 2013.

[37] JB Pendry, A Aubry, DR Smith, and SA Maier. Transformation optics and subwavelength control of light. *science*, 337(6094):549–552, 2012.

[38] D Schurig, JB Pendry, and David R Smith. Calculation of material properties and ray tracing in transformation media. *Optics express*, 14(21):9794–9804, 2006.

[39] David Schurig, Jack J Mock, BJ Justice, Steven A Cummer, John B Pendry, Anthony F Starr, and David R Smith. Metamaterial electromagnetic cloak at microwave frequencies. *Science*, 314(5801):977–980, 2006.

[40] Wenshan Cai, Uday K Chettiar, Alexander V Kildishev, and Vladimir M Shalaev. Optical cloaking with metamaterials. *Nature photonics*, 1(4):224–227, 2007.

[41] Chen Shen, Jun Xu, Nicholas X Fang, and Yun Jing. Anisotropic complementary acoustic metamaterial for canceling out aberrating layers. *Physical Review X*, 4(4):041033, 2014.

[42] Vladimir Fokin, Muralidhar Ambati, Cheng Sun, and Xiang Zhang. Method for retrieving effective properties of locally resonant acoustic metamaterials. *Physical review B*, 76(14):144302, 2007.

[43] ASTM E2611-19. Standard test method for normal incidence determination of porous material acoustical properties based on the transfer matrix method, 2019.

[44] Seyyed Esfahlani Hussein. Electromagnetic inspired acoustic metamaterials studying the applications of sound-metastructures interactions based on different wave phenomena. page 190, 2017.

[45] Mats Åbom. Measurement of the scattering-matrix of acoustical two-ports. *Mechanical systems and signal processing*, 5(2):89–104, 1991.

[46] Yusuf Tufail, Alexei Matyushov, Nathan Baldwin, Monica L Tauchmann, Joseph Georges, Anna Yoshihiro, Stephen I Helms Tillery, and William J Tyler. Transcranial pulsed ultrasound stimulates intact brain circuits. *Neuron*, 66(5):681–694, 2010.

[47] Wynn Legon, Tomokazu F Sato, Alexander Opitz, Jerel Mueller, Aaron Barbour, Amanda Williams, and William J Tyler. Transcranial focused ultrasound modulates the activity of primary somatosensory cortex in humans. *Nature neuroscience*, 17(2):322–329, 2014.

[48] Seung-Schik Yoo, Alexander Bystritsky, Jong-Hwan Lee, Yongzhi Zhang, Krisztina Fischer, Byoung-Kyong Min, Nathan J McDannold, Alvaro Pascual-Leone, and Ferenc A Jolesz. Focused ultrasound modulates region-specific brain activity. *Neuroimage*, 56(3):1267–1275, 2011.

[49] E Newton Harvey. The effect of high frequency sound waves on heart muscle and other irritable tissues. *American Journal of Physiology-Legacy Content*, 91(1):284–290, 1929.

[50] Michael D Menz, Ömer Oralkan, Pierre T Khuri-Yakub, and Stephen A Baccus. Precise neural stimulation in the retina using focused ultrasound. *Journal of Neuroscience*, 33(10):4550–4560, 2013.

[51] PJ White, GT Clement, and Kullervo Hynynen. Local frequency dependence in transcranial ultrasound transmission. *Physics in Medicine & Biology*, 51(9):2293, 2006.

[52] Gianmarco Pinton, Jean-Francois Aubry, Emmanuel Bossy, Marie Muller, Mathieu Pernot, and Mickael Tanter. Attenuation, scattering, and absorption of ultrasound in the skull bone. *Medical physics*, 39(1):299–307, 2012.

[53] Mickaël Tanter, Jean-Louis Thomas, and Mathias Fink. Focusing and steering through absorbing and aberrating layers: Application to ultrasonic propagation through the skull. *The Journal of the Acoustical Society of America*, 103(5):2403–2410, 1998.

[54] Mathieu Pernot, Jean-Francois Aubry, Mickael Tanter, Anne-Laure Boch, Fabrice Marquet, Michele Kujas, Danielle Seilhean, and Mathias Fink. In vivo transcranial brain surgery with an ultrasonic time reversal mirror. *Journal of neurosurgery*, 106(6):1061–1066, 2007.

[55] Fabrice Marquet, M Pernot, Jean-Francois Aubry, G Montaldo, L Marsac, M Tanter, and M Fink. Non-invasive transcranial ultrasound therapy based on a 3d ct scan: protocol validation and in vitro results. *Physics in Medicine & Biology*, 54(9):2597, 2009.

[56] Gianmarco Pinton, Jean-Francois Aubry, Mathias Fink, and Mickael Tanter. Numerical prediction of frequency dependent 3d maps of mechanical index thresholds in ultrasonic brain therapy. *Medical physics*, 39(1):455–467, 2012.

[57] Steven A Cummer, Johan Christensen, and Andrea Alù. Controlling sound with acoustic metamaterials. *Nature Reviews Materials*, 1(3):1–13, 2016.

[58] Michael R Haberman and Matthew D Guild. Acoustic metamaterials. *Phys. Today*, 69(6):42–48, 2016.

[59] Pierre A Deymier. *Acoustic metamaterials and phononic crystals*, volume 173. Springer Science & Business Media, 2013.

[60] Frédéric Bongard, Hervé Lissek, and Juan R Mosig. Acoustic transmission line metamaterial with negative/zero/positive refractive index. *physical Review B*, 82(9):094306, 2010.

[61] Vitalyi E Gusev and Oliver B Wright. Double-negative flexural acoustic metamaterial. *New Journal of Physics*, 16(12):123053, 2014.

[62] Y Cheng, JY Xu, and XJ Liu. One-dimensional structured ultrasonic metamaterials with simultaneously negative dynamic density and modulus. *Physical Review B*, 77(4):045134, 2008.

[63] Yangbo Xie, Bogdan-Ioan Popa, Lucian Zigoneanu, and Steven A Cummer. Measurement of a broadband negative index with space-coiling acoustic metamaterials. *Physical review letters*, 110(17):175501, 2013.

[64] Nadege Kaina, Fabrice Lemoult, Mathias Fink, and Geoffroy Lerosey. Negative refractive index and acoustic superlens from multiple scattering in single negative metamaterials. *Nature*, 525(7567):77–81, 2015.

[65] Huaijun Chen, Hongcheng Zeng, Changlin Ding, Chunrong Luo, and Xiaopeng Zhao. Double-negative acoustic metamaterial based on hollow steel tube meta-atom. *Journal of Applied Physics*, 113(10):104902, 2013.

[66] Yun Lai, Jack Ng, HuanYang Chen, DeZhuan Han, JunJun Xiao, Zhao-Qing Zhang, and Che Ting Chan. Illusion optics: the optical transformation of an object into another object. *Physical review letters*, 102(25):253902, 2009.

[67] Steven R Craig, Phoebe J Welch, and Chengzhi Shi. Non-hermitian complementary acoustic metamaterials for lossy barriers. *Applied Physics Letters*, 115(5):051903, 2019.

[68] Greg T Clement and K Hynynen. A non-invasive method for focusing ultrasound through the human skull. *Physics in Medicine & Biology*, 47(8):1219, 2002.

[69] Sergio Jiménez-Gambín, Noé Jiménez, José María Benlloch, and Francisco Camarena. Holograms to focus arbitrary ultrasonic fields through the skull. *Physical Review Applied*, 12(1):014016, 2019.

[70] MR Bailey, VA Khokhlova, OA Sapozhnikov, SG Kargl, and LA Crum. Physical mechanisms of the therapeutic effect of ultrasound (a review). *Acoustical Physics*, 49(4):369–388, 2003.

[71] Vera A Khokhlova, Michael R Bailey, Justin A Reed, Bryan W Cunitz, Peter J Kaczkowski, and Lawrence A Crum. Effects of nonlinear propagation, cavitation, and boiling in lesion formation by high intensity focused ultrasound in a gel phantom. *The Journal of the Acoustical Society of America*, 119(3):1834–1848, 2006.

[72] Shahram Vaezy, Xuegong Shi, Roy W Martin, Emil Chi, Peter I Nelson, Michael R Bailey, and Lawrence A Crum. Real-time visualization of high-intensity focused ultrasound treatment using ultrasound imaging. *Ultrasound in medicine & biology*, 27(1):33–42, 2001.

[73] Jinwoong Cha, Kun Woo Kim, and Chiara Daraio. Experimental realization of on-chip topological nanoelectromechanical metamaterials. *Nature*, 564(7735):229–233, 2018.

[74] Jong Jin Park, Choon Mahn Park, KJB Lee, and Sam H Lee. Acoustic superlens using membrane-based metamaterials. *Applied Physics Letters*, 106(5):051901, 2015.

[75] Xiaoming Zhou and Gengkai Hu. Superlensing effect of an anisotropic metamaterial slab with near-zero dynamic mass. *Applied Physics Letters*, 98(26):263510, 2011.

[76] Zhenhua Tian, Chen Shen, Junfei Li, Eric Reit, Yuyang Gu, Hai Fu, Steven A Cummer, and Tony Jun Huang. Programmable acoustic metasurfaces. *Advanced functional materials*, 29(13):1808489, 2019.

[77] Víctor Manuel García-Chocano, Rogelio Graciá-Salgado, D Torrent, F Cervera, and Jose Sánchez-Dehesa. Quasi-two-dimensional acoustic metamaterial with negative bulk modulus. *Physical Review B*, 85(18):184102, 2012.

[78] Sam H Lee and Oliver B Wright. Origin of negative density and modulus in acoustic metamaterials. *Physical Review B*, 93(2):024302, 2016.

[79] David T Blackstock. Fundamentals of physical acoustics, 2001.

[80] DP Jena, J Dandsena, and VG Jayakumari. Demonstration of effective acoustic properties of different configurations of helmholtz resonators. *Applied Acoustics*, 155:371–382, 2019.

[81] Nikhil JRK Gerard, Huachen Cui, Chen Shen, Yangbo Xie, Steven Cummer, Xiaoyu Zheng, and Yun Jing. Fabrication and experimental demonstration of a hybrid resonant acoustic gradient index metasurface at 40 khz. *Applied Physics Letters*, 114(23):231902, 2019.

[82] Samir Mitragotri. Healing sound: the use of ultrasound in drug delivery and other therapeutic applications. *Nature reviews Drug discovery*, 4(3):255–260, 2005.

[83] Steven A. Cummer, Johan Christensen, and Andrea Alù. Controlling sound with acoustic metamaterials. *Nature Reviews Materials*, 1(3):16001, 2016.

[84] G. Ma and P. Sheng. Acoustic metamaterials: From local resonances to broad horizons. *Science Advances*, 2(2):e1501595–e1501595, 2016.

[85] Chen Shen, Yangbo Xie, Ni Sui, Wenqi Wang, Steven A Cummer, and Yun Jing. Broadband acoustic hyperbolic metamaterial. *Physical review letters*, 115(25):254301, 2015.

[86] Nicholas Fang, Dongjuan Xi, Jianyi Xu, Muralidhar Ambati, Werayut Srituravanich, Cheng Sun, and Xiang Zhang. Ultrasonic metamaterials with negative modulus. *Nature Materials*, 5(6):452–456, 2006.

[87] E Cianci, A Schina, A Minotti, S Quaresima, and V Foglietti. Dual frequency pecvd silicon nitride for fabrication of cmuts' membranes. *Sensors and Actuators A: Physical*, 127(1):80–87, 2006.

[88] Annette Lohfink and P-C Eccardt. Linear and nonlinear equivalent circuit modeling of cmuts. *IEEE transactions on ultrasonics, ferroelectrics, and frequency control*, 52(12):2163–2172, 2005.

[89] Byung Lee, Amin Nikoozadeh, Kwan Park, and Butrus Khuri-Yakub. High-efficiency output pressure performance using capacitive micromachined ultrasonic transducers with substrate-embedded springs. *Sensors*, 18(8):2520, 2018.

[90] Hao Nan, Kevin C Boyle, Nikhil Apte, Miaad S Aliroteh, Anshuman Bhuyan, Amin Nikoozadeh, Butrus T Khuri-Yakub, and Amin Arbabian. Non-contact thermoacoustic detection of embedded targets using airborne-capacitive micromachined ultrasonic transducers. *Applied Physics Letters*, 106(8):084101, 2015.

[91] O. Vazquez-Mena, L. Gross, S. Xie, L.G. Villanueva, and J. Brugger. Resistless nanofabrication by stencil lithography: A review. *Microelectronic Engineering*, 132:236 – 254, 2015. Micro and Nanofabrication Breakthroughs for Electronics, MEMS and Life Sciences.

[92] Tolga Bagci, Anders Simonsen, Silvan Schmid, Luis G Villanueva, Emil Zeuthen, Jürgen Appel, Jacob M Taylor, A Sørensen, Koji Usami, Albert Schliesser, and Eugene Polzik. Optical detection of radio waves through a nanomechanical transducer. *Nature*, 507(7490):81, 2014.

[93] Hien D Tong, Henri V Jansen, Vishwas J Gadgil, Cazimir G Bostan, Erwin Berenschot, Cees JM van Rijn, and Miko Elwenspoek. Silicon nitride nanosieve membrane. *Nano letters*, 4(2):283–287, 2004.

[94] Oscar Vazquez-Mena, Guillermo Villanueva, Veronica Savu, Katrin Sidler, MAF Van Den Boogaart, and Juergen Brugger. Metallic nanowires by full wafer stencil lithography. *Nano Letters*, 8(11):3675–3682, 2008.

[95] P.J French, P.M Sarro, R Mallée, E.J.M Fakkeldij, and R.F Wolffenbuttel. Optimization of a low-stress silicon nitride process for surface-micromachining applications. *Sensors and Actuators A: Physical*, 58(2):149 – 157, 1997.

[96] O. Oralkan, S. T. Hansen, B. Bayram, G. G. Yaralioglu, A. S. Ergun, and B. T. Khuri-Yakub. High-frequency cmut arrays for high-resolution medical imaging. In *IEEE Ultrasonics Symposium, 2004*, volume 1, pages 399–402 Vol.1, 2004.

[97] Kevin Brenner, Arif Sanli Ergun, Kamyar Firouzi, Morten Fischer Rasmussen, Quintin Stedman, and Butrus (Pierre) Khuri–Yakub. Advances in capacitive micromachined ultrasonic transducers. *Micromachines*, 10(2), 2019.

[98] Bernd Folkmer, Peter Steiner, and Walter Lang. A pressure sensor based on a nitride membrane using single-crystalline piezoresistors. *Sensors and Actuators A: Physical*, 54(1-3):488–492, jun 1996.

[99] M. Amabili and M.K. Kwak. Free vibrations of circular plates coupled with liquids: Revising the lamb problem. *Journal of Fluids and Structures*, 10(7):743 – 761, 1996.

[100] Moon K Kwak. Hydroelastic vibration of rectangular plates. *Journal of applied mechanics*, 63(1):110–115, 1996.

[101] L. G. Villanueva and S. Schmid. Evidence of surface loss as ubiquitous limiting damping mechanism in sin micro- and nanomechanical resonators. *Phys. Rev. Lett.*, 113:227201, Nov 2014.

[102] John Elie Sader. Frequency response of cantilever beams immersed in viscous fluids with applications to the atomic force microscope. *Journal of Applied Physics*, 84(1):64–76, 1998.

[103] Ali H Nayfeh and Mohammad I Younis. A new approach to the modeling and simulation of flexible microstructures under the effect of squeeze-film damping. *Journal of Micromechanics and Microengineering*, 14(2):170, 2003.

[104] Chuanli Zhang, Guanshui Xu, and Qing Jiang. Characterization of the squeeze film damping effect on the quality factor of a microbeam resonator. *Journal of Micromechanics and Microengineering*, 14(10):1302, 2004.

[105] John E Sader, Julian A Sanelli, Brian D Adamson, Jason P Monty, Xingzhan Wei, Simon A Crawford, James R Friend, Ivan Marusic, Paul Mulvaney, and Evan J Bieske. Spring constant calibration of atomic force microscope cantilevers of arbitrary shape. *Review of Scientific Instruments*, 83(10):103705, 2012.

[106] A De Pastina, D Maillard, and LG Villanueva. Fabrication of suspended microchannel resonators with integrated piezoelectric transduction. *Microelectronic Engineering*, 192:83–87, 2018.

[107] William Connacher, Naiqing Zhang, An Huang, Jiyang Mei, Shuai Zhang, Tilvawala Gopesh, and James Friend. Micro/nano acoustofluidics: materials, phenomena, design, devices, and applications. *Lab on a Chip*, 2018.

[108] MR Haddara and S Cao. A study of the dynamic response of submerged rectangular flat plates. *Marine Structures*, 9(10):913–933, 1996.

[109] Liang Sun, Ning Wang, Chong Meng, and Z Yang. High ultrasonic transmission loss metasurfaces in water. *arXiv preprint arXiv:1701.07923*, 2017.

[110] MJ Holmes, NG Parker, and MJW Povey. Temperature dependence of bulk viscosity in water using acoustic spectroscopy. In *Journal of Physics: Conference Series*, volume 269, page 012011. IOP Publishing, 2011.

[111] Robert D Blevins. *Formulas for dynamics, acoustics and vibration*. John Wiley & Sons, 2015.

[112] Abdelhamid Maali, Cedric Hurth, Rodolphe Boisgard, Cédric Jai, Touria Cohen-Bouhacina, and Jean-Pierre Aimé. Hydrodynamics of oscillating atomic force microscopy cantilevers in viscous fluids. *Journal of Applied Physics*, 97(7):074907, apr 2005.

[113] Zhangming Wu and Xianghong Ma. Dynamic analysis of submerged microscale plates: the effects of acoustic radiation and viscous dissipation. *Proceedings of the Royal Society A: Mathematical, Physical and Engineering Sciences*, 472(2187):20150728, 2016.

[114] Jae-Woo Im, Woo-Pyo Jeong, Doo-Hyun Kim, Sang-Wan Nam, Dong-Kyo Shim, Myung-Hoon Choi, Hyun-Jun Yoon, Dae-Han Kim, You-Se Kim, Hyun-Wook Seok-Min Yoon Park, Wook-Ghee Hahn, Jin-Ho Ryu, Sang-Won Shim, Kyung-Tae Kang, Sung-Ho Choi, Jeong-Don Ihm, Young-Sun Min, In-Mo Kim, Doo-Sub Lee, Ji-Ho Cho, Oh-Suk Kwon, Ji-Sang Lee, Moo-Sung Kim, Sang-Hyun Joo, Jae-Hoon Jang, Sang-Won Hwang, Dae-Seok Byeon andHyang Ja Yang, Ki-Tae Park, Kye-Hyun Kyung, and Jeong-Hyuk Choi. 7.2 a 128gb 3b/cell v-nand flash memory with 1gb/s i/o rate. In *2015 IEEE International Solid-State Circuits Conference-(ISSCC) Digest of Technical Papers*, pages 1–3. IEEE, 2015.

[115] Ki-Tae Park, Sangwan Nam, Daehan Kim, Pansuk Kwak, Doosub Lee, Yoon-He Choi, Myung-Hoon Choi, Dong-Hun Kwak, Doo-Hyun Kim, Min-Su Kim, Hyun-Wook Park, Sang-Won Shim, Kyung-Min Kang, Sang-Won Park, Kangbin Lee, Hyun-Jun Yoon, Kuihan Ko, Dong-Kyo Shim, Yang-Lo Ahn, Jinho Ryu, Donghyu Kim, Joonsoo Kwon, Seunghoon Shin, Dae-Seok Byeon, Kihwan Choi, Jin-Man Han, Kye-Hyun Kyung, Jeong-Hyuk Choi, and Kinam Kim. Three-dimensional 128 gb mlc vertical nand flash memory with 24-wl stacked layers and 50 mb/s high-speed programming. *IEEE Journal of Solid-State Circuits*, 50(1):204–213, 2014.

[116] Max M Shulaker, Gage Hills, Rebecca S Park, Roger T Howe, Krishna Saraswat, H-S Philip Wong, and Subhasish Mitra. Three-dimensional integration of nanotechnologies for computing and data storage on a single chip. *Nature*, 547(7661):74–78, 2017.

[117] Jemma L Vickery, Avinash J Patil, and Stephen Mann. Fabrication of graphene–polymer nanocomposites with higher-order three-dimensional architectures. *Advanced Materials*, 21(21):2180–2184, 2009.

[118] Owen C Compton and SonBinh T Nguyen. Graphene oxide, highly reduced graphene oxide, and graphene: versatile building blocks for carbon-based materials. *small*, 6(6):711–723, 2010.

[119] Chun Li and Gaoquan Shi. Three-dimensional graphene architectures. *Nanoscale*, 4(18):5549–5563, 2012.

[120] Mohammad Vaezi, Hermann Seitz, and Shoufeng Yang. A review on 3d micro-additive manufacturing technologies. *The International Journal of Advanced Manufacturing Technology*, 67(5-8):1721–1754, 2013.

[121] Zhong Xun Khoo, Joanne Ee Mei Teoh, Yong Liu, Chee Kai Chua, Shoufeng Yang, Jia An, Kah Fai Leong, and Wai Yee Yeong. 3d printing of smart materials: A review on recent progresses in 4d printing. *Virtual and Physical Prototyping*, 10(3):103–122, 2015.

[122] Bharat Bhushan and Matt Caspers. An overview of additive manufacturing (3d printing) for microfabrication. *Microsystem Technologies*, 23(4):1117–1124, 2017.

[123] Brian H Cumpston, Sundaravel P Ananthavel, Stephen Barlow, Daniel L Dyer, Jeffrey E Ehrlich, Lael L Erskine, Ahmed A Heikal, Stephen M Kuebler, I-Y Sandy Lee, Dianne McCord-Maughon, Jinqui Qin, Harald Röckel, Mariacristina Rumi, Xiang-Li Wu, Seth R. Marder, and Joseph W. Perry. Two-photon polymerization initiators for three-dimensional optical data storage and microfabrication. *Nature*, 398(6722):51–54, 1999.

[124] Joachim Fischer and Martin Wegener. Three-dimensional optical laser lithography beyond the diffraction limit. *Laser & Photonics Reviews*, 7(1):22–44, 2013.

[125] Justyna K Gansel, Michael Latzel, Andreas Frölich, Johannes Kaschke, Michael Thiel, and Martin Wegener. Tapered gold-helix metamaterials as improved circular polarizers. *Applied Physics Letters*, 100(10):101109, 2012.

[126] Nicolas Muller, Jakub Haberko, Catherine Marichy, and Frank Scheffold. Silicon hyperuniform disordered photonic materials with a pronounced gap in the shortwave infrared. *Advanced Optical Materials*, 2(2):115–119, 2014.

[127] Aránzazu del Campo and Christian Greiner. Su-8: a photoresist for high-aspect-ratio and 3d submicron lithography. *Journal of micromechanics and microengineering*, 17(6):R81, 2007.

[128] Bong Gill Choi, MinHo Yang, Won Hi Hong, Jang Wook Choi, and Yun Suk Huh. 3d macroporous graphene frameworks for supercapacitors with high energy and power densities. *ACS nano*, 6(5):4020–4028, 2012.

[129] Jiantie Xu, Min Wang, Nilantha P Wickramaratne, Mietek Jaroniec, Shixue Dou, and Liming Dai. High-performance sodium ion batteries based on a 3d anode from nitrogen-doped graphene foams. *Advanced materials*, 27(12):2042–2048, 2015.

[130] Xiehong Cao, Zongyou Yin, and Hua Zhang. Three-dimensional graphene materials: preparation, structures and application in supercapacitors. *Energy & Environmental Science*, 7(6):1850–1865, 2014.

[131] Duy Tho Pham, Tae Hoon Lee, Dinh Hoa Luong, Fei Yao, Arunabha Ghosh, Viet Thong Le, Tae Hyung Kim, Bing Li, Jian Chang, and Young Hee Lee. Carbon nanotube-bridged graphene 3d building blocks for ultrafast compact supercapacitors. *ACS nano*, 9(2):2018–2027, 2015.

[132] Arend M van der Zande, Robert A Barton, Jonathan S Alden, Carlos S Ruiz-Vargas, William S Whitney, Phi HQ Pham, Jiwoong Park, Jeevak M Parpia, Harold G Craighead, and Paul L McEuen. Large-scale arrays of single-layer graphene resonators. *Nano letters*, 10(12):4869–4873, 2010.

[133] Antoine Reserbat-Plantey, Dipankar Kalita, Zheng Han, Laurence Ferlazzo, Sandrine Autier-Laurent, Katsuyoshi Komatsu, Chuan Li, Raphael Weil, Arnaud Ralko, Laetitia Marty, Sophie Guéron, Nedjma Bendiab, Hélène Bouchiat, and Vincent Bouchiat. Strain

superlattices and macroscale suspension of graphene induced by corrugated substrates. *Nano letters*, 14(9):5044–5051, 2014.

[134] Yu-Min Chen, Shih-Ming He, Chi-Hsien Huang, Cheng-Chun Huang, Wen-Pin Shih, Chun-Lin Chu, Jing Kong, Ju Li, and Ching-Yuan Su. Ultra-large suspended graphene as a highly elastic membrane for capacitive pressure sensors. *Nanoscale*, 8(6):3555–3564, 2016.

[135] Herbert R Philipp. Optical properties of silicon nitride. *Journal of the Electrochemical Society*, 120(2):295, 1973.

[136] Rahul Raveendran Nair, Peter Blake, Alexander N Grigorenko, Konstantin S Novoselov, Tim J Booth, Tobias Stauber, Nuno MR Peres, and Andre K Geim. Fine structure constant defines visual transparency of graphene. *Science*, 320(5881):1308–1308, 2008.

[137] VG Kravets, F Schedin, and AN Grigorenko. Extremely narrow plasmon resonances based on diffraction coupling of localized plasmons in arrays of metallic nanoparticles. *Physical review letters*, 101(8):087403, 2008.

[138] Meni Wanunu, Tali Dadosh, Vishva Ray, Jingmin Jin, Larry McReynolds, and Marija Drndić. Rapid electronic detection of probe-specific micrornas using thin nanopore sensors. *Nature nanotechnology*, 5(11):807–814, 2010.

[139] Arif E Cetin, Ahmet F Coskun, Betty C Galarreta, Min Huang, David Herman, Aydogan Ozcan, and Hatice Altug. Handheld high-throughput plasmonic biosensor using computational on-chip imaging. *Light: Science & Applications*, 3(1):e122–e122, 2014.

[140] Xiaokang Li, Maria Soler, Cenk I Özdemir, Alexander Belushkin, Filiz Yesilköy, and Hatice Altug. Plasmonic nanohole array biosensor for label-free and real-time analysis of live cell secretion. *Lab on a Chip*, 17(13):2208–2217, 2017.

[141] O Vazquez-Mena, L Gross, S Xie, LG Villanueva, and Jürgen Brugger. Resistless nanofabrication by stencil lithography: A review. *Microelectronic Engineering*, 132:236–254, 2015.

[142] Alexey I Ekimov, F Hache, MC& al Schanne-Klein, D Ricard, Chr Flytzanis, IA Kudryavtsev, TV Yazeva, AV Rodina, and Al L Efros. Absorption and intensity-dependent photoluminescence measurements on cdse quantum dots: assignment of the first electronic transitions. *JOSA B*, 10(1):100–107, 1993.